Confocal Acoustic Holography for Non-Invasive 3D Temperature and Composition Measurement

by

Stefan Atalick
B.Sc., University of Waterloo, 2004

A Thesis Submitted in Partial Fulfillment
of the Requirements for the Degree of

MASTER OF APPLIED SCIENCE

in the department of Mechanical Engineering

University of Victoria
satalick@gmail.com

SUPERVISORY INFORMATION

Confocal Acoustic Holography for Non-Invasive
3D Temperature and Composition Measurement

by

Stefan Atalick
B.Sc., University of Waterloo, 2004

Supervisory Committee

Supervisor
Dr. Rodney Herring (Department of Mechanical Engineering)

Departmental Member
Dr. Barbara Sawicki (Department of Mechanical Engineering)

Outside Member
Dr. Adam Zielinski (Department of Electrical & Computer Engineering)

Supervisory Committee

Supervisor: Dr. Rodney Herring, Mechanical Engineering

Departmental Member: Dr. Barbara Sawicki, Mechanical Engineering

Outside Member: Dr. Adam Zielinski, Electrical & Computer Engineering

ABSTRACT

This thesis summarizes my work at the University of Victoria to design and evaluate a proof-of-concept instrument called the Confocal Acoustic Holography Microscope (CAHM). The instrument will be able to measure small changes in temperature and composition in a fluid specimen, which can be indirectly measured via small fluctuations in the speed of sound. The CAHM combines concepts of confocal microscopy, interferometry, and ultrasonic imaging. This recent work in confocal acoustic holography has progressed from our previous research in confocal laser holography.

The prototype CAHM design uses a frequency of 2.25 MHz, and can measure sound speed changes of 16 m/s, temperature changes of 5°C, with a spatial resolution of 660 μm. With future improvements to the CAHM, utilizing the latest technologies such as 2D array detectors, MEMS, and acoustic lenses, we expect resolutions of 1 m/s, 0.5°C, and 150 μm.

The design of the CAHM involved the production of a 3D CAD layout of the opto-mechanical components and ray tracing simulations using Zemax optical design software. Simulated acoustic holograms and fringe shifts were produced and they were found to match up very well with theoretical calculations.

A simplified acoustic holography instrument was built and tested. Speed of sound measurements were made for several test specimens, while keeping temperature constant. Specimens of ethanol, isopropanol, acetic acid, glycerine, and mineral oil were measured. Holograms were collected for acetic acid and mineral oil and were compared to the reference case (distilled water). The fringe spacing and phase shifts measured experimentally matched up well with the Zemax simulations and the theoretical calculations. Hence, the popular Zemax optical software can be effectively used to design acoustic instruments. To our knowledge, this is the first use of Zemax for acoustic designs.

Based on the successful results of the simulations and experiments, the CAHM is expected to have many useful applications, especially in medical diagnostics where it could be used to measure density and temperature within the human body. Phase contrast images could also be used to help identify suspicious lesions, such as those found in prostate or breast tissue. Other applications include non-destructive testing of electronic and mechanical parts, measurements of fluid samples, material science experiments, and microgravity experiments, where non-invasive examination is required.

TABLE OF CONTENTS

LIST OF FIGURES

LIST OF TABLES

LIST OF EQUATIONS

ABBREVIATIONS & TERMINOLOGY

adenocarcinoma - a malignant tumour arising from secretory epithelium

aneurysm - permanent cardiac or arterial dilatation usually caused by weakening of the vessel wall

CAD - Computer Aided Design

CAHM - Confocal Acoustic Holography Microscope

CCD - Charge Coupled Device

CNC - Computerized Numerically Controlled (machining)

CW - Continuous Wave

DIDSON - Dual Frequency Identification Sonar

DIH - Digital In-Line Holography

fibrosis - development of excess fibrous connective tissue in an organ

FT - Fourier Transform

granulation tissue - tissue formed in early wound healing and repair, composed largely of newly growing capillaries

haemorrhage - flow of blood from a ruptured blood vessel

IFT - Inverse Fourier Transform

in vivo - occurring or made to occur within a living organism or natural setting

LASER - Light Amplification by Stimulated Emission of Radiation

lipoma - a benign tumour consisting of fat tissue

macrophage - a large white blood cell, occurring principally in connective tissue and the bloodstream, that ingests foreign particles and infectious micro-organisms

MEMS - Micro Electromechanical Systems

mucosa - mucus-secreting membrane lining passages that communicate with the exterior

myocardium - muscular tissue of the heart

NAH - Nearfield Acoustic Holography

NDT - Non Destructive Testing

ppt - parts per thousand

renal - of or pertaining to the kidneys or the surrounding regions

RMS - Root Mean Squared

SAM - Scanning Acoustic Microscopy

SATM - Scanning Acoustic Transmission Microscopy

transverse mode - a sound wave which has its displacement perpendicular to the propagation direction

TRH - Temporal Reference Holography

Zemax - Zemax Optical Design software

ACKNOWLEDGEMENTS

I would like to acknowledge and express my sincere thanks to my supervisor, Professor Rodney Herring. Rodney is the originator of the concept of confocal holography and its application to acoustics. Without his assistance and support, this research would not have been possible.

I would like to thank my research compatriots: Rodney Herring, Peter Jacquemin, and Barbara Sawicki for their regular and vital input to the project during our weekly discussions. I would like also to thank Paul Kraeutner, Ross Chapman, Songcan Lai, Robert McLeod, and Horace Luong for their valuable input.

Thanks to Arthur Makosinski, Patrick Chang, and Ian Soutar for lending the wave generators and digital oscilloscopes for the experiments. Thanks especially to Adam Zielinski for providing the ultrasound transducers, which allowed me to learn the basics of ultrasound transduction and ultimately to design and perform the holography experiments.

Funding to support this research was provided by the University of Victoria and the Canadian Foundation for Innovation. Some equipment was provided on loan from the Canadian Space Agency.

1 INTRODUCTION & MOTIVATION

An acoustic hologram is produced by the interference of two coherent sound waves. Acoustic interference is analogous to optical interference, except that sound propagates as longitudinal pressure oscillations, whereas light propagates as transverse waves. Recent work at the University of Victoria in confocal acoustic holography has progressed from previous research in confocal laser holography [1,2].

When two coherent sources of waves overlap, their signals combine either constructively or destructively. The result is a fringe pattern, or hologram, which retains the phase information from the two interacting beams. If an object beam passes through a specimen and interferes with a known reference beam, then phase information can be recorded for the specimen. The phase information is directly related to the speed of sound (or refractive index) of the material, which in turn is a function of the temperature and composition. The object beam is used to internally probe a specimen. Therefore, acoustic holography can non-invasively measure useful internal properties of a specimen, such as temperature and composition.

In contrast to ultrasonic imaging, optical imaging can only penetrate a few millimetres into tissue before scattering significantly [3]. Furthermore, measuring the speed of sound of tissue can provide information on its physical and mechanical properties, such as elasticity, which cannot be measured by optical imaging [4]. One of the main motivations for the design and construction of the Confocal Acoustic Holography Microscope (CAHM) is that there is currently no method to measure temperature accurately and non-invasively within the human body.

Several recent studies of human tissue showed that it is possible to distinguish some types of diseased tissue from healthy tissue based on their differences in mechanical properties, including their speed of sound. For example, in one study by Saijo et al, they discovered that aortic tissue infiltrated with macrophages showed higher values of attenuation and sound speed than the surrounding tissues [5]. These measurements were made via scanning Acoustic Microscopy (SAM) on tissue surgically excised from patients suffering aortic aneurysms. Saijo et al concluded that the increased speed of sound indicated a decrease in elasticity and hence a mechanical weakness of the aneurysm tissues, when compared to a normal aortic tissue [5]. Using an instrument such as the CAHM, it may be possible to screen a patient for these types of changes before the patient suffers an aneurism.

A change in the mechanical properties of tissue could be used to identify sites of disease in cancer patients. This is due to the fact that many cancers involve exudation of fluids from

the vascular or lymphatic systems into the extra-cellular and intra-cellular space [6]. The result is an increase in stiffness or elastic modulus of the tissue, which is why manual palpation is often used to physically examine a patient from outside the body or inside the body during surgery. It is also known that the elastic modulus of breast tumours can differ from surrounding tissues by a factor of 90-fold [6]. These changes in the mechanical properties will influence the acoustic properties of the cancerous tissue, and hence would likely be detectable using acoustic holography. For example, Table 1 shows the speed of sound and attenuation values for aortic tissue [7], myocardial tissue [8], renal (kidney) tissue [9], and gastric tissue [10], and shows the differences of these values for diseased tissue.

Table 1: Attenuation and Sound Speed for Normal and Diseased Tissue

Aortic Structure	**Attenuation**	**Speed of sound**
normal intima	0.61 dB/mm/MHz	1568 m/s
calcificated lesion	2.5 dB/mm/MHz	1760 m/s
fibrosis	1.7 dB/mm/MHz	1677 m/s
fatty material	0.34 dB/mm/MHz	1526 m/s
Myocardial Structure	**Attenuation**	**Speed of sound**
normal myocardium	0.94 dB/mm/MHz	1620.2 m/s
degenerated myocardium	0.71 dB/mm/MHz	1572.4 m/s
granulation tissue	0.88 dB/mm/MHz	1590.2 m/s
fibrosis	1.75 dB/mm/MHz	1690.3 m/s
Tissue in Renal Tumours	**Attenuation**	**Speed of sound**
lipoma cell	0.71 dB/mm/MHz	1515 m/s
clear cell renal cancer	0.94 dB/mm/MHz	1538 m/s
granular cell renal cancer	0.67 dB/mm/MHz	1540 m/s
smooth muscle fibres	0.66 dB/mm/MHz	1574 m/s
fibrosis	1.62 dB/mm/MHz	1667 m/s
haemorrhage	1.87 dB/mm/MHz	1668 m/s
blood vessels	1.88 dB/mm/MHz	1679 m/s
Gastric Tissue	**Attenuation**	**Speed of sound**
normal mucosa	1.04 dB/mm/MHz	1619 m/s
papillary adenocarcinoma	1.12 dB/mm/MHz	1610 m/s
tubular adenocarcinoma (well-differentiated)	2.12 dB/mm/MHz	1667 m/s
tubular adenocarcinoma (moderately-differentiated)	1.43 dB/mm/MHz	1600 m/s
adenocarcinoma (poorly-differentiated)	0.69 dB/mm/MHz	1557 m/s
singlet-ring cell carcinoma	0.49 dB/mm/MHz	1523 m/s

The speeds of sound shown in this table have variations of as little as 9 m/s between normal and diseased tissue. Therefore, an instrument that could accurately measure variations in sound speed on this order may be able to detect the diseases non-invasively from outside the body. Another study by Techavipoo [11] reports on the differences of speed of sound

and attenuation measured in liver tissue at various temperatures. This data is shown in Table 2.

Table 2: Attenuation and Sound Speed for Liver Tissue vs Temperature

Liver Temperature	Attenuation @ 5 MHz	Speed of Sound
22°C	0.401 dB/mm	1580 m/s
25°C	0.356 dB/mm	1576 m/s
30°C	0.358 dB/mm	1584 m/s
37°C	0.351 dB/mm	1598 m/s
40°C	0.331 dB/mm	1594 m/s
50°C	0.376 dB/mm	1601 m/s
60°C	0.359 dB/mm	1602 m/s

This data suggests that it should possible to extract temperature information about tissue simply by measuring the speed of sound (or refractive index). Measurements of sound speed and attenuation in tissue have been performed thus far only on excised tissue using Scanning Acoustic Microscopy (SAM). However, it is conceivable that other techniques sensitive to changes in sound speed, such as acoustic holography, could be used non-invasively to distinguish between healthy and diseased tissue *in vivo*. The Confocal Acoustic Holography Microscope (CAHM) would be an ideal candidate to perform such measurements.

2 BACKGROUND INFORMATION

2.1 Introduction to Holography

Holography is an imaging method that collects two important pieces of information, the intensity and the phase of waves that pass through a specimen. A holographic image is known as a hologram. The word hologram comes from the Greek roots of *holos*, meaning whole or complete and *gram*, meaning writing or message [12]. Translated, the word hologram conveys the meaning *whole message*.

Holography was first envisioned by Hungarian born physicist, Denis Gabor in 1949, who proposed a method of electron and optical microscopy that could reconstruct the wavefronts of coherent electrons passing through a specimen by interfering them with a known reference electron beam [13,14]. He received the Nobel prize in physics in 1971 for this work. Gabor's original idea for holography was an *"on-axis"* or *"in-line"* design as shown in Figure 1, [13].

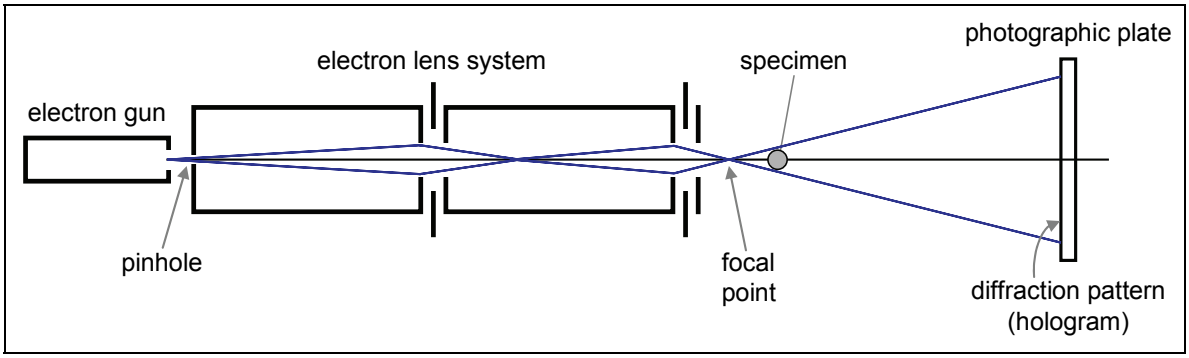

Figure 1: Original Design for Wavefront Reconstruction (Holography)

In this on-axis design, the wavefront of the electron beam interferes with itself to produce a diffraction pattern (hologram) at the photographic plate on the right. Modern, high resolution holography studies typically use an off-axis method [1].

2.1.1 Optical Holography

Gabor also proposed using coherent optical sources of illumination, but it was not until the invention of the LASER in the 1960s that holography became practical in the optical realm. Typically, the amplitude and phase information was stored on film and a 3D image of the specimen could later be reconstructed by illuminating the film with coherent light. For example, the holograms on modern credit cards are of this type, as are the holographic "eye" glasses shown in Figure 2.

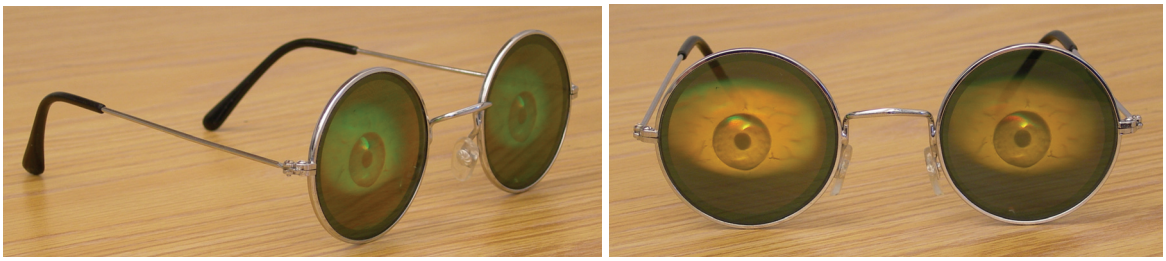

Figure 2: Holographic "Eye" Glasses

In this case, the hologram is illuminated with white (incoherent) light, but the hologram predominantly selects out and reflects a narrow frequency band, depending on the observation angle. The photo on the left shows predominant reflection of green light, and the photo on the right shows predominant reflection of orange light. The 3D information of the original specimen can be reconstructed from the amplitude and phase information stored on the film. The modern, more useful way of recording holographic data from electron, light, or sound holograms is to store the intensity and phase data digitally.

2.1.2 Digital Measurement of Light

When an optical detector (such as a CCD camera) measures the amount of light illuminating its surface, the measured quantity is called the irradiance, represented by I. Irradiance is a measure of the average energy per unit area per unit time. Irradiance is proportional to the square of the electric field amplitude. That is, for an oscillating electric field, $\vec{E}(r,t)$,

$$I \propto \left\langle \vec{E}^2 \right\rangle_T = \left\langle \vec{E}(t) \cdot \vec{E}(t) \right\rangle_T \tag{1}$$

where the time average of a function f(t) taken over an interval T is defined as:

$$\left\langle f(t) \right\rangle_T = \frac{1}{T} \int_t^{t+T} f(t')\, dt' \tag{2}$$

In other words, the limited speed of a digital detector can only measure the time-average intensity of rapidly oscillating light waves (~10^{14} Hz) and not the phase. However, it is still possible to measure the phase of light indirectly using holography or interferometry. To use the strict definition, the term *holography* technically refers to the measurement of *absolute* phase, whereas *interferometry* refers to the measurement of *relative* phase. Holography is therefore a special case of interferometry. Usually monochromatic light or a very narrow frequency band of light is used for optical digital holography.

2.1.3 Off-Axis Optical Holography

One form of optical (laser) holography, which is currently used at UVic, is shown in Figure 3, [15]. This type is often referred as *off-axis* holography, in contrast to Gabor's original *on-axis* design.

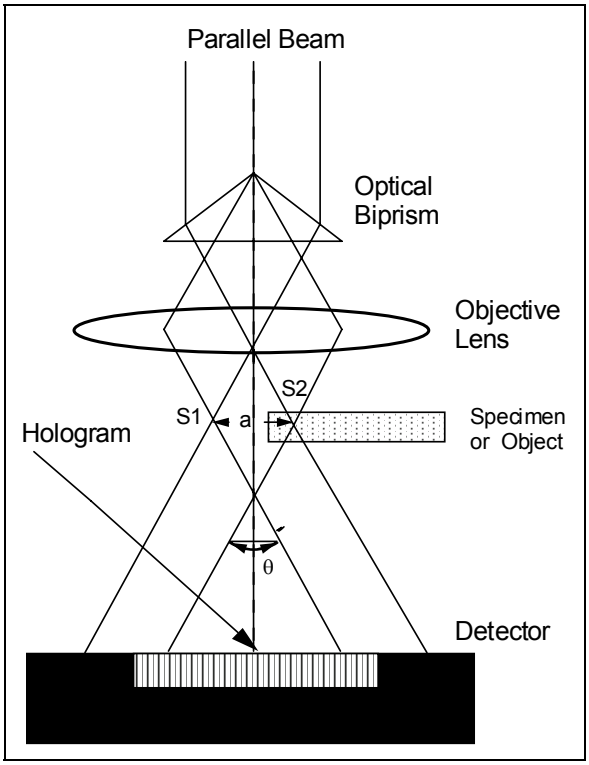

Figure 3: Off-Axis Optical Holography, with Wavefront Splitting

In this technique, a biprism is used to wavefront-split the incoming collimated light beam in half, which effectively creates two probes. One probe is directed to pass through the specimen (object beam, S2), and the other to pass to the side of the specimen (reference beam, S1). The two coherent beams overlap and interfere at the detector to form a hologram. To obtain accurate results, both beams should be in phase when there is no specimen present, so the only phase difference measured by the instrument is due to the inserted specimen. Hence, both beams should travel the same optical path length and have the same propagation conditions.

Accurate translating devices are needed to align the optical components and set the proper path lengths. The hologram produced when no specimen is present is called the *reference hologram*. If the path lengths of the two beams are slightly different, the beams will not be in perfect phase at the detector and only a relative phase measurement can be made. In this case, the term *interferometry* should be used.

Figure 4 shows an example of an optical reference hologram collected by a CCD camera for the configuration shown previously in Figure 3. The laser wavelength used was 633 nm.

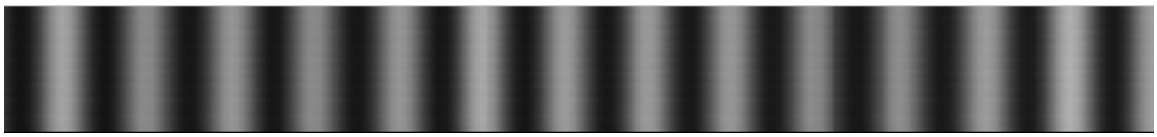

Figure 4: Sample Optical Hologram

The bright areas (intensity maxima for wave reinforcement) are shown as white, while the dark areas (intensity minima for wave cancellation) are shown as black. The camera used, (Redlake MegaPlus II ES 3200), has 12-bit resolution, which means that the recorded grayscale values of intensity are in the range of 1 to 4096. The pixel spacing of the camera is 6.8 μm.

If a specimen is placed in the object beam, as in Figure 3, amplitude and phase can be extracted from the hologram to reconstruct useful information about the specimen, such as temperature and composition. When the object beam is scanned through an inhomogeneous specimen, the phase of the object beam will shift either positively or negatively, due to the change in wave speed (increase or decrease) within the specimen. The specimen is sometimes called a *phase object*, since it phase-modifies the object beam. A change in wave speed changes the phase of the object beam which shows up as a fringe shift of the hologram at the detector. The horizontal fringe shift of the hologram is proportional to the change in wave speed (or change in refractive index) within the specimen. The calculation for this fringe shift for a simple specimen is given in section 4.3.

2.1.4 Digital In-Line Holography (DIH)

Optical In-Line Holography is also sometimes referred to as Optical Digital In-Line Holography, or simply DIH. However, the DIH label could also refer to electron or acoustic holography. In one form of Optical DIH, reported by Kruezer et al. [16], a digital hologram is generated without the use of a separate reference beam. Instead, the incident light beam interferes with itself, as shown in Figure 5, [17].

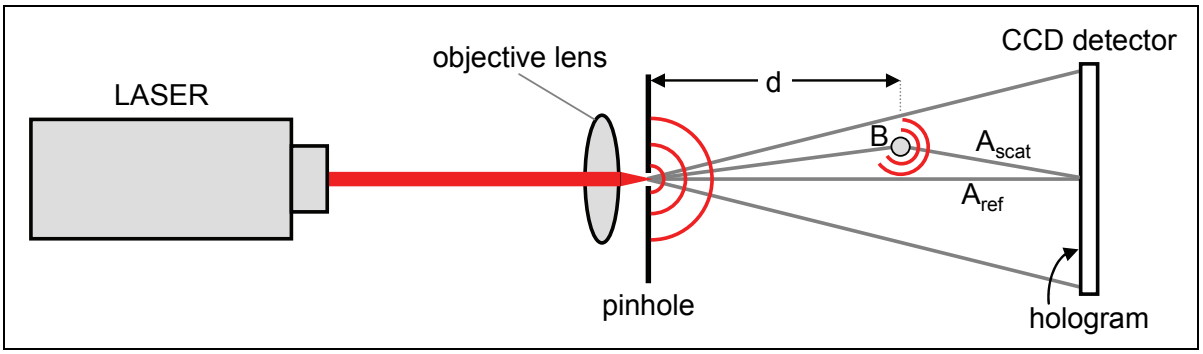

Figure 5: Schematic of Optical Digital In-line Holography (DIH)

This design uses a point source of monochromatic light which propagates as spherical waves from a pinhole and interferes with itself. This design is basically an optical version of Gabor's electron holography design shown in Figure 1. Part of the wave passes through a specimen point (B), called the *scattered* component, and part of the wave travels undeviated to the detector and acts as a reference. The two wave components, A_{scat} and A_{ref}, interfere at the CCD detector to form a digital hologram. The specimen of lateral dimension, b, to be visualized is placed at a distance, d, from the pinhole source such that the Fraunhofer condition, $b^2 << d\lambda$, is fulfilled [16]. In other words, the measurement is made in the nearfield of the beam, where the phase can be written as a linear function of the aperture variables [18].

For the setup in Figure 5, typically the distance, d, is a few millimetres. A single hologram provides information about multiple planes within the scanning volume, however the specimen is not necessarily in focus. To obtain a focussed image of the specimen, the system defocus value should be known, but it can be difficult to determine this value. Currently, points as small as 1 µm have been resolved laterally. The depth resolution, however, is not nearly as good, and requires an accurate knowledge of the defocus of the specimen [16]. Point source DIH microscopes have been used to study microfluidics and living biological specimens, and work is being done to use them for atmospheric science to observe microscopic ice crystals [17]. Ongoing research is attempting to improve the resolving power of the DIH microscope. The theory behind the concept is as follows [16]. For the incident time-varying laser light, the scattered wave amplitude, $A_{scat}(r,t)$, and the spherical reference wave, $A_{ref}(r,t)$, interfere at the detector. They combine according to the *superposition principle* and the resulting interference pattern is given as:

$$\tilde{I}(r) = \left|A_{ref}(r,t) + A_{scat}(r,t)\right|^2 - \left|A_{ref}(r,t)\right|^2 \quad (3)$$

$$= \left|A^*_{ref}(r,t)A_{scat}(r,t) + A_{ref}(r,t)A^*_{scat}(r,t)\right| + \left|A_{scat}(r,t)\right|^2 \quad (4)$$

where: $\widetilde{I}(r)$ is the intensity (irradiance) at distance r from the pinhole source

The first term in equation (4) contains the interference between the scattered wave and the unscattered reference wave. The second term in equation (4) contains the interference between scattered waves only. Therefore, the first term contains the important holographic information that can be used to reconstruct the specimen information. The goal is to obtain the 3D structure of the specimen by reconstructing the wavefront at the specimen. This can be achieved by using the Kirchoff-Helmholtz transform [19], which is given as:

$$K(r) = \int_S d^2\xi \; \widetilde{I}(\xi)\, e^{\left(2\pi i \xi \cdot r / (\lambda \xi)\right)} \tag{5}$$

where: the integration extends over a 2D surface with coordinates $\xi(X,Y,Z)$
L is the horizontal distance from the source (pinhole) to centre of detector
$\widetilde{I}(\xi)$ is the 2D contrast image
K(r) is a complex function that represents the wavefront at the specimen

The *contrast image*, $\widetilde{I}(\xi)$, is obtained by taking the hologram measured with the specimen present and subtracting the reference hologram. Other reconstruction methods for confocal optical holography have been published by Lai [20] and Jacquemin [21]. Section 2.5.9 shows the reconstruction method used for acoustic holography.

2.1.5 Holographic Interferometry

Interferometry is simply the interference of two sources of waves. For example, Figure 6 shows Young's double slit interferometer [18]. This technique is analogous to the wavefront-splitting of a biprism, shown in Figure 3, except that Figure 3 used plane waves, whereas Figure 6 uses spherical waves.

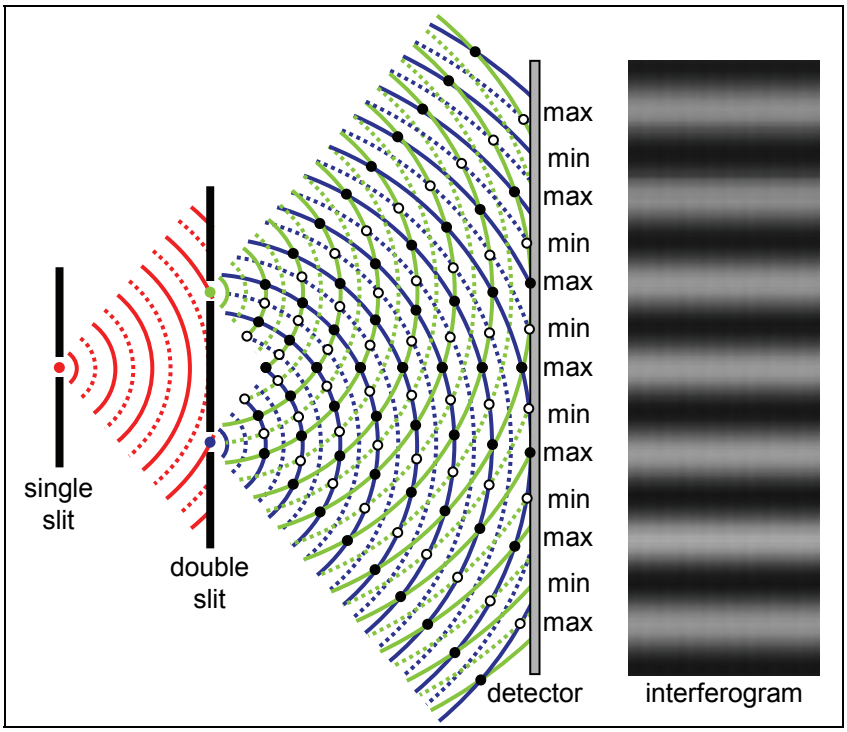

Figure 6: Young's Double Slit Interferometer [18]

In this diagram, a single point source on the left is converted into two coherent sources by the double slit. The two sources of spherical waves then overlap and interfere constructively (shown by black circles) and destructively (shown by white circles). The nature of the combination will change from place to place, simply because of the time it takes each wave to get from its source to the observation point. The pattern of maxima and minima at the detection plane on the right-hand-side is called an *interference pattern* or *interferogram*. The fringe spacing of the interference pattern is measured as the distance between successive maxima or minima. If the observation plane is moved closer (to the left in Figure 6), the fringe spacing will decrease. A specimen placed within the path of one of the beams will cause a relative shift in the phase of that beam and therefore also cause a shift in the fringes of the interferogram.

If several interferograms are collected by scanning a specimen internally, the amplitude and phase information for 3D points in the specimen can be stored digitally and reconstructed later. Knowledge of the specimen can convert the *relative* information into *absolute* information. In this case, the term *holographic interferometry* is used. For example, in a recent publication by Colambani and Bert [22], they describe a type of holographic interferometry, where the phase object is made to interfere with a memory of itself at a preceding time.

Some researchers use the term *holographic interferometry* interchangeably with *holography* and use the term *hologram* interchangeably with *interferogram*. For example, Figure 7 shows an optical interferometer, which is used to measure the temperature in a flame [23].

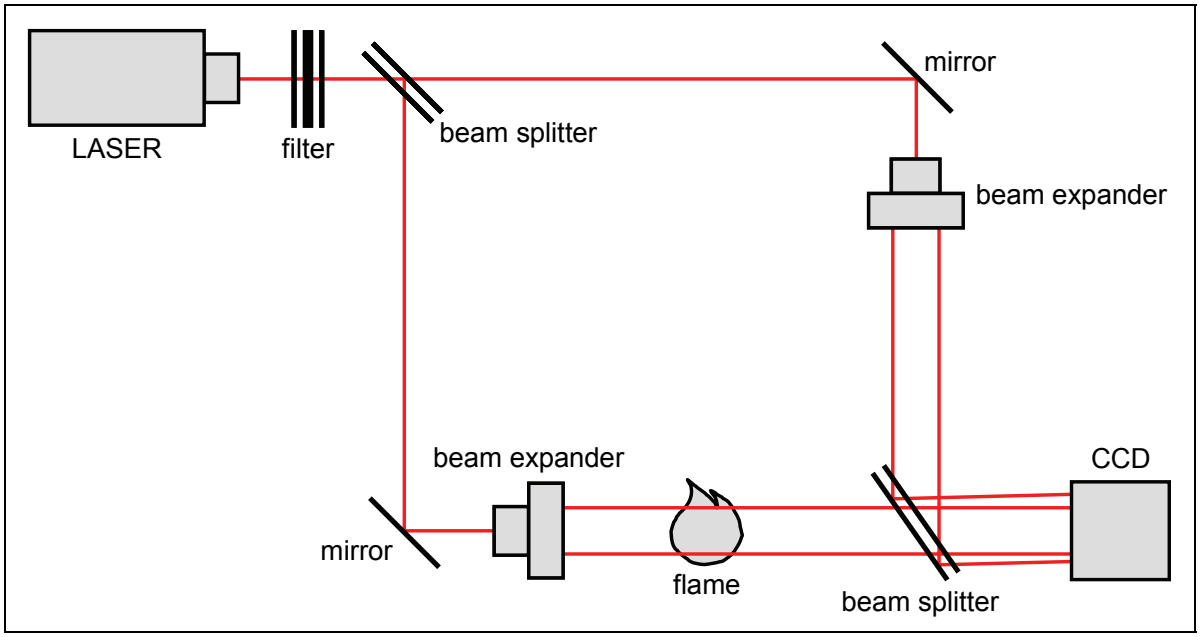

Figure 7: Off-axis Optical Holographic Interferometry system

In this case, the laser beam is amplitude-split by a beam splitter, which is in contrast to the wavefront splitting of Figure 3. This is also an off-axis system, in contrast to the in-line techniques shown previously. The object beam (the beam that probes the flame) and reference beam travel different paths before recombining at the detector. Therefore, the path lengths of the object and reference beam could be different. If the path lengths are different, the phase shift caused by the specimen can only be measured relatively. This instrument is technically an interferometer, however, the group has called their instrument an "off-axis digital holography system" [23].

To further confuse the terminology, in acoustics, holography usually refers to *Nearfield Acoustic Holography*, (described in section 2.4.1), where there is not even interference between an object and reference beam. Technically, the instrument designed in this thesis is a holographic interferometer. It is holographic because it measures both amplitude and phase for a 3D specimen, but it is an interferometer because the beams have different paths and different propagation conditions, hence the phase measurement is relative. However, to be consistent with the acoustic literature, I will use the terms holography and hologram to refer to the design and construction of the acoustic instrument in this document.

2.2 Confocal Microscopy

Confocal microscopy is a common technique used in optical systems. In this case, an aperture is set up between the specimen and the detector, which is *confocal* (*coplanar*) with an illuminated spot on the specimen, as shown in Figure 8, [24].

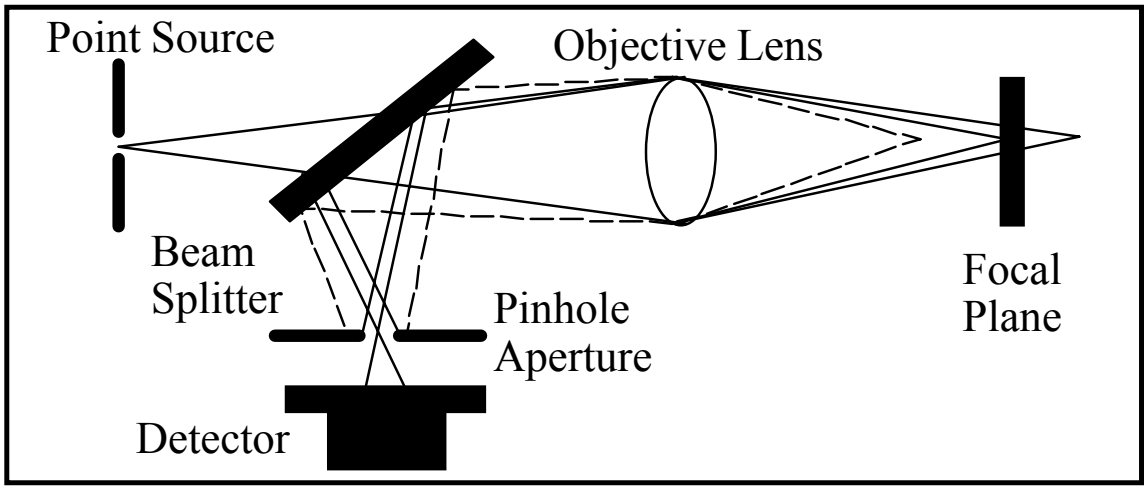

Figure 8: Confocal Microscopy (in Optical Systems)

In this figure, the source light rays from the left side are focussed by the objective lens to a focal point at the specimen on the right side. The reflected light from the specimen travels back through the objective lens, gets directed downward by the mirror, and passes through the pinhole aperture before it reaches the detector. The pinhole aperture blocks out the rays that are out of focus (shown by the dashed lines) and therefore sharpens the image over a narrow depth-of-field at that particular scanned focal plane position. Reconstructing the image over various scan positions along the axis of depth can provide a composite image in which all points are in good focus. The advantage of a confocal configuration is that you can take an accurate measurement of a single desired point in the specimen, while minimizing noise from aberrant rays. Confocal scanning through the points in the specimen allows the measurement and collection of a 3D map of intensity information.

The key feature that allows the observation of depth information on a specimen in confocal microscopy is the presence of a convergent beam (also known as a *cone* beam), rather than a collimated beam (also known as a *parallel* beam). Figure 9 illustrates the difference between a collimated beam (top) and convergent beam (bottom) incident on a spherical specimen [25].

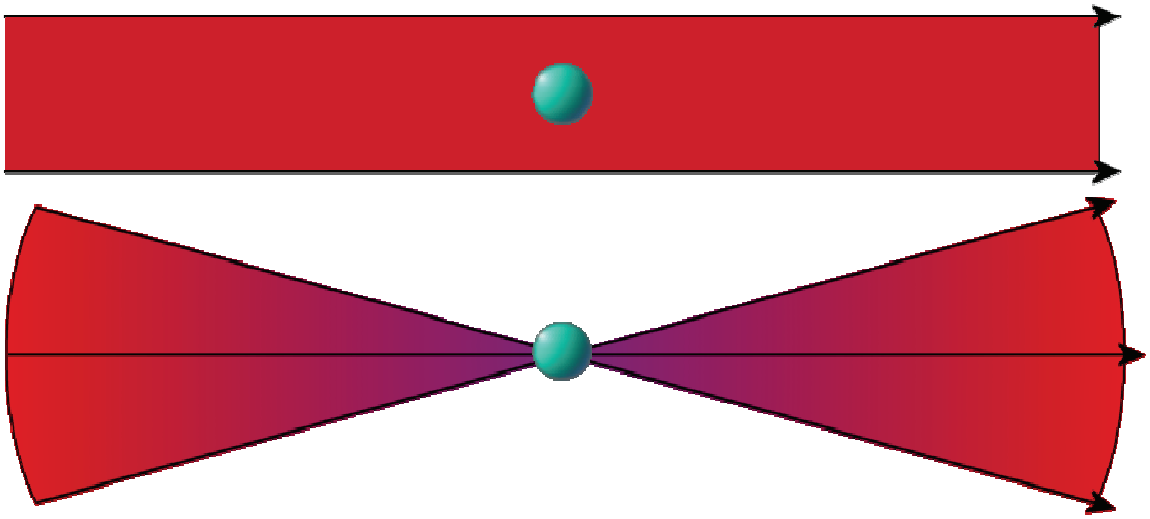

Figure 9: Collimated vs Convergent Beam

For the collimated beam (top), if the specimen shifts to the left or right, there would be no change in the output image on the right-hand side. This is because the same rays are passing through the specimen regardless of its horizontal position. This is not the case for the convergent beam (bottom). For the convergent beam, all rays pass through the specimen when it is at the focal point of the beam, however, if the specimen is moved to the left or right of the focal point, only some of the rays will pass through the specimen. Hence, it is possible to distinguish between different horizontal locations of the specimen by looking at the output image. In other words, the convergent beam allows collection and extraction of depth information about the specimen, whereas a collimated beam does not. The same idea applies if the sphere shown above was a small volume element (*voxel*) within a larger specimen. A larger convergence angle improves the depth resolution of the instrument. Hence, a convergence angle that is as large as possible is desired for the CAHM design. The difference in the holograms produced by the cases shown above is investigated further in section 4.9.

2.3 Ultrasonic Imaging

Acoustic imaging techniques are advantageous to optical imaging when the sample being measured is opaque to light. Sound waves can propagate considerable distances in dense liquids and solids where light cannot enter [18]. Ultrasonic imaging is considered non-invasive and has been used in medicine and Non-Destructive Testing (NDT) for over 50 years. Ultrasound refers to pressure waves with frequencies higher than 20 kHz. Typically, medical ultrasound uses frequencies up tens of MHz and NDT uses frequencies up to hundreds of MHz [26].

Two different kinds of systems exist for creating ultrasound images, reflective or transmissive. In reflective imaging, sound scattered from acoustic impedance differences at boundaries between regions causes some sound to be scattered back toward the source. By timing the return signal relative to the transmitted signal, depth information can be obtained. For transmissive imaging, the sound waves travel through the entire specimen, as shown in Figure 10. Transmissive imaging can often show details from beyond the regions whose boundaries lead to reflective imaging [27]. However, large specimens, such as a human body will not allow transmission imaging, since the transmitted sound will scatter and attenuate significantly, especially for MHz frequencies [28].

2.4 Acoustic Holography

The first use of acoustic holography was reported by Pal Greguss in 1965 [29]. Greguss, like Gabor, was also from Hungary. The same year, Denis Gabor registered the first patents for acoustic holography [30]. The basic elements of an acoustic holography device are:

- the specimen, also known as a *phase object*
- a source of temporally coherent sound to *insonify* the specimen
- a reference source of sound that is coherent with the object beam
- an acoustic detector positioned at the beam overlap to detect the interference pattern

These elements are shown in Figure 10, [30].

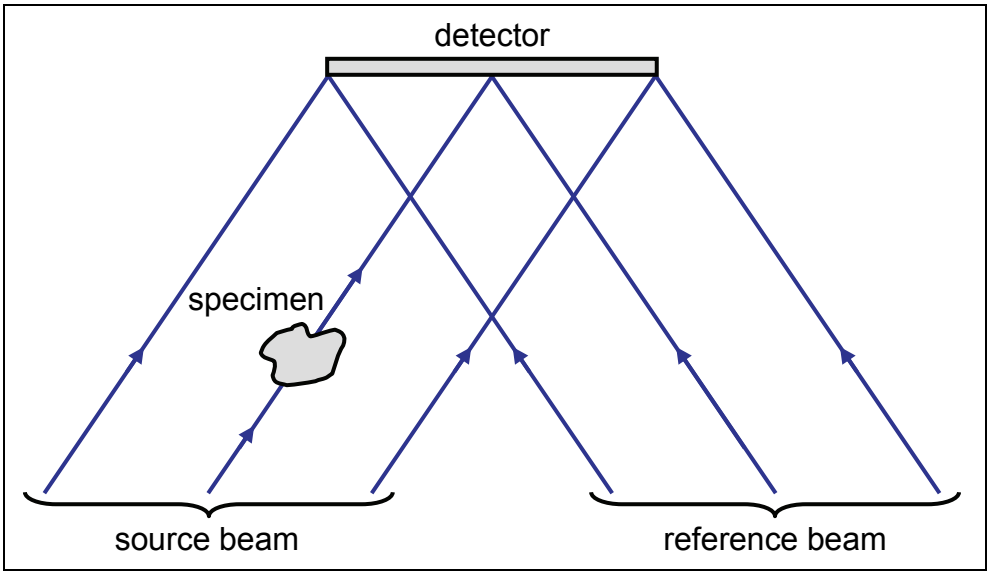

Figure 10: Basic Elements of Acoustic Holography Device

A specimen-modified (or object-modified) source beam is referred to as the *object beam*. The basic concept of acoustic holography is as follows: when a specimen is *insonified* (illuminated by sound), the scattered specimen wavefront will interfere with the coherent

reference wavefront to form an interference pattern at the detector plane. The specimen interacts with the beam of sound from the source through reflection, absorption, diffraction and refraction. The generated interference pattern changes over time, so a snapshot of the hologram and knowledge of the interaction and geometry of the setup can be used to reconstruct the specimen. Reconstruction could mean determining the shape and outline of specimen features, such as cracks, defects, membranes, etc. Or it could also mean determining internal properties of the specimen such as temperature, density, composition, strain, etc. To our knowledge, acoustic holography has not been used to measure internal temperature, which is one of the goals of the CAHM design.

In acoustic holography, it is only necessary to know the amplitude and phase in one plane. The amplitude and phase of the entire image volume can then be obtained via wavefront reconstruction, (see section 2.5.9). Hence, the location of the detector is not critical. However, it is desirable to place the detector in the location that has the greatest beam overlap, in order to get the greatest contrast in the interference fringes, as discussed in the experimental section 5.7.

The schematic layout in Figure 10 shows a collimated source beam, although a point source could also be used to insonify the specimen. Likewise, the reference beam could be either collimated or from a point source. Usually, off-axis reference beams are preferred because they help provide measurable depth information about the specimen. Off-axis beams with plane wavefronts can be simulated by shifting the phase of the oscillator signal in a manner that is related to the position of the detecting element in the detector plane [30]. One of the goals of the CAHM design is to obtain depth information by using a convergent object beam, (see section 2.2). Acoustic lenses can also be used to converge a collimated sound beam to a specific focal point within the specimen, (see section 2.6).

It is not always necessary to use a real reference source of sound. For holographic systems in which the object beam is detected by piezoelectric transducers, the reference beam can be simulated by an electronic signal [30]. In a technique referred to as Temporal Reference Holography (TRH), no separate reference beam, either acoustic or electronic, is used. Instead, the signal at the detector at one instant is compared with the signal a half-period of the sound wave later. This is possible with acoustic waves because electronic equipment is fast enough to measure between wave cycles, which is not the case for optical holography, since the frequency of a light wave is much faster than the electronics used for detection.

In the past, the most popular type of ultrasonic holography detectors have utilized liquid surfaces and laser optics to optically image the sound wavefront. In the early acoustic holography literature from the 1960s and 1970s, some researchers refer to acoustic holography as a means of "converting" an ultrasonic field (phase and amplitude) into an optical field [31]. The optical image was viewed in real-time or combined with light from a laser source and photographic film to record the hologram. The hologram could then be illuminated afterwards with coherent light to form an image. However, this method only provided a 2D image and no useful depth information [27]. It also had the problem that the resulting optical hologram was demagnified with respect to the original acoustic hologram, and the magnification factor was often not known exactly [27]. Since the origins of this technique, however, new advances in detection technology now allow the digital collection and storage of an ultrasonic field, which is much more useful than using optical conversion and film.

2.4.1 Nearfield Acoustic Holography

The term *Nearfield Acoustic Holography* (NAH) is often used interchangeably with *Acoustic Holography*. However, the term *Wave Field Extrapolation*, which is less used, would better illustrate its meaning. NAH is the name given to the reconstruction of the phase and amplitude of all or part of a sound field by measuring the amplitude and phase of the field in a single plane and performing a mathematical back-projection. Interference with a reference wave is not required. It is possible to do this in acoustics because a detector can oscillate fast enough to measure both the amplitude and phase of a sound signal and record them digitally, even for ultrasound frequencies (MHz range). On the other hand, optical detectors must make a time-average of the energy deposited by the rapidly oscillating electromagnetic waves, (~10^8 MHz).

One of the more recent developments in the field of acoustic holography was reported by Huang et al in 2005 [27]. Their technique uses a stationary specimen scanned by a single *needle* detector through multiple positions, as shown in Figure 11.

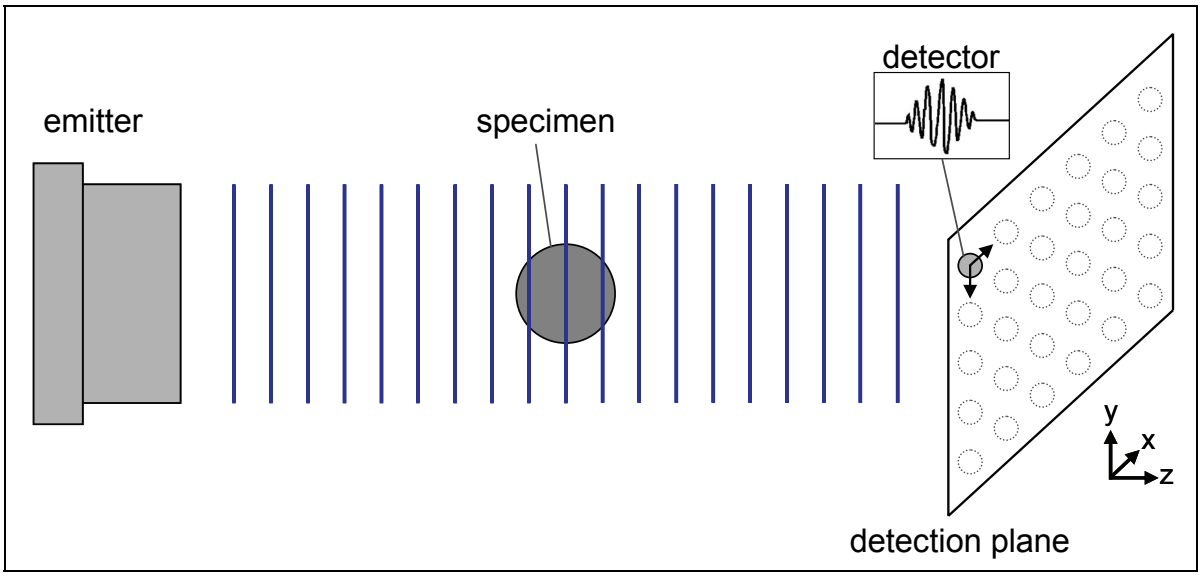

Figure 11: Nearfield Acoustic Holography (NAH) Method with Scanning

In this setup, the emitter and specimen remain stationary, while the needle detector is scanned through a 2D array of positions (shown as dotted circles) in the detection plane. From the single plane of amplitude and phase information, the wave field in any other plane, including a plane within the specimen, can be reconstructed. Huang et al used a 2 μs pulse of 5 MHz ultrasound and a detector with an active element diameter of 0.6 mm. The detector is placed within the nearfield of the sound field, (nearfield is discussed in section 3.3). The NAH method avoids the problem of poor depth resolution that plagued early acoustic holography instruments, (discussed in section 2.4). Huang et al were able to achieve a depth resolution of a few millimetres for this design.

The mathematical back-projection used in NAH is often referred to as an *inverse problem*. This reconstruction can be implemented by solving the *Rayleigh integral* for planar geometries or the *Helmholtz integral* for more complex geometries, both with the aid of the Fast Fourier Transform (FFT) [32]. The details of the reconstruction methods for NAH are given in section 2.5.9.

The method of scanning the detector to build up the holographic information can be time consuming, and thus it is not possible to measure dynamic specimens with this method. However, Huang et all also suggest that future advances in acoustic detector technology, such as an *acoustic camera* (2D imaging array), will allow faster detection and better resolution [27]. For example, the company *Optel* is in the process of commercializing an ultrasound camera, with a resolution of 0.1 mm or smaller [33]. This camera allows the observation of the near surface structures of solid objects and is currently used to measure fingerprints. Such a device would be a good candidate for use in an ultrasonic holography

instrument. In the future it should be possible to view internal features in a 3D specimen such as the human body, and observe small feature changes in real-time [27].

Another recent advancement in NAH was reported by Twerdowski et al in 2006 [34]. Figure 12 shows two methods used for ultrasonic Non-Destructive Testing (NDT) of semiconductor wafers [34].

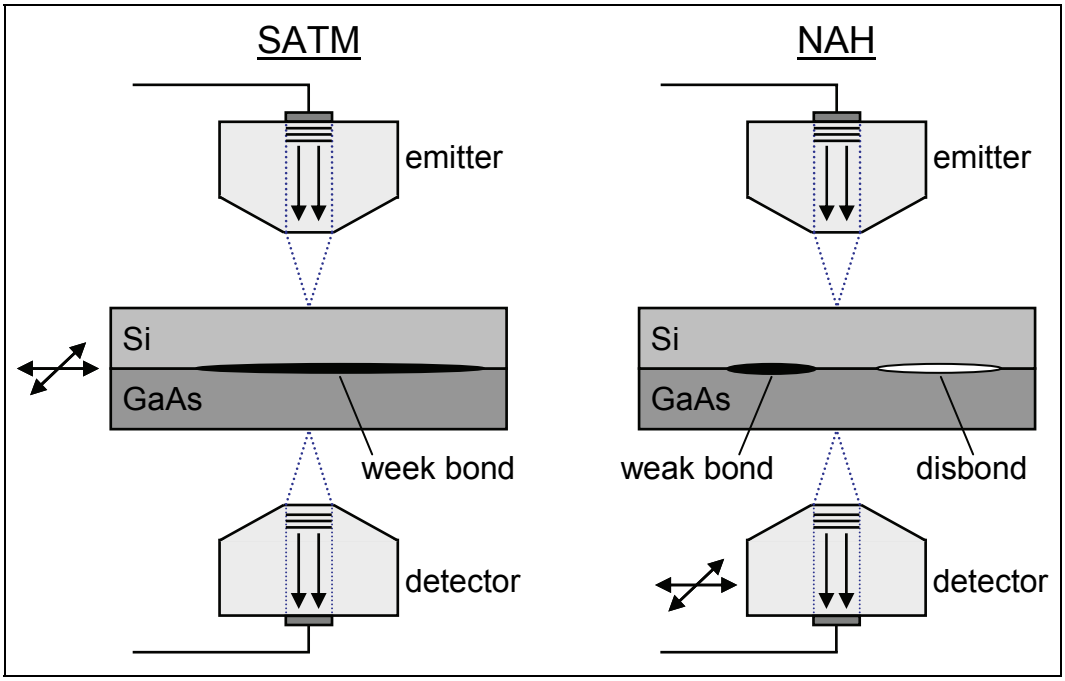

Figure 12: SATM and Scanning NAH for Non-Destructive Testing

The setup on the left side is typically used for Scanning Acoustic Transmission Microscopy (SATM) and the setup on the right is the more recent scanning NAH method. Both of these methods use a focussed beam to probe the specimen, whereas the design shown in Figure 11 used a collimated beam. The SATM method on the left of Figure 12, which has coaxial ultrasonic transducers and a moving specimen, can measure only amplitude information from within the specimen. However, the scanning NAH method on the right of Figure 12, which instead has a moving detector, can provide more useful information since NAH theory can be used to reconstruct the amplitude and phase inside the specimen. Furthermore, conventional NDT methods employ only longitudinal sound waves. However, Twerdowski et al have developed a method that also takes advantage of the *transverse modes* that can be excited in solid specimens [34]. This can provided additional information about the specimen such as the presence of defects such as the *weak bonds* and *disbonds*, as shown in Figure 12.

2.4.2 Sample Acoustic Hologram

As an example, Figure 13 shows an acoustic hologram created (by the company *Holosonics Inc*) by measuring the reflection from a U.S. penny under water, [18].

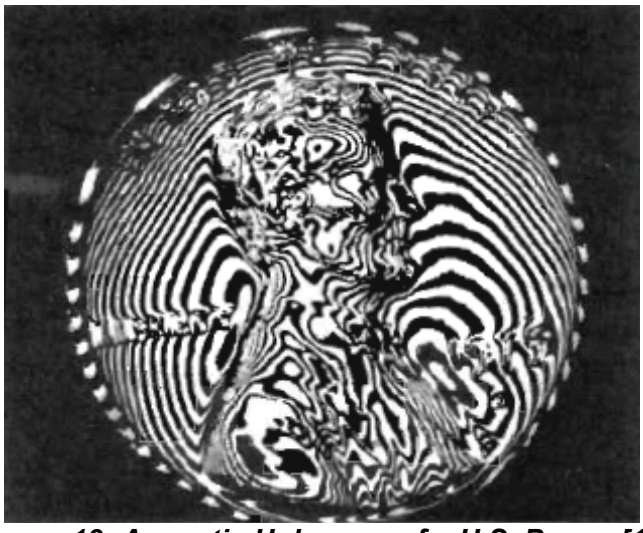

Figure 13: Acoustic Hologram of a U.S. Penny [18]

An ultrasound frequency of 48 MHz was used for this measurement, which corresponds to a wavelength of approximately 30 μm. Each spacing between fringes indicates a change in elevation (depth) of $\lambda/2$ or 15 μm. Hence, the holographic fringes produced by surface reflection can be interpreted as contour lines [18].

2.5 Introduction to Acoustics

The concepts of acoustics in the following sections are necessary in the understanding of designing and constructing an acoustic holography device. Most of this information can be found in introductory acoustic texts such as *Basic Acoustics* [35]. This was the primary text used, along with some other sources, as indicated in the following sections.

2.5.1 Speed of Sound

For the purpose of designing the instrument and performing accurate simulations, the speed of sound in the tank of water used in the lab should be known accurately. At atmospheric pressure, and at shallow depths, the speed of sound in distilled water as a function of temperature, can be approximated by the 6th order polynomial [36]:

$$\begin{aligned} c_{water} = {} & 1402.736 + 5.03358\,T - 0.0579506\,T^2 + 3.31636\cdot 10^{-4}\,T^3 \\ & - 1.45262\cdot 10^{-6}\,T^4 + 3.0449\cdot 10^{-9}\,T^6 \end{aligned} \tag{6}$$

where: c is the speed of sound (also known as the *sound speed*) in [m/s]
T is the temperature in °C

Assuming a room temperature of about 20°C in our lab, this corresponds to a speed of 1482.84 m/s. This is the value used in the design of the CAHM in section 3 and the simulations and calculations of section 4. The accuracy of equation (6) is confirmed experimentally in section 5.4.

2.5.2 Acoustic Intensity, Impedance, Pressure, Voltage

The *acoustic intensity*, also known as the *acoustic power intensity*, represents the power per unit area carried by an acoustic wave. Acoustic intensity of an acoustic plane wave in a fluid is defined as:

$$I(t) = \frac{p^2(t)}{\rho c} \quad \text{[Watts / m}^2\text{]} \tag{7}$$

where: p(t) is the time varying pressure in [Pa]
ρ is the specific density of the fluid in [kg/m^3]

The acoustic impedance of a fluid is defined as

$$Z = \rho c \quad \text{[Rayls] or [kg/m}^2\text{s]} \tag{8}$$

The speed of sound, and therefore the acoustic impedance, varies with the temperature, density, and pressure of the fluid. Therefore, an instrument that can measure variations in acoustic impedance (or sound speed) can be used to reconstruct the internal temperature and composition of a specimen. This measurement is discussed in detail in section 4.3.

An acoustic transducer will measure a time-varying voltage signal that is proportional to the pressure impinging on the transducer. To find the average acoustic intensity of a time-varying pressure wave, the *Root-Mean-Squared* (RMS) pressure is used:

$$I_{ave} = \frac{p_{rms}^2}{\rho c} \tag{9}$$

The RMS average of a pressure wave is defined as:

$$p_{rms} = \sqrt{\left(p^2\right)_{ave}} = \left[\frac{1}{T}\int_0^T p^2(t)\, dt\right]^{1/2} \tag{10}$$

where T is either a very long time or a single period of the repeating wave.

If a harmonic pressure wave is used:

$$p(r,t) = p_{\max} Sin(\omega t - kr) \quad \text{[Pa]} \tag{11}$$

where: p_{max} is the constant amplitude in [Pa]
r is the distance of travel of the acoustic wave in [m]
ω = is the angular frequency in [s^{-1}]
k = 2π/λ is the wavenumber in [m^{-1}]
λ is the wavelength in [m]
f is the frequency in [Hz]

The RMS pressure in this case is: $p_{rms} = \frac{p_{\max}}{\sqrt{2}}$, and the maximum intensity is: $I_{ave} = \frac{p_{rms}^2}{\rho c} = \left(\frac{1}{\rho c}\right)\left(\frac{p_{\max}}{\sqrt{2}}\right)^2 = \left(\frac{1}{\rho c}\right)\frac{p_{\max}^2}{2}$.

2.5.3 Refraction

As in optics, Snell's law determines the refraction of waves at an interface between two media, which comes from the requirement that the intensity at the interface must be continuous.

$$\frac{Sin\theta_1}{Sin\theta_2} = \frac{c_1}{c_2} \tag{12}$$

where: c_1 is the speed of sound of medium 1
c_2 is the speed of sound of medium 2
θ_1 is the angle of the incident ray to the normal
θ_2 is the angle of the refracted ray to the normal

For example, Figure 14 shows incident and refracted plane waves at an interface.

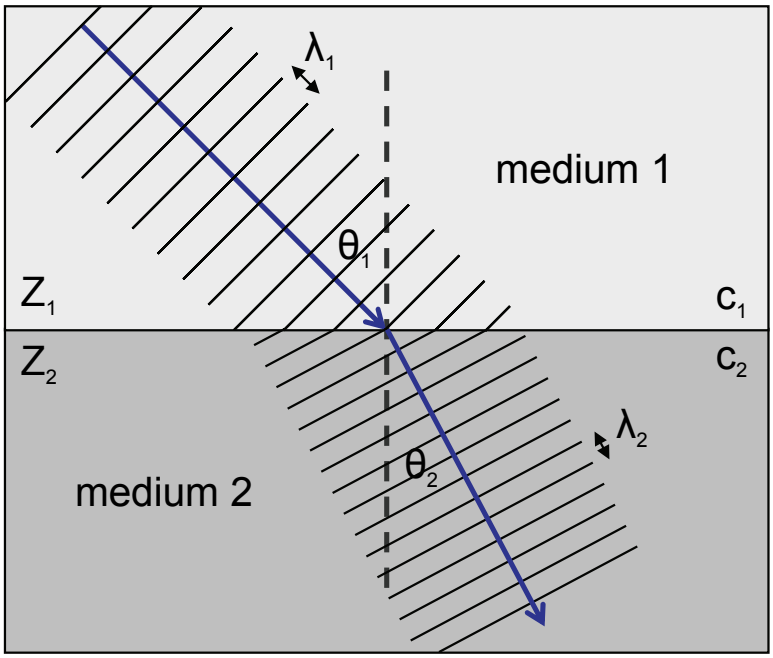

Figure 14: Refraction of Plane Waves at an Interface

Note that the wavefronts are continuous at the interface. In this particular example, the wavelength in medium 2 is smaller than the wavelength in medium 1. The speed of sound is related to the wavelength of the sound waves by:

$$c = f\lambda \tag{13}$$

where: f is the frequency of the sound wave in [Hz]
λ is the wavelength of the sound wave in [m]

Taking the frequency to be constant, then the wavelength will be proportional to the speed of sound. Therefore, if the speed of sound is different for the two media, then the wavelength will also be different. The plane waves can be represented by a single ray, parallel to the direction of propagation, as shown in Figure 14. Figure 15 shows a similar diagram, using only ray representations, and gives the result of Snell's Law for three different cases.

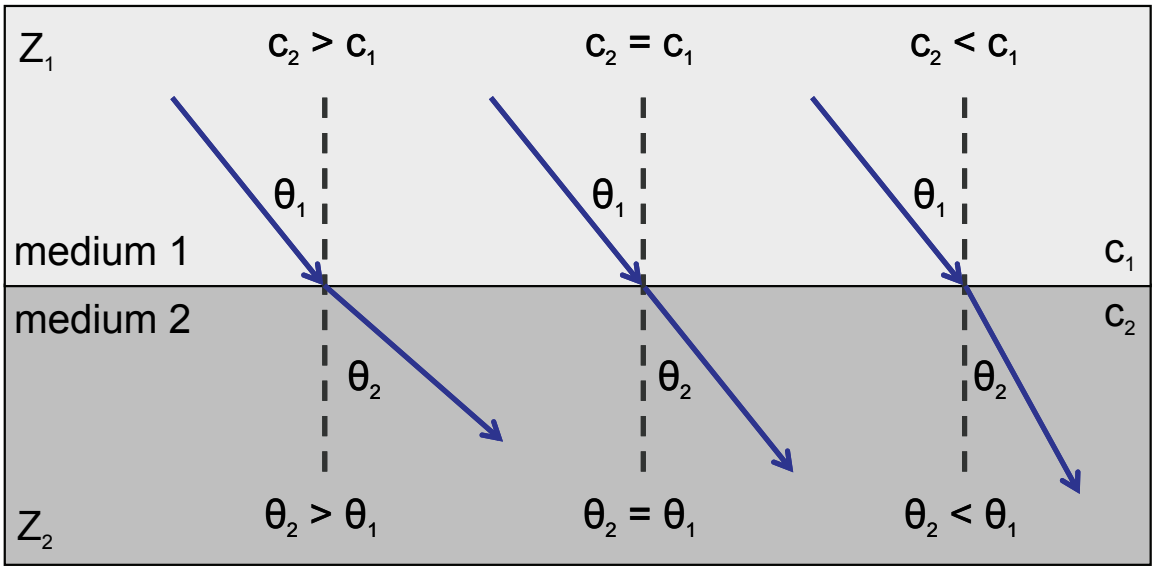

Figure 15: Snell's Law for Refraction at an Interface, 3 cases

In the middle of the diagram is shown the case when $c_1 = c_2$. In this case, the incident ray passes straight through the interface undeviated, as shown. When $c_2 > c_1$, the incident ray is refracted away from the normal, as shown. When $c_2 < c_1$, the incident ray is refracted towards the normal. This is the case shown previously in Figure 14. The refraction angle θ_2, does not depend on the acoustic impedances (Z_1 and Z_2) of the two media. However, they will affect the transmission and reflection intensities, as described in section 2.5.4. By setting θ_2 to 90°, and solving for θ_1, the critical angle can be found:

$$\theta_{crit} = Sin^{-1}\left(\frac{c_1}{c_2}\right) \tag{14}$$

This is the angle at which there is total reflection at the interface back into medium 1 and there is no sound penetration into medium 2. There is no refracted ray in this case. The same is true for all incident ray angles $\theta_1 \geq \theta_{crit}$.

2.5.4 Reflection and Transmission

When sound travels between two media, the amount of transmission and reflection depend on the acoustic impedances of the media, and the incidence angle. The reflected and transmitted intensity can be determined using the Rayleigh model [37]. According to this model, the intensity reflection coefficient is given as:

$$\alpha_R = \frac{I_3}{I_1} = \left(\frac{K_2 - K_1}{K_2 + K_1} \right)^2 \quad (15)$$

where: I_1 is the incident acoustic intensity

I_3 is the reflected acoustic intensity

$$K_1 = \frac{Z_1}{Cos\,\theta_1} \quad \text{and} \quad K_2 = \frac{Z_2}{Cos\,\theta_2}$$

The incident, reflected, and transmitted rays and their angles are shown in Figure 16.

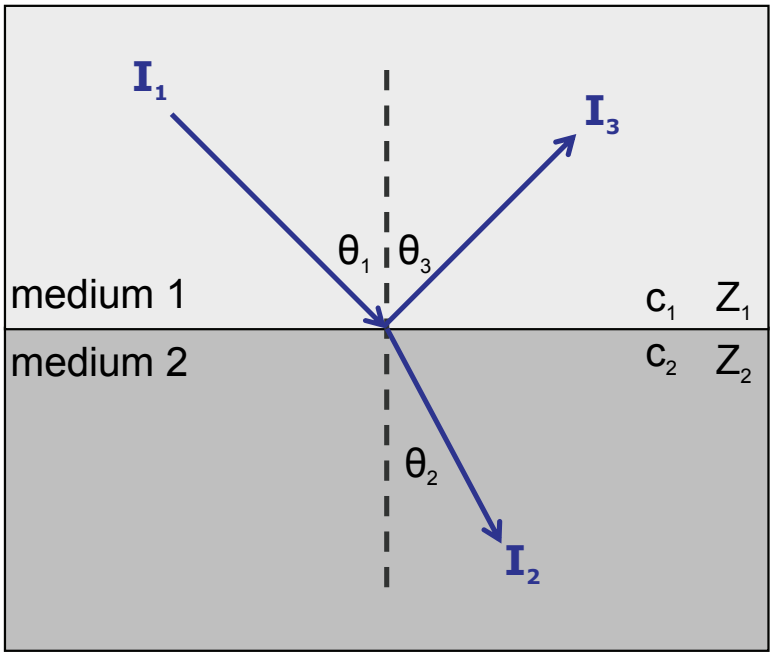

Figure 16: Sound Reflection and Refraction at an Interface Between Two Media

The angles θ_1, θ_2, and θ_3 are all measured to the normal, as shown. The refracted angle depends on incident angle, according to Snell's Law, equation (12). Since K_1 and K_2 depend on θ_1, therefore the reflected intensity varies with the incidence angle, and with the acoustic impedances (Z_1 and Z_2). The transmission coefficient also depends on these three values. It is given by:

$$\alpha_T = \frac{I_2}{I_1} = \frac{4K_1K_2}{(K_2 + K_1)^2} \quad (16)$$

where: I_2 is the transmitted (refracted) acoustic intensity

Assuming there is no absorption, the total incident intensity is the sum of the reflected and transmitted intensities. That is,

$$I_2 + I_3 = I_1 \quad \text{and} \quad \alpha_R + \alpha_T = 1 \quad (17)$$

In general, the phase of the reflected sound wave will vary with θ_1, Z_1, and Z_2. The phase shift of the reflected wave with respect to the incident wave can be found by taking the argument of the complex quantity given in equation (15). This phase shift is:

$$\Delta\phi = \arg(\alpha_R) = Tan^{-1}\left(\frac{\mathrm{Re}(\alpha_R)}{\mathrm{Im}(\alpha_R)}\right) \tag{18}$$

In general, there will be a reflection at the interface whenever $Z_1 \neq Z_2$, and $\Delta\phi$ will vary, depending on θ_1. For the special case when α_R is real, there is no phase shift of the reflected wave ($\Delta\phi = 0°$). This is true when $\theta_1 < \theta_{crit}$, that is when there is partial reflection and partial transmission. For the special case when $Z_1 >> Z_2$, complete reflection occurs ($\alpha_R = 1, \alpha_T = 0$), and the phase of the reflected wave is inverted ($\Delta\phi = 180°$), regardless of the incident angle. Total transmission occurs for an incidence angle called the *intromission angle* [38]. This angle can be found by setting $\alpha_R = 0$ and $\alpha_T = 1$, and solving for the above equations for θ_1. This gives:

$$\theta_{\mathrm{int}} = Sin^{-1}\left(\sqrt{\frac{(c_1/c_2)^2 - 1}{(\rho_2/\rho_1)^2 - 1}}\right) \tag{19}$$

2.5.5 Spherical Spreading

Any point source emitter will experience a loss of intensity with distance due to spherical spreading, (recall Figure 6). For intensity, this is given by:

$$\frac{I(r)}{I(r_0)} = \left(\frac{r_0}{r}\right)^2 \tag{20}$$

where: r is the distance from the emitter in [m]
r_0 is a reference position in [m]
$I(r_0) = I_0$ is the intensity at the reference position in [Watts / m^2]

In pressure units, the spherical spreading becomes:

$$p(r) = p(r_0) \cdot \left(\frac{r_0}{r}\right) \tag{21}$$

where: $p(r)$ and $p(r_0) = p_0$ are measured in [Pa]

The signal loss in decibels due to spherical spreading can be expressed as:

$$TL = 20\log(r) \quad \text{[dB]} \tag{22}$$

This quantity is called the *transmission loss*.

2.5.6 Absorption

Sound travelling in water experiences exponential decay of intensity with distance, according to:

$$I = I_0 \cdot 10^{\frac{-\alpha r}{10}} \tag{23}$$

where: I_0 is the acoustic intensity of the emitter [Watts/m^2]
I is the acoustic intensity at a location away from the emitter [Watts/m^2]
r is the distance from the emitter [m]
α is the absorption coefficient in units of [m^{-1}]

in pressure units, this becomes:

$$P = P_0 \cdot 10^{\frac{-\alpha r}{20}} \tag{24}$$

or, in units of decibels,

$$\Delta I_{dB} = \Delta P_{dB} = -\alpha_{dB} \cdot r \quad \text{[dB]} \tag{25}$$

where pressure and intensity are equivalent on the dB scale.

Sound absorption in water can be modelled using the Francois-Garrison model, [39]. Using this model, the absorption coefficient can be calculated using the formulas:

$$\alpha_{dB} = A_1 P_1 \frac{f_1 f}{f_1^2 + f^2} + A_2 P_2 \frac{f_2 f^2}{f_2^2 + f^2} + A_3 P_3 f^2 \quad \text{[dB/km]} \tag{26}$$

where: $A_1 = \frac{8.86}{c} 10^{(0.78\,pH-5)}$ $A_2 = 21.44 \frac{S}{c}\left(1 + 0.025T\right)$

$A_3 = 3.964 \cdot 10^{-4} - 1.146 \cdot 10^{-5} T + 1.45 \cdot 10^{-7} T^2 - 6.5 \cdot 10^{-10} T^3$

$P_1 = 1$ $P_2 = 1 - 1.37 \cdot 10^{-4} z + 6.2 \cdot 10^{-9} z^2$ $P_3 = 1 - 3.83 \cdot 10^{-5} z + 4.9 \cdot 10^{-10} z^2$

$f_1 = 2.8 \sqrt{\frac{S}{35}} 10^{\left(4 - \frac{1245}{T+273}\right)}$ $f_2 = \frac{8.17 \cdot 10^{\left(8 - \frac{1990}{T+273}\right)}}{1 + 0.0018(S-35)}$

T is the temperature in [°C]
c is the speed of sound in [m/s]
f is the frequency in [kHz]
z is the depth in [m]
S is the salinity in [p.s.u.] or [ppt]

The total transmission loss, including spherical spreading and absorption, can be written as:

$$TL = 20\log(r) + \alpha_{dB} \cdot r \quad \text{[dB]} \tag{27}$$

2.5.7 Coherence

Two periodic signals that have a definite fixed relative phase relation are said to be *coherent*. This is often the case when two signals originate from the same source. In order to make an absolute phase-shift measurement via the interference of two beams, the beams need to be coherent. The coherence length of a source is defined as the distance within which two beams that are split from the source (which begin in phase with each other) remain in phase. If a phase shift between the two signals is detected within the coherence length, then it must be due to a path difference of the two beams. Modern lasers have coherence lengths on the order of kilometres. Commonly used ultrasound transducers also generate beams with long coherence lengths (on the order of meters), which is important for creating and measuring acoustic holograms.

In Holography, if the detection plane is moved further away from the source, the fringe pattern will begin to lose contrast. If the detector is then moved outside the coherence length of the source, the interference fringes will disappear. Coherence length depends on the coherence properties of the source and can also be influenced by disordered motion of the medium, such as turbulence along the path of the wave propagation.

2.5.8 Interference of Pressure Waves

The distinction between two coherent or incoherent sources makes a big difference in determining what the combined signal will be. For two incoherent pressure sources, the combined pressure signal will be:

$$p_{tot,rms}^2 = p_{1,rms}^2 + p_{2,rms}^2 \tag{28}$$

where the pressures are all measured as an RMS average, as given by equation (10). This is equivalent to saying that we may simply add the energies or the acoustic intensities of the two incoherent pressure waves. Using equation (9), this gives:

$$I_{tot,ave} = I_{1,ave} + I_{2,ave} = \frac{p_{1,rms}^2 + p_{2,rms}^2}{\rho c} \tag{29}$$

However, for coherent sources, this will be incorrect. For waves that are coherent, such as two waves that originate from the same source, the time-varying pressure signals add:

$$p_{tot}(t) = p_1(t) + p_2(t) \tag{30}$$

And therefore, using equation (7), the total intensity of the combined signals is:

$$I_{tot} = \frac{p_{tot}^2}{\rho c} = \frac{|p_1(t) + p_2(t)|^2}{\rho c} = \frac{|p_1(t)|^2 + p_1^*(t)p_2(t) + p_1(t)p_2^*(t) + |p_2(t)|^2}{\rho c} \tag{31}$$

which is not equal to equation (29), but will instead vary in strength between $(p_{1,\max} + p_{2,\max})^2$ and $(p_{1,\max} - p_{2,\max})^2$, [35]. The first of these two cases is called *constructive interference* (maximum cooperation) and the second case is called *destructive interference* (maximum cancellation). These two extremes occur for phase differences of 0° (in phase) and 180° (out of phase). This concept can be easily extended to pressure waves that are *pulsed*, rather than *continuous wave* (CW) signals.

2.5.9 Mathematical Methods for NAH

Nearfield Acoustic Holography (NAH) was described qualitatively in section 2.4.1. Some background information and mathematical methods used for reconstruction of the specimen

information in NAH are given in the following sections. The goal is similar to the optical reconstruction algorithm shown in section 2.1.4, except that the measured quantity in acoustic holography is pressure, rather than intensity (called irradiance in optical holography). The information in the following sections comes mainly from the text *Fourier Acoustics* [40].

2.5.9.1 Acoustic Wave Equation

For adiabatic processes, such as those in water, the wave equation for pressure in a fluid is:

$$\frac{\partial^2 p}{\partial t^2} = c^2 \nabla^2 p \tag{32}$$

where: $p(\vec{r},t) = p(x,y,z,t)$ is the time-varying pressure of a 3D acoustic wave

Equation (32) is referred to as the *Acoustic Wave Equation* (in the time domain). For a 3D plane pressure wave, the general solution to the Acoustic Wave Equation is:

$$p(x,y,z,t) = Ae^{i(\vec{k}\cdot\vec{r} - \omega_0 t)} = Ae^{i(k_x x + k_y y + k_z z - \omega_0 t)} \tag{33}$$

where: $\omega_0 = 2\pi f$ is the angular frequency of the pressure wave in [s^{-1}]

The position vector $\vec{r} = (x,y,z)$ is the observation point in the sound field in Cartesian coordinates. The detected time-varying pressure $p(x,y,z,t)$ is illustrated in Figure 11. The *wavevector* $\vec{k} = (k_x, k_y, k_z)$ gives the direction of the wave propagation. Its magnitude, called the *acoustic wavenumber*, is:

$$k = \left|\vec{k}\right| = \sqrt{k_x^2 + k_y^2 + k_z^2} = \frac{2\pi}{\lambda} = \frac{\omega_0}{c} \quad [m^{-1}] \tag{34}$$

where: $k_j = \frac{2\pi}{\lambda_j} = \frac{\omega}{c_j}$ is called the *trace wavenumber* in the j-direction

c_j is the *phase speed* of the trace wave in the j-direction

and all other variables are the same as those defined for equation (11). The trace wavenumbers k_x and k_y can be taken as independent variables, in which case k_z depends on them in the following way:

$$k_z = \pm\sqrt{k^2 - k_x^2 - k_y^2} \tag{35}$$

For an *evanescent* wave, which is a wave whose intensity decays with distance, equation (35) can be written as:

$$k_z = \pm i\sqrt{k_x^2 + k_y^2 - k^2} \tag{36}$$

where the imaginary factor comes from the negative square root.

2.5.9.2 Helmholtz Equation

If we take the Fourier Transform of the Acoustic Wave Equation (32), the resulting frequency domain equation is:

$$\nabla^2 P + k^2 P = 0 \tag{37}$$

which is known as the *Helmholtz Equation*. Note that the "P" symbol denotes the transformed pressure signal. The 3D plane wave solution to the Helmholtz Equation is:

$$P(\vec{r},\omega) = A(\omega)e^{i(\vec{k}\cdot\vec{r})} = A(\omega)e^{i\left(k_x x + k_y y + k_z z\right)} \tag{38}$$

which is now a vector function in k-space. $A(\omega)$ is an arbitrary constant. The solution to the Helmholtz Equation (37) for a plane evanescent wave is:

$$P(\vec{r},\omega) = A(\omega)e^{i(\vec{k}\cdot\vec{r})} = A(\omega)e^{-\left(\sqrt{k_x^2+k_y^2-k^2}\right)z}\, e^{i\left(k_x x + k_y y\right)} \tag{39}$$

The first exponential term indicates exponential decay of the amplitude along the z-direction, called the *evanescent component*. The second term indicates the direction of travel which is along $(k_x, k_y, 0)$, called the *plane component*.

2.5.9.3 Wave Field Extrapolation

The pressure signal in k-space can be written as a function of the two independent, wavenumbers: $P(k_x, k_y)$, which is known as the *angular spectrum*. Using this definition, the pressure distribution in the z = 0 plane can be expressed as a the sum of plane and evanescent wave components:

$$p(x,y,0,t) = \sum_{k_x} \sum_{k_y} P(k_x,k_y)\, e^{i\left(k_x x + k_y y\right)} \tag{40}$$

For a continuum of all possible wavenumbers, these sums need to be represented by integrals:

$$p(x,y,0,t) = \frac{1}{4\pi^2} \int_{-\infty}^{\infty} dk_x \int_{-\infty}^{\infty} dk_y\, P(k_x,k_y)\, e^{i\left(k_x x + k_y y\right)} \tag{41}$$

These two integrals represent two Inverse Fourier Transforms in k_x and k_y, respectively. Similarly, the angular spectrum can be defined as:

$$P(k_x,k_y) = \Im_x \Im_y \left[p(x,y,0,t)\right] = \int_{-\infty}^{\infty} dx \int_{-\infty}^{\infty} dy\, p(x,y,0,t)\, e^{-i\left(k_x x + k_y y\right)} \tag{42}$$

which is the 2D Fourier Transform of the pressure distribution $p(x,y,0,t)$. Therefore, we can compute the angular spectrum by measuring the pressure distribution in the z = 0 plane. From the angular spectrum, we can compute the pressure distribution $p(x,y,z',t)$ in any z = z' plane. This allows us to reconstruct the entire wave field $p(x,y,z,t)$ from the single plane measurement, using the following steps:

1) Measure the pressure distribution in a single plane: $p(x,y,0,t)$, as in Figure 11
2) Take the 2D FT: $\Im_x \Im_y \left[p(x,y,0,t)\right] = P(k_x,k_y)$
3) Multiply $P(k_x,k_y)$ by $e^{ik_z z'}$
4) Take the 2D IFT: $\Im_x^{-1} \Im_y^{-1} \left[P(k_x,k_y)\, e^{ik_z z'}\right] = p(x,y,z',t)$
5) Repeat steps 3 and 4 for all desired planes $p(x,y,z',t)$

Usually a specific region of interest of $p(x,y,z,t)$ is chosen for reconstruction. For example, the desired z = z' planes could be within a specimen. The term $e^{ik_z z'} = e^{ikz'}$ is called the *phase factor* and it accounts for the advance in phase of a plane wave travelling in the z-direction between the z = 0 and the z = z' plane. The procedure shown above can be easily modified if the original pressure measurement is made in any arbitrary z-plane, rather than the z = 0 plane. One of the restrictions of this mathematical reconstruction is that the original pressure measurement should be sampled at a very high spatial resolution, typically sub-millimetre resolution to achieve good results [41].

2.6 Acoustic Lenses

Sound waves can be steered and focused just like light beams. An acoustic lens works in the same way as an optical lens. A converging lens is thicker in the middle and thinner at the edges, as shown in Figure 17, [42]. A diverging lens is thicker at the edges and thinner in the middle.

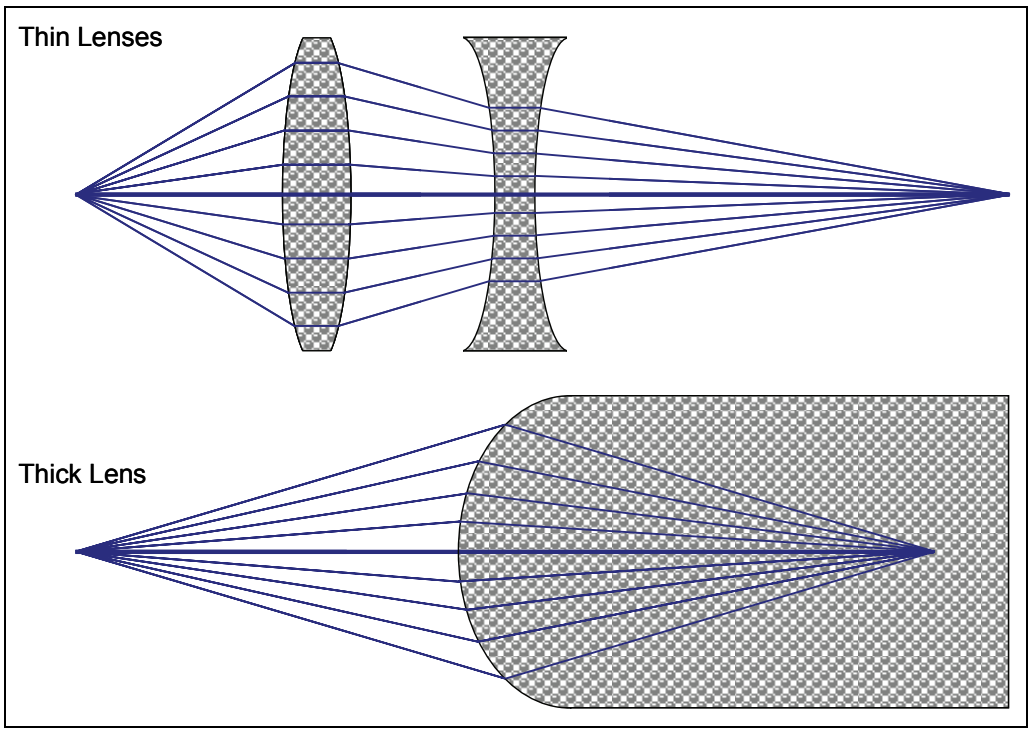

Figure 17: Acoustic Lenses

Sound originating in the outer medium enters the lens and passes through an array of tiny solid cylinders, which lowers the speed of sound. The incident wavefronts are then reradiated and redirected by the cylinders to either converge or diverge on the opposite side of the acoustic lens. As with optical lenses, Snell's Law defines the refraction at the interfaces. Acoustic lenses are differentiated into two types: thick and thin, as shown in Figure 17. Either type may be a compound lens, with multiple layers of materials of varying thickness or even varying sound speed.

The *discrete element* type of acoustic lens shown above was developed in the 1990s by several researches, including Fink [42]. This type of lens is prone to energy loss, since the discrete cylinders will absorb some of the acoustic energy. Presently, acoustic lenses are often made from a continuous medium, which can have its acoustic impedance matched closely with the specimen or with water. The acoustic impedance matching helps to eliminate acoustic energy loss. The *continuous material* style lens is usually made with plastics and can be easily machined by *CNC* (Computerized Numerically Controlled

machining). For example, a company called *Sound Metrics Corp* makes an underwater imaging device that utilizes acoustic lenses, as shown in Figure 18, [43]. The technology is called *DIDSON*, which stands for Dual Frequency Identification Sonar.

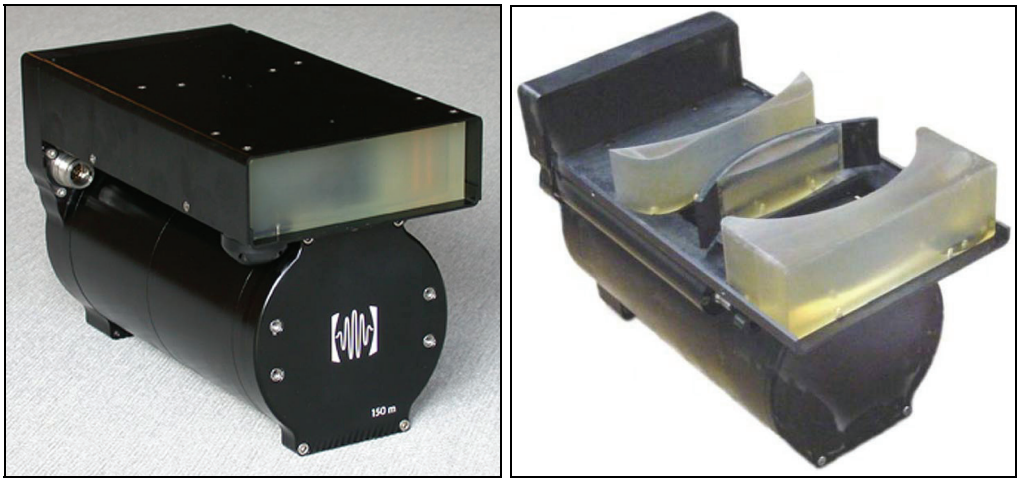

Figure 18: Sound Metrics DIDSON Underwater Ultrasound Imaging Device

The picture on the left shows a rectangular window, which projects an acoustic beam with 30° horizontal spread and 14° vertical spread. The picture on the right shows the internal design, which uses 3 polymethylpentene acoustic lenses with varying thicknesses. Sound Metrics has DIDSON models that operate at 1.1 and 1.8 MHz. If we were to make our own acoustic lenses in the future, we would want to use a material that is easily machine-able and has an acoustic impedance that is well-matched to water. The Zemax Optical Design software described in section 4 would be ideal for designing the acoustic lenses.

2.7 Micro Electromechanical Systems (MEMS)

Recent advancements in Micro Electromechanical Systems (MEMS) technology provide great promise for developments in precise ultrasonic devices. The possibility of using an array of tiny ultrasound emitters or detectors would provide significant advantages over the acoustic holography techniques used thus far. For example, increased resolution in sampling of the hologram would be possible.

An article published in 2000 [44], describes the construction of such a device. The company *Sensant Corp* is currently producing tiny ultrasonic transducers by depositing thin films of aluminium nitride on silicon substrates using molecular beam epitaxy. The films are mechanically flexed by applying small electric currents that generate sound waves in the high kHz range. With multiple-element arrays, electronic beam steering or focusing is possible, along with off-axis beam radiation. The article suggests that such a device will bring major advances to 3D ultrasonic medical imaging [44].

3 EXPERIMENTAL DESIGN

3.1 Confocal Acoustic Holography Microscope

Figure 19 shows a conceptual design of the Confocal Acoustic Holography Microscope [45].

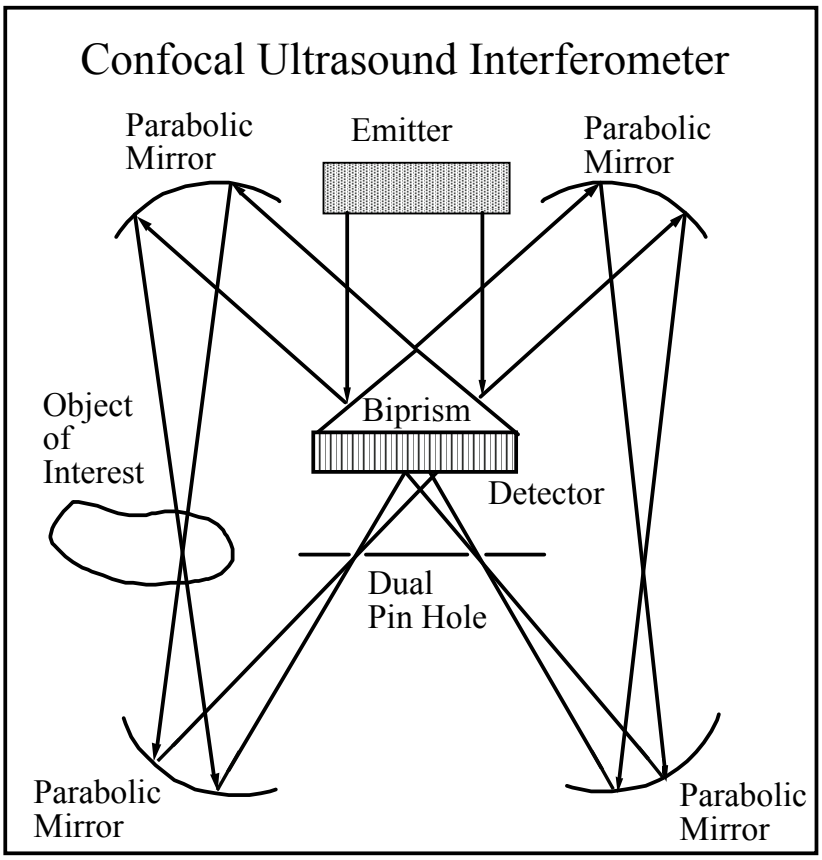

Figure 19: Schematic Diagram of CAHM

The instrument works in the following way: The emitter transducer emits plane waves towards the biprism. The biprism reflects and splits the wavefronts in half, which effectively creates two beams of equal intensity. The two reflected beams are then reflected by the first set of parabolic mirrors. One of the beams, called the *object beam*, passes through the target object (specimen) on the left side of the diagram. The other beam on the right-hand side, called the *reference beam*, passes through the reference medium, which in this case is water. The two beams are reflected by the second set of parabolic mirrors and then pass through a dual pinhole aperture. Finally, the two beams are overlapped at the detector and interfere to form a hologram.

The confocal label is given to the instrument because there is an aperture that is confocal (coplanar) with an illuminated spot on the specimen. The aperture only accepts sound rays from the object beam that have passed through the point of interest in the specimen. It

rejects rays from objects that are not in this focal plane. In other words, the pinholes form a virtual aperture around the focal point in the specimen, which block out-of-focus rays and aberrant noise. Scanning through the specimen allows the instrument to collect and construct a 3D map of information within the specimen.

The holography label is given to the instrument because there are two beams (probes), one passing through the specimen (object beam) and the other passing to the side of the specimen (reference beam). As a result, both amplitude and phase information can be extracted from the specimen, which allows the measurement of temperature and concentration gradients in a specimen. These measurements are possbile because the object beam is phase-modified, $\Delta\Phi$, depending on the speed of sound, c, of the specimen. When scanning through the specimen, a change in sound speed changes the phase of the object beam since the waves are either delayed or advanced with respect to the reference beam. This shows up as a fringe shift at the detector, as discussed in section 2.1.3 for optical holograms. The fringe shift is proportional to the change in sound speed (or change in refractive index) within the specimen. The calculation for this fringe shift for a simple specimen is given in section 4.3.

The microscope label is given to the instrument because it allows the measurement of the internal properties of the specimen with a resolution in the micrometer range. A frequency of 2.25 MHz has been chosen for the prototype design, which corresponds to a minimum attainable resolution of approximately 600 µm. However, future versions of the CAHM could be built to take advantage of even higher frequency ultrasound and finer resolution.

The fact that the reference beam on the right side of Figure 19 is also focussed to a point which is coplanar with the specimen, is not explicitly necessary to make the interference measurement. However, it makes the left and right side of the instrument symmetric, which means that the object beam and reference beam travel identical paths. Therefore, when no specimen is present, the object and reference wavefronts will be in phase.

3.2 CAD Model

Using the schematic diagram shown in the previous section as a starting point, a rough 3D layout of the instrument was produced using SolidWorks computer-aided design (CAD) software. The CAD model was created to use off-the-shelf components (mainly from the *Melles Griot* catalogue), along with some custom parts that will be machined by hand or

produced by CNC (Computerized Numerically Controlled machining). The preliminary 3D design of the CAHM, with approximate dimensions, is shown in Figure 20.

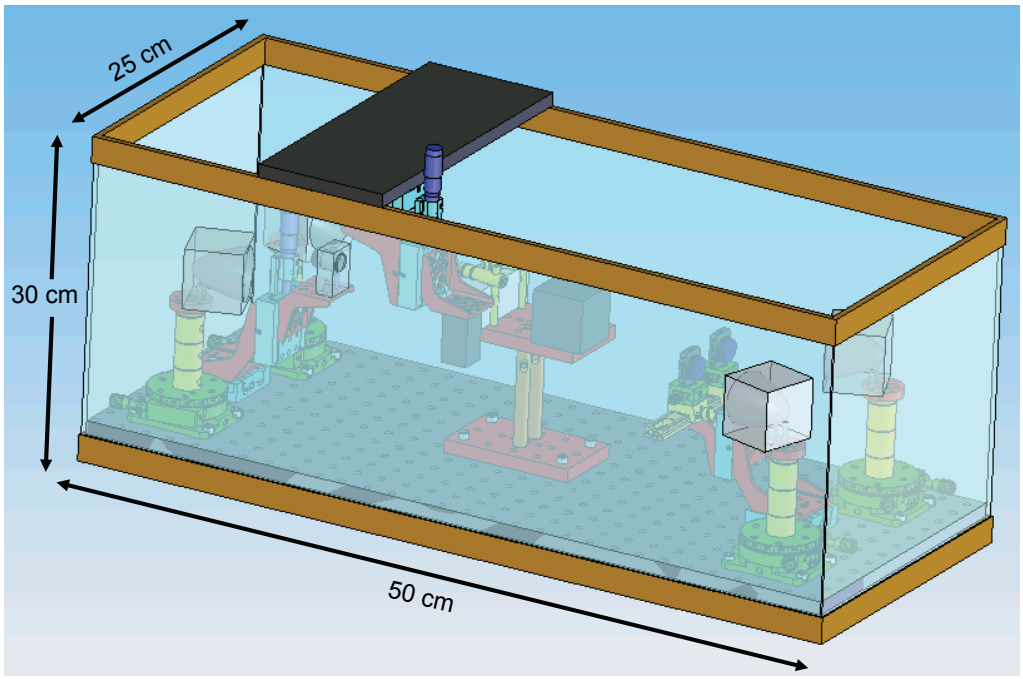

Figure 20: CAHM CAD Model with Water Tank

All components need to be submerged in a tank of liquid to allow propagation of the sound waves. Distilled water will be used to control the conditions of the propagating medium. The components shown previously in the 2D schematic drawing (Figure 19), are now shown as 3D entities in the CAD model. A black plate fixed to the top surface of the tank is used to mount the specimen. Since the water tank will be made of acrylic (as opposed to glass), machining of any of the tank surfaces can be easily performed. For example, machining will be needed to attach the black top-plate. Modifications of this type will likely be required in the future for add-on features such as a water pumping and purification system. Figure 21 shows the setup with both the water tank and the black top-plate hidden.

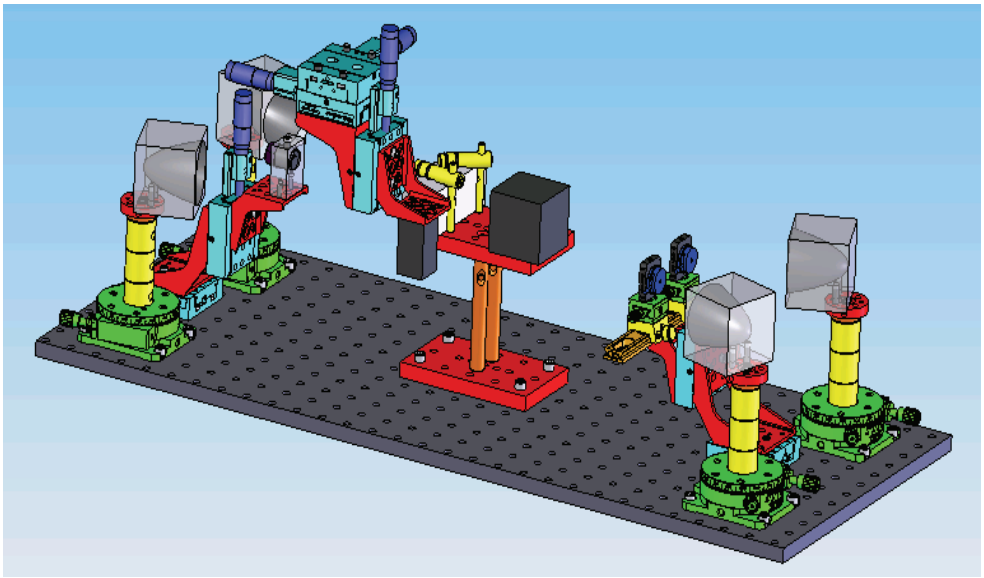

Figure 21: CAHM CAD Model (Water Tank Removed)

In the CAD model, the off-the-shelf components are shown as solid objects, and the components to be machined (parabolic mirrors and emitter transducer holder) are shown as transparent (in light gray). The specimen and detector are represented by black boxes, since their exact specifications and dimensions have not yet been determined. The detector will likely be the most expensive component. Detector selection is discussed in section 3.7. The parabolic mirrors will be made from aluminium by CNC machining. This CAD model can be sent directly to the machinist for production of the mirrors. The mirrors should be machined to a roughness smaller than the wavelength of sound used (λ = 659 μm). Figure 22 shows a top view of the CAD model.

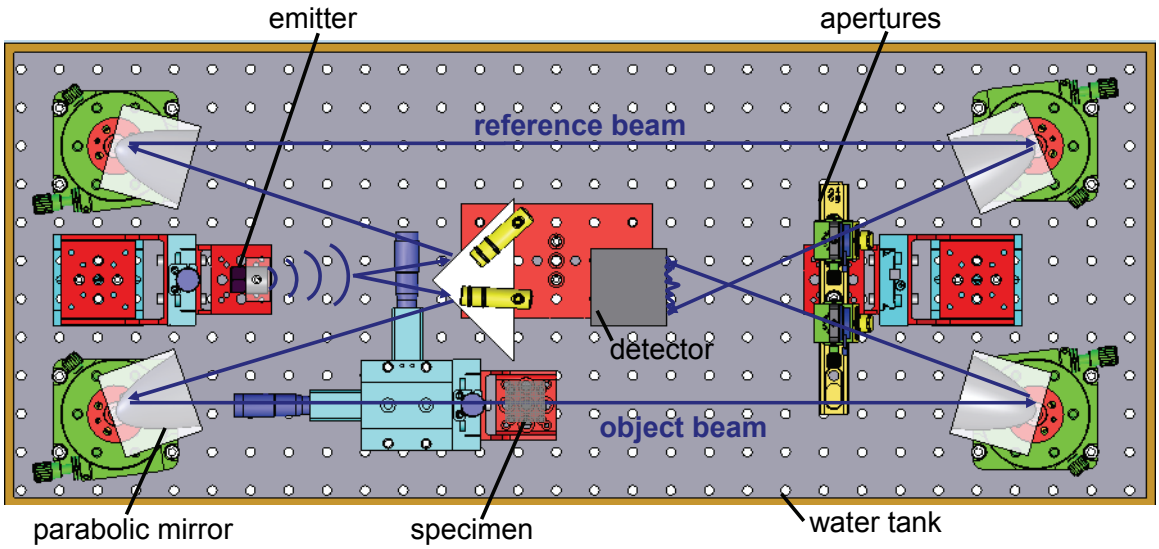

Figure 22: Top View of CAHM CAD Model

From the top, it is easier to see the resemblance of the CAD model to the original schematic, which was shown in Figure 19. As before, the emitted sound pulse gets split in half by the

reflective biprism (made of glass). The two beams then proceed to the first set of parabolic mirrors, where they are reflected. The object beam is focussed to a point within the specimen, while the reference beam travels through the reference medium (water). The two beams are then reflected by the second set of parabolic mirrors, pass through the apertures, and then overlap and interfere at the detector to form a hologram.

In the CAD pictures shown above, the 4 parabolic mirrors are fixed horizontally and vertically on the optical breadboard, and they have adjustable rotation stages. The centre stage holding both the biprism and the detector is fixed vertically and horizontally, as shown in the side view of the CAD model in Figure 23.

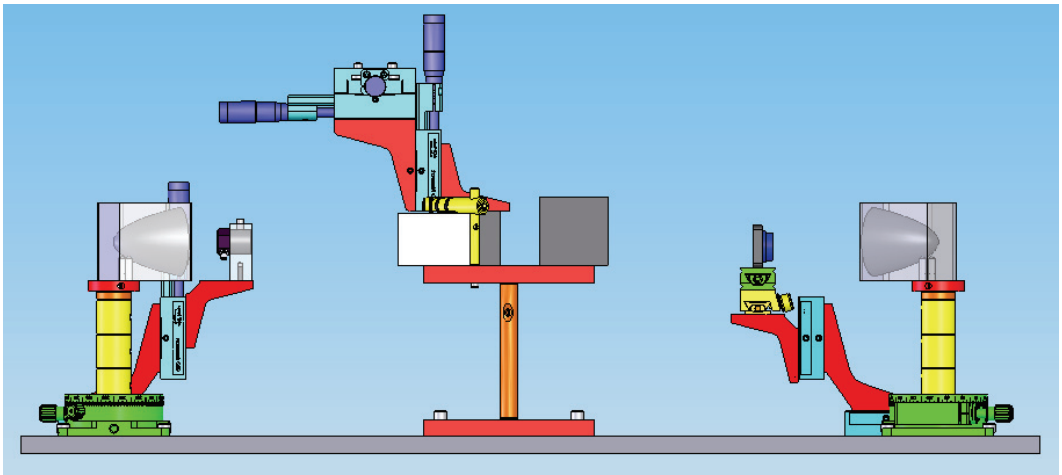

Figure 23: Side view of CAHM CAD model

The emitter, apertures, and specimen have adjustable 3D positioners to allow them to be aligned with the fixed parabolic mirrors, biprism, and detector. Note that the specimen mount has its 3 translation controls outside of the water, which allows the user to scan the specimen without getting his/her hands wet or disturbing the water surface.

When using the CAD software to model and design the CAHM, we must realise that just because the components align properly in virtual space, it does not necessarily mean they will align perfectly in practise. There are always small and unavoidable errors in the dimensions, positions, and orientations of the instrument components. Therefore, rather than designing an instrument that is always perfectly aligned, it is more desirable to chose a design that has many adjustments which can fine-tuned as needed. It is also advantageous to have a modular design that allows the possibility of adding enhancements (such as automatic scanning) in the future.

Note that unlike an optical laser system, the user cannot see the acoustic beam, which makes alignment of the CAHM much more difficult than an optical microscope. Only the

acoustic detector can be used to "see" the beam path. However, once the alignment procedure is complete, it would not need to be repeated often. On the other hand, it would be a good idea to verify the alignment approximately once a day. After alignment, the user would only need to access the 3 translation controls of the specimen mount. The alignment procedure is discussed in section 5.7.

Since this CAD model was produced before optimizing the component parameters, only rough dimensions and positions were used. However the CAD design was still very useful in determining which components need to be purchased, and to determine how they would all fit together. The actual positions and dimensions of the final instrument design will be discussed in section 4, as a result of the ray tracing optimization.

3.3 Emitter Transducer Selection

Since all measurements will be done by a single, fixed frequency, we prefer an emitter with a strong resonance centred on our chosen frequency. Also, we want the bandwidth to be as small as possible because we want to observe the interference at a single frequency (or a very small range of frequencies). Hence, we will want to make the pulse length long. The chosen frequency for the emitter is $f = 2.25MHz$. Using a speed of sound of 1482.84 m/s, this corresponds to a wavelength of $\lambda = 659\mu m$. For a desired bandwidth of approximately 10%, or B = 0.225 MHz, the quality factor is:

$$Q = \frac{f}{B} = 10 \tag{43}$$

Figure 24 shows a schematic diagram of the output of an ultrasound transducer [46].

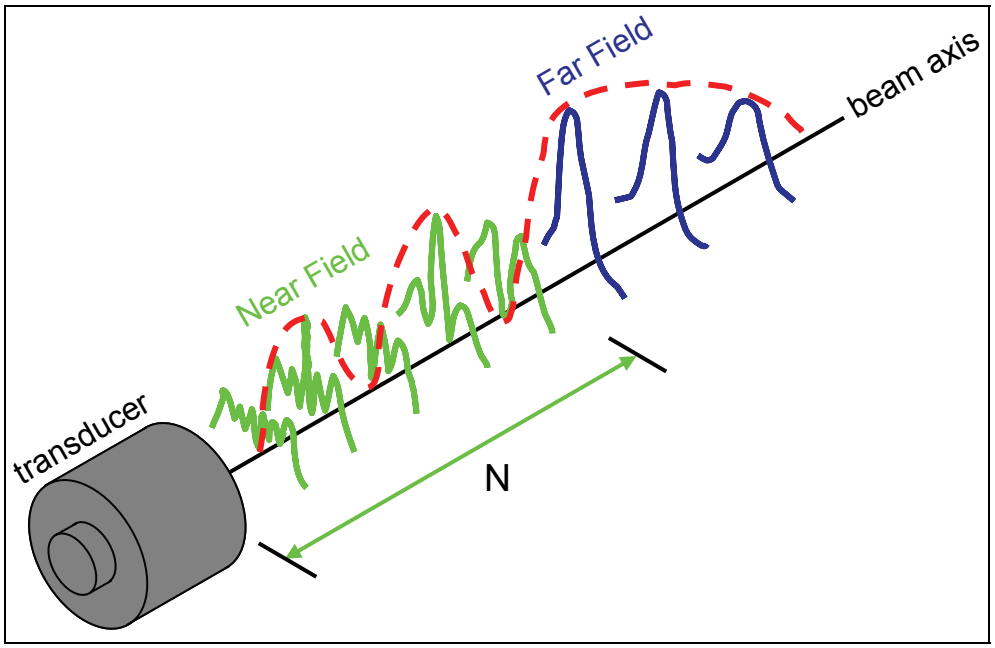

Figure 24: Ultrasound Transducer Beam Output

The solid lines show the pressure output by the transducer. The overall amplitude along the beam axis is shown by the dashed line. The amplitude in the nearfield fluctuates significantly, whereas in the farfield, the beam is more homogeneous, as shown by the dashed line. Hence, it is preferred to perform the measurements for the CAHM in the farfield of the emitter. We also require that the emitter face be as large as possible, in order to allow a large convergence angle when the object beam is focussed, as explained in section 2.2. The chosen emitter diameter is D = 1.5" = 38 mm. The nearfield distance of a circular transducer can be approximated by:

$$N = \left(\frac{D^2}{4\lambda} \right) \tag{44}$$

which corresponds to a nearfield of N = 54.5 cm. Hence, a beam path of 55 cm or greater is desired between the emitter and detector. The beam path will be discussed in section 4.1. The beam width (angular spread about the beam axis in the farfield), is given as:

$$\Omega = 2Sin^{-1}\left(\frac{0.514\,c}{f\,D} \right) \tag{45}$$

For the above parameters, and sound speed of 1482.84 m/s, this corresponds to a value of Ω = 1°. This small beam spread angle allows us to consider the source as approximately collimated, which means it emits a parallel beam of plane waves.

3.4 Absorption Considerations

Equation (26) was used, inputting the following parameters:

temperature	T = 20°C
speed of sound	c = 1482.84 m/s
frequency	f = 2.25 MHz
salinity	S = 0 ppt
depth	z = 1 m
pH	pH = 7

The attenuation coefficient was calculated as: α_{dB} = 1.114 dB/m. Since the total path length of sound in the proposed design is 55cm, we expect a drop of only 0.61 dB, which corresponds to a drop in intensity of only 13%, or a drop in pressure of only 7%. The voltage signal we will be measuring is proportional to the pressure. Therefore, absorption effects should be insignificant with the proposed with this design.

3.5 Spherical Spreading Considerations

The emitter transducer used in the experiments, although directional, will still experience spherical spreading loss. Using equation (22), and a path length of 55 cm, the transmission loss would be -5.19 dB. This corresponds to a intensity drop of 70% or a pressure drop of 45%. Thus, the voltage signal will drop 45%. Therefore, it should still be possible to detect the voltage signal at the detector without any problem.

3.6 Biprism and Mirrors

The currently available biprisms in our lab are made of crown (BK7) glass, with an acoustic impedance of 11.4 MRayls and a speed of sound of 5100 m/s [47]. Taking water (1.48 Mrayls, 1483 m/s) as medium 1 and the glass as medium 2, the Rayleigh equations of section 2.5.4 were used to plot the reflection and transmission vs incidence angle:

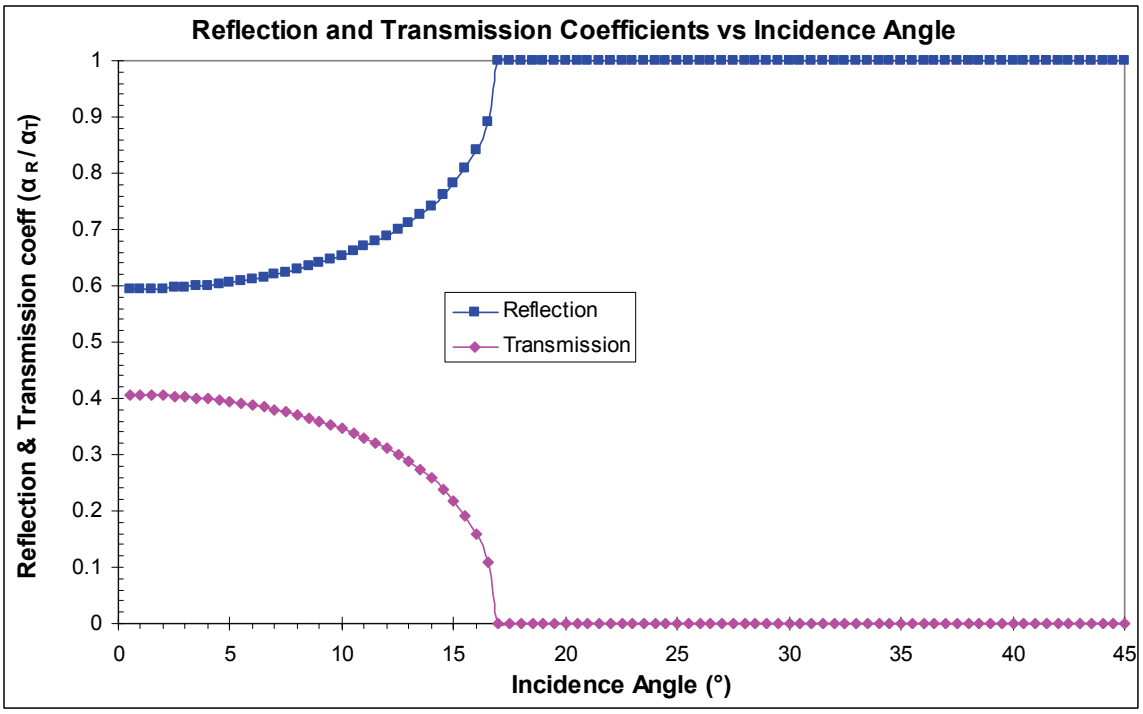

Figure 25: Reflection and Transmission Coefficients for BK7 Glass

The critical angle, from equation (14), is 17°. For incidence angles smaller than this, there is partial reflection and partial transmission into the glass. Beyond 17°, all incident sound is reflected and none is transmitted. Since 100% reflection is desired, we must use an incidence angle higher than 17°.

There are three possible biprisms currently available in the lab, with an apex angle of 130°, 135°, or 140°. For the 130° biprism, the incidence angle of a parallel beam, aimed at the biprism is 25°, as shown in Figure 26.

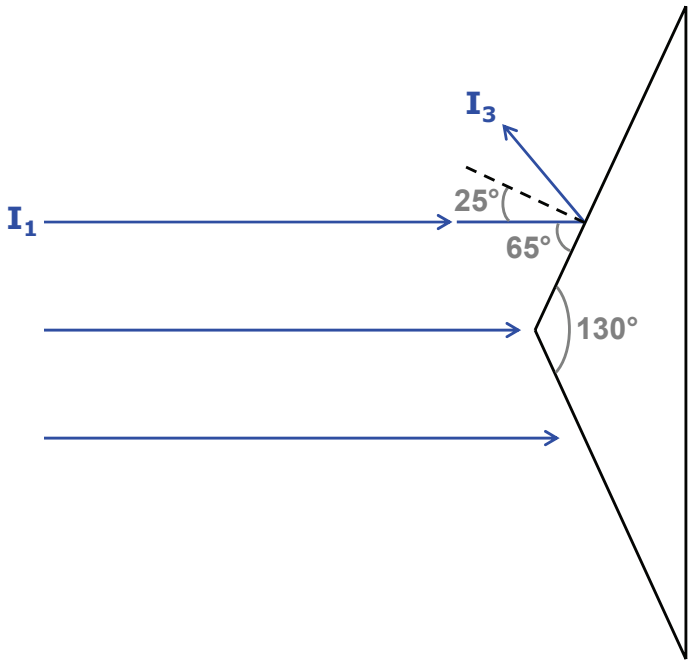

Figure 26: Reflection Angle at the Biprism

Since this incident angle is greater than the critical angle, we can expect 100% reflection from the biprism. The incident angle for the 135° biprism is 22.5°, and for the 140° biprism, it is 20°. Hence, all three biprisms would be suitable for constructing the CAHM. However, the 130° biprism is preferred because it allows the shortest path length between the biprism and the next two components (the parabolic mirrors).

3.7 Detector Selection

The detector that we have chosen to measure the holograms in the CAHM is a medical ultrasound probe with a linear array of elements, similar to the probe shown in Figure 27.

Figure 27: Linear Array Medical Ultrasound Probe

The probe, a V319 Phased array, made by Acuson is designed to plug into a medical ultrasound imaging machines. A medical ultrasound imaging machine typically costs $200,000 - $500,000, which is beyond the available budget of our project. The linear array has 128 elements with a pitch (element spacing) of 0.2 mm, for a total length of 2.56 cm. In the absence of a medical ultrasound imaging machine, an interface is needed to be able to control the probe using a computer. *Sonora Medical Systems* makes such an interface, called the *FirstCall Test System*, which is shown in Figure 28, [48].

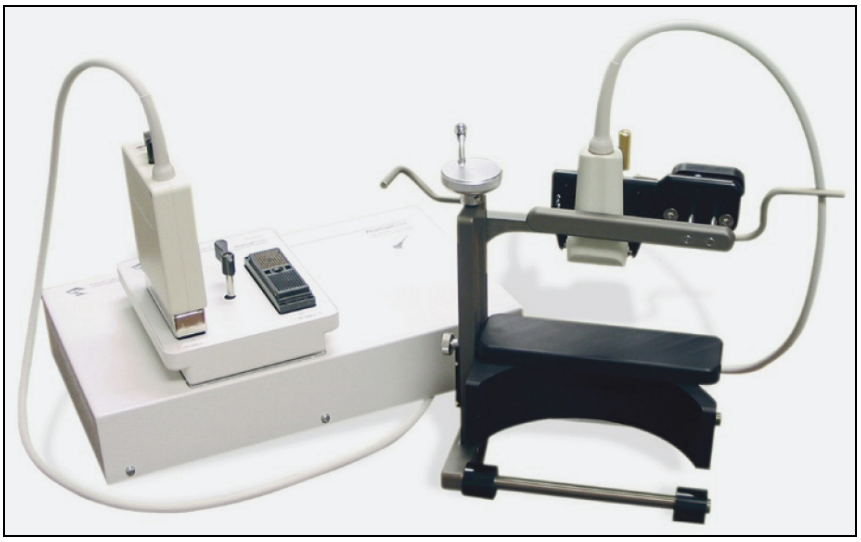

Figure 28: Sonora FirstCall Test System

This interface allows the user to control the input and output of all 128 elements in the probe with a computer using *LabView* software. For our instrument, we would likely only need to measure the received signals of the transducer elements and we would not need to transmit signals. This piece of equipment would be the most expensive element of the instrument. The total cost for this part, including the array probe and computer interface would be approximately $16,000.

3.8 Total Cost of CAHM

The total cost of the proposed CAHM design would be approximately $38,000, as shown in the following table.

Table 3: Total Cost Estimate of Proposed CAHM design

Items	Product Number	Company	Cost (CAN $)
Emitter Components			
2.25 MHz, 1.5" diameter High Power transducer	IL0212HP	Valpey Fisher Corporation	$563.00
Waterproof UHF/BNC cable, 6'	-	Valpey Fisher Corporation	$105.00
Computer Controlled Pulser-Receiver	5800PR	Olympus NDT	$7,200.00
Detector Components			
First Call phased array interface system	FC-2000	Sonora Medical Systems	$16,100.00
included: Acuson Dual Connector probe adaptor	AC-2		-
included: Acuson V319 Phased array	V319		-
Machining			
4 parabolic acoustic reflectors		Prototype Equipment Design	$1,400.00
other machining costs (bottom plate, adaptors, etc)		Prototype Equipment Design	$500.00
Opto-Mechanical Components			
3 Motorized Linear Stages	LTA-HL	Newport	$5,820.00
Solid Aluminum Optical Breadboard	07-BPM-503	Melles Griot	$479.00
4 Micrometer-Driven Rotation Stages	07-TRS-504	Melles Griot	$1,160.00
8 post holders	07-PHS-513	Melles Griot	$160.00
8 posts	07-RMS-002	Melles Griot	$80.00
3 Linear Translation Stages	07-TXS-723	Melles Griot	$864.00
2 Vertical Translation Stages	07-TEZ-703	Melles Griot	$1,092.00
2 Adaptor Plates	07-RPC-516	Melles Griot	$32.00
4 Single-Post Component Retainers	07-TTD-001	Melles Griot	$120.00
Right-Angle Bracket	07-TSH-504	Melles Griot	$84.00
Miscellaneous			
Computer + Monitor	EX262AA#ABA	CompuSmart	$1,000.00
SeaClear 20 or 50 Gallon Water Tank	605052	Petsmart	$220.00
Aptflex acoustic absorbing material - 3 sheets	F28	Precision Acoustics	$720.00
		Total Cost:	$37,699.00

4 SIMULATED RESULTS

4.1 Zemax Model

Zemax Optical Design (ray tracing) software was used to simulate the CAHM and optimize its design. For example, using Zemax, it was possible to optimize the curvature of the parabolic mirrors, the angle of the biprism, the positions of the components, the overlap of the object and reference beam at the detector, and the convergence angle at the specimen. Even though Zemax is meant for designing optical lens systems, by entering the appropriate parameters such as frequency and wave speed, it can be used for acoustic systems as well. Assuming a room temperature of 20°C in our lab, the speed of sound in water from equation (6) is 1482.84 m/s. The frequency used in the simulations was 2.25 MHz and the wavelength was 659 μm. The A top view of the Zemax layout for the CAHM is shown in Figure 29.

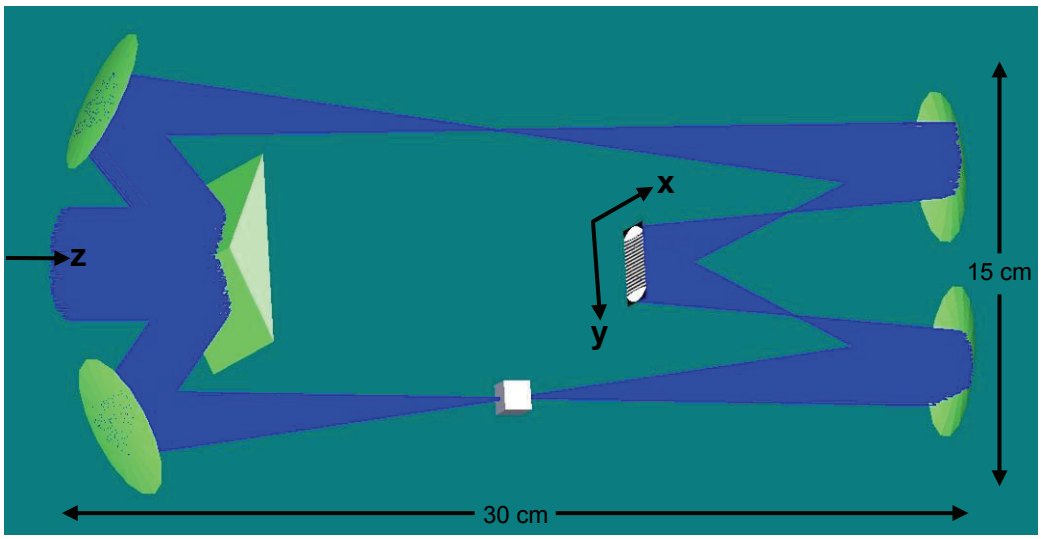

Figure 29: Zemax Layout for CAHM

In Zemax, the z-axis is used for the direction of the beam propagation, that is to the right. The y-axis is shown as down in this view, and the x-axis is out of the page. In the simulations, the emitter is assumed to emit parallel (collimated) rays. However, it would also be possible to include the actual beam spread angle if required, for example, Ω = 1°. The incoming collimated rays come from the left-hand side and get reflected and split into 2 halves at the biprism. The upper branch becomes the reference beam and the lower branch becomes the object beam. The specimen is represented by a cube with sides 1cm, and can be seen at the focal point of the lower branch. The object beam and reference beam overlap at the detector to form a hologram, as shown in the figure. The reference beam and object beam both have the same path length, which is 55 cm. The total length of this layout shown is approximately 30 cm, and the width is approximately 15 cm.

The Zemax prescriptions and relevant parameters of the simulated design are given in Appendix A. The 4 parabolic mirror surfaces can be exported from Zemax directly into the SolidWorks CAD model shown in section 3.2. The company Prototype Equipment Design, in Victoria, can machine the mirrors directly from SolidWorks model. The estimated machining costs were shown previously in Table 3.

4.2 Simulated Hologram

Some sample holograms for the Zemax design were produced by simulating the interference of the reference beam and object beam in the absence of a specimen. This is equivalent to setting the "index" of the specimen to n = 1, making it identical to the reference medium. The specimen index is defined and discussed in detail in section 4.3. The resulting interference pattern that is measured at the detector, with no specimen, is called the r*eference hologram*, and is shown in Figure 30.

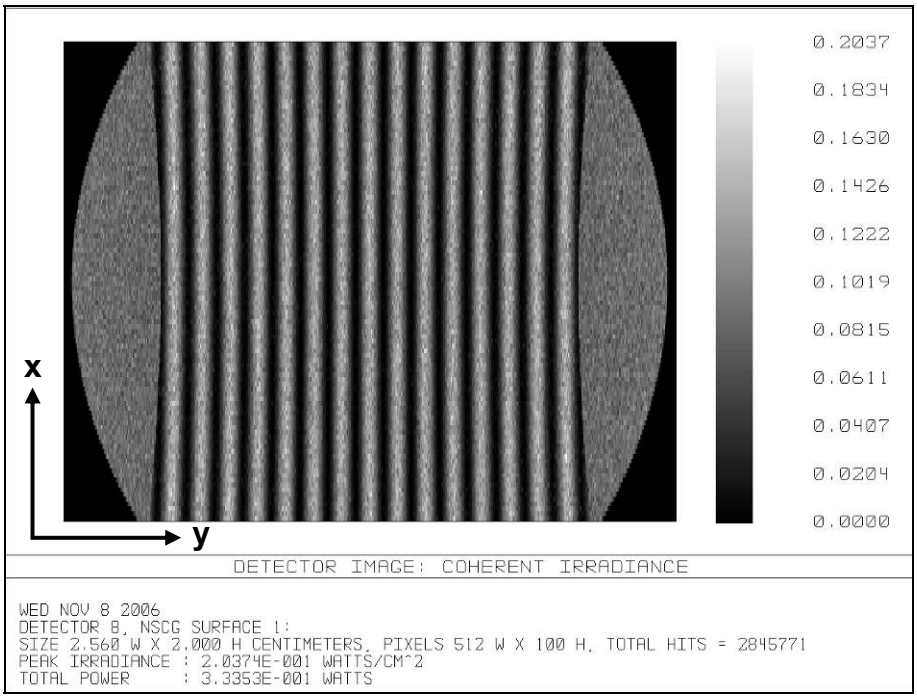

Figure 30: Reference Hologram for an Ideal 2D Detector

This diagram shows the variation of the intensity in the horizontal direction, which corresponds to the y-axis in Figure 29. Due to the geometry of the design, the hologram is symmetric in the vertical direction, which corresponds to the x-axis in Figure 29. The highest intensity is shown as bright (white) and the lowest intensity as dark (black), with grey-scale shades in between. In the water tank, the bright fringes would correspond to high relative pressure and the dark fringes would correspond to low relative pressure. The above hologram is for an ideal 2D detector. Since the detector we plan to use is a 1D linear array

and not a 2D array, the actual hologram we would expect to measure would look like the one in Figure 31.

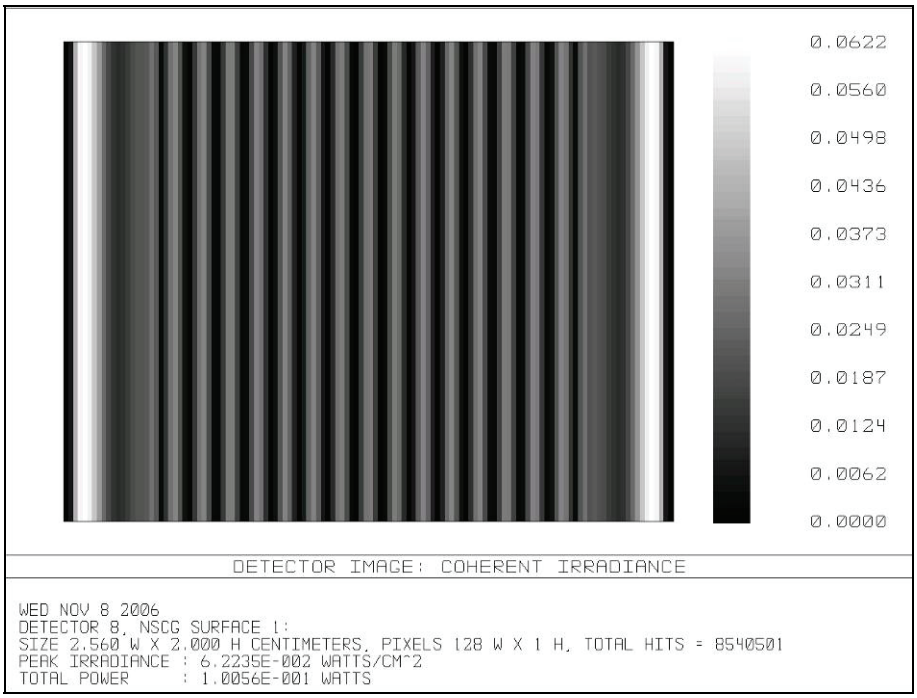

Figure 31: Reference Hologram for Linear Array Detector

In this simulation, the specifications of the linear array given in section 3.7 were used. The simulated detector is 128 elements with 0.2 mm pitch, which gives a horizontal width of 2.56 cm. The height of the elements is 2 cm. Clearly, the resolution in this hologram is poorer than the detector image shown in Figure 30. However, it is still possible to observe the fringes (variations of high and low intensity) in the hologram and this resolution is sufficient to be able to test the prototype design. The fringe spacing (distance between successive maxima or minima) is 1.2 mm. Therefore the resolution of the fringe shift measurements will be 0.2mm/1.2mm = 0.167 of a fringe shift, or 0.167 waves. The next section will discuss what this means in terms of resolution of the speed of sound measurements, and hence the resolution of the temperature or composition measurements.

4.3 Phase Delay and Fringe Shift Calculation

To determine the change in sound speed of the specimen that can be detected by the holography method, a simple calculation was done to determine the Δc that would cause a fringe shift of 1 fringe spacing. A shift of 1 fringe spacing means that a maxima (as shown in Figure 30 or Figure 31) will move to the left or right until it is in the position of the next adjacent maxima. The new hologram will look identical if the fringes are shifted 1 spacing, therefore accurate holography measurements can only be made for fringe shifts of less than

one fringe spacing. Note that a hologram shift of 1 fringe is also referred to as a shift of 1 *wave* or a *phase shift* of 360°.

For this calculation, the simplest case is considered, where the specimen is a solid cube of uniform material and constant speed of sound, and the object beam passing through the specimen is a parallel beam. Figure 32 shows a schematic diagram of the object beam, specimen, reference beam, and the resulting interference pattern.

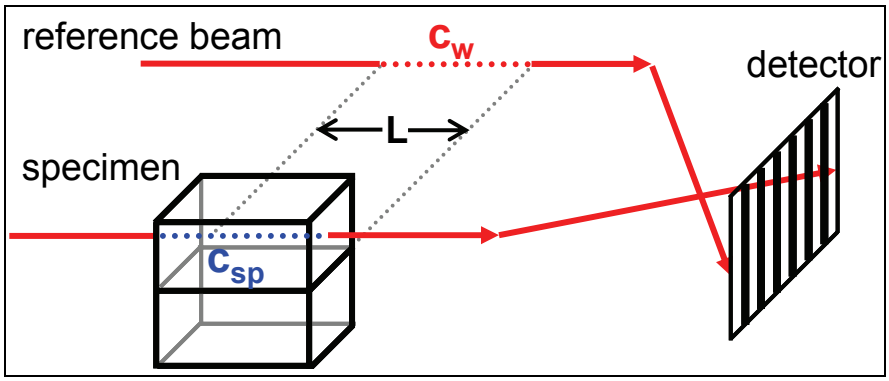

Figure 32: Phase Delay of Object Beam Caused by Specimen

The speed of sound ratio between the reference medium (water) and the specimen is:

$$\frac{c_w}{c_{sp}} = n \tag{46}$$

In optics, n is referred to as the index of refraction. This ratio of the speed of sounds will be referred to as the index throughout this report. For a specimen with index, n, the wavelength in the specimen is:

$$\lambda_n = \frac{\lambda}{n} \tag{47}$$

For thickness, L, of the specimen, the phase shift between the two beams is:

$$\Delta\phi = \left(\frac{2\pi}{\lambda_{sp}}\right)L - \left(\frac{2\pi}{\lambda}\right)L \tag{48}$$

The first term is the shift caused by the positive contribution due to the specimen and the second term is the negative contribution of an equal distance travelled in the reference medium. This total phase shift occurs for the case when the speed of sound is slower in the

specimen than in the reference medium. In the case where the speed is faster, the first term would be negative and the second term would be positive. This equation can be written as:

$$\Delta\phi = \left(\frac{2\pi}{\lambda}\right) L(n-1) \tag{49}$$

The condition for constructive interference is:

$$\Delta\phi = m\,2\pi\ , \tag{50}$$

that is, for the object beam delayed by an integer, m, number of cycles. Therefore, combining equations (49) and (50) results in:

$$L(n-1) = m\lambda \tag{51}$$

which is the condition for constructive interference, (a maxima or bright fringe). The hologram fringes will appear to shift 1 fringe spacing if the object beam is delayed by an additional amount of exactly 1 cycle, which corresponds to the condition:

$$m \rightarrow m+1 \tag{52}$$

If the model is now extended to include a specimen with 2 chambers, the first of constant index n_1 and the second of constant index n_2. When scanning between material 1 and 2, the Δn can be found which will cause 1 fringe shift. To find the change in index, Δn, that would cause this fringe shift, we can apply equation (51) to the two materials:

<u>for index 1</u>	<u>for index 2</u>
$m\lambda = L(n_1 - 1)$	$(m+1)\lambda = L(n_2 - 1)$

and combining these two equations gives the final calibration equation for the change in index per fringe shift of the hologram:

$$n_2 - n_1 = \Delta n = \frac{\lambda}{L} \tag{53}$$

Note that the fringe spacing did not appear in this calculation at all. Therefore, the fringe shift we would observe in the measured hologram, when scanning through the specimen, would not depend on the fringe spacing.

4.4 Separation of Temperature and Composition

A change in sound speed (or refractive index), as observed by a shift in the hologram fringes, could indicate either a change in temperature or a change in composition of the specimen. Holding temperature constant, a composition measurement of the specimen could be performed. Alternatively, holding composition constant, a temperature measurement could be performed. Previous work in optical interferometry by Abe and Iwasaki [49] showed that for many practical specimens, the change in refractive index can be broken into separate contributions due to composition changes and temperature changes, as in the following equation:

$$\Delta n \approx \left(\frac{\partial n}{\partial C}\right)_T \Delta C + \left(\frac{\partial n}{\partial T}\right)_C \Delta T \tag{54}$$

where the first partial derivative is the index change due to composition change (holding temperature constant) and second partial derivative is the index change due to the temperature change (holding composition constant). Assuming that equation (54) holds for a particular specimen, Abe and Iwasaki showed that it is possible to reconstruct both the temperature and the composition by using two different frequencies to probe the specimen [49]. In other words, if we measure a particular index change by scanning through a specimen, then we can solve for the two unknowns in equation (54) by performing the same scan a second time using a different frequency. In acoustic holography, this would also be possible by simply using a second emitter transducer. However, for the purposes of this research, the experiments were performed such that temperature was held approximately constant and only sound speed measurements due to composition were made.

4.5 CAHM Specifications

For λ = 659 μm, and a specimen cell size of L = 1 cm, equation (53) predicts an index change of Δn = 0.0659 per fringe shift (or per wave). For the proposed CAHM design, the minimum detectable fringe shift is 0.167 waves (from section 4.2), which means that the minimum detectable index change is Δn = 0.0659 x 0.167 = 0.011.

To get an idea of what this means in terms of the sound speed change in a specimen, we can assume c_w = 1483 m/s, which is the speed of sound of water at 20°C. Therefore, the weakest phase object that could be detected via a phase shift in the hologram fringes would need to have an index of 1.011 or 0.989. Using equation (46) this corresponds to a speed of sound of 1466.7 m/s or 1499.3 m/s. Therefore, the minimum detectable speed of sound change is approximately 16.3 m/s. The estimated minimum detectable temperature change can be found using equation (6), which works out to approximately 5.2°C for the above parameters. The estimated specifications of the CAHM, assuming a water temperature near 20°C, are summarized in Table 4.

Table 4: Estimated Specifications of Proposed CAHM (near 20°C)

Minimum Detectable Fringe Shift	Minimum Detectable Phase Shift	Minimum Index Resolution	Minimum Sound Speed Resolution	Minimum Temperature Resolution	Minimum Spatial Resolution
0.167 waves	ΔΦ = 60°	Δn = 0.011	Δc = 16.3 m/s	ΔT = 5.2°C	659 μm

As a prototype, these resolutions would be acceptable in order to prove the concept of the CAHM. However, in the future, we would expect to achieve much better sound speed and temperature resolution. This can be achieved by using a higher emitter frequency and a higher resolution detector. Array detectors with better resolution, smaller than 0.1 mm pitch, are currently being built for research [50] and will be available commercially soon. Typically in holography, small fringe shifts of 1/32 (0.0313 waves) or even 1/64 (0.0156 waves) can be measured with a suitable detector. For example, if we instead used a frequency of 10 MHz and a detector pitch of 0.1 mm, we can expect to achieve a spatial resolution of 148 μm, a sound speed resolution of 1 m/s and a temperature resolution of less than 0.5°C.

4.6 Specimen Parameters

For purpose of verifying the calculation made in the previous section, the value of Δn = 0.0659 per fringe shift was divided by 4 and a simulation was performed for several increments of 0.0659 ÷ 4 = 0.0165. Table 5 shows the simulation inputs and relevant parameters for these increments.

Table 5: Speed of Sound for Specimen at Different Temperatures

Δn	n	c_{sp} [m/s]	Δc [m/s]	ΔT [°C]
+0.0659	1.0659	1391	-92	-22.2
+0.0494	1.0494	1413	-70	-17.9
+0.0330	1.0330	1436	-47	-12.9
+0.0165	1.0165	1459	-24	-7.1
0	1	1483	0	0
-0.0165	0.9835	1508	+25	+8.5
-0.0330	0.9671	1533	+51	+17.5
-0.0494	0.9506	1560	+77	+24.7
-0.0659	0.9341	1588	+105	+29.7

Water 20°C →

The reference medium of water at 20°C, shown highlighted in the table, has a index of n = 1 and therefore a change of Δn = 0 and Δc = 0. The speed of sound for the reference medium was taken as 1483 m/s as specified in section 2.5.1. The first row above the reference row is for Δn = 0.0165, which is predicted by the calculation to have ¼ of a fringe shift. The second row above the reference row is for 2 times this increment, or ½ a fringe shift. The third row above the reference is for ¾, and the top row for 1 full fringe shift. The rows below the reference row are for negative increments of 0.0165.

The last column of the table is a temperature value for distilled water that would give the specified speed of sound. This column is included for illustration purposes and is meant to give an indication of the sensitivity of the CAHM to temperature changes. For example, if the instrument was used to measure temperature variations in water, an observed fringe shift of ¼ wave would correspond to a temperature change of -7.1°C. Likewise, a fringe shift of -¼ wave would correspond to a temperature change of +8.5°C.

4.7 Simulated Fringe Shifts

For each of the specimen index (and speed of sound) values given in Table 5, a hologram was generated from the model shown in Figure 29. The goal was to compare these holograms to the reference hologram, which is the detected inference pattern without any specimen, and observe any fringe shifts. Figure 33 shows the results of these simulations overlaid.

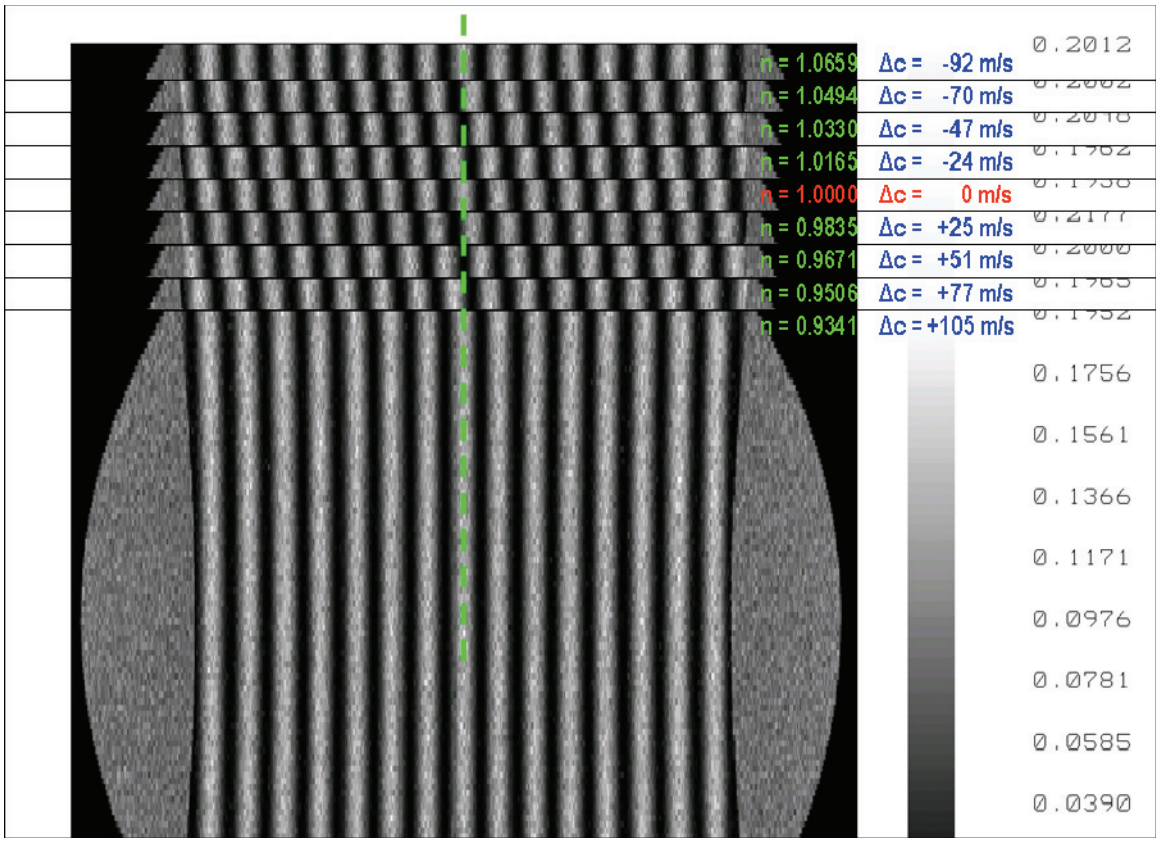

Figure 33: Simulated Holograms for Different Specimen Sound Speeds (overlaid)

The first detector image is for n = 1.0659, from the top row of Table 5. The next image, for n=1.0494, from the second row of Table 5, is laid on top of the previous image, and so on for each additional value of n in the table. We can clearly see that the fringes shift to the right as we decrease n. Also, we can see that the fringes have shifted exactly 1 fringe spacing from the n = 1.0659 hologram to the n = 1.0000 reference hologram. They shift another full fringe spacing going from n = 1.0000 to n = 0.9341, which is change of $\Delta n = -0.0659$. As predicted, the fringes shift exactly 1 spacing for a change of $\Delta n = 0.0659$.

This Zemax simulation did not use a collimated beam, but rather a convergent beam. However, the simulation results matched up perfectly with the calculations given by equation (53), which was done for the simple case. We can conclude that the calculation of Δn per fringe shift is indeed correct. Furthermore, we can conclude that for a decreasing index (increasing speed of sound) in the specimen, the fringes will shift to the right. Similarly, for an increasing index (decreasing speed of sound) in the specimen, the fringes will shift to the left. Hence, we can accurately determine the relative change in speed of sound as we scan through a specimen just by observing the shift in the fringes of the hologram. This variation in sound speed could be due to temperature changes or due to composition changes. If the

specimen was moved from the lower beam to the upper beam of Figure 29, then fringe shifts would have been in the opposite direction.

4.8 Other Possible Test Specimens

The following table shows the speed of sound and other relevant parameters for some liquids that could be used as specimens for testing the CAHM. The speed of sound values were obtained from [47].

Table 6: Speed of sounds for Possible Specimen

Δn	n	c_{sp} [m/s]	Δc [m/s]	specimen
0.3604	1.3604	1090	-393	Methanol
0.3123	1.3123	1130	-353	Ethanol
0.2674	1.2674	1170	-313	Isopropyl Alcohol
0.0262	1.0262	1445	-38	Olive Oil
0.0157	1.0157	1460	-23	Mineral (Paraffin) Oil
0	1	1483	0	Water (20°C)
-0.1478	0.8522	1740	+257	Motor Oil (SAE 20)
-0.2196	0.7804	1900	+417	Glycerine

The row for the reference medium, shown highlighted, is included for comparison. These liquids are already available in the lab, and a good test of the CAHM would be to use a specimen holder with two chambers with different liquids. By scanning from the first chamber to the second, we can observe the shift of the hologram fringes and compare it with the predicted shift using equation (53). For example, if we scanned between specimens of methanol and ethanol, which have an index difference of: $\Delta n = 1.3604 - 1.3123 = 0.0481$, we would expect a fringe-shift of $\frac{0.0481}{0.0659} = 0.73$ waves. The actual sound speed measurements of some the specimens in this table will be discussed in section 5.5.

4.9 Parallel vs Convergent beam for a Spherical Specimen

Up to this point, the specimen was always assumed to be larger than the beam diameter. However, it is possible to get useful information for even smaller specimens or small pieces within a specimen using a convergent beam, as discussed in section 2.2. Figure 34 shows the Zemax model using a spherical specimen of constant index.

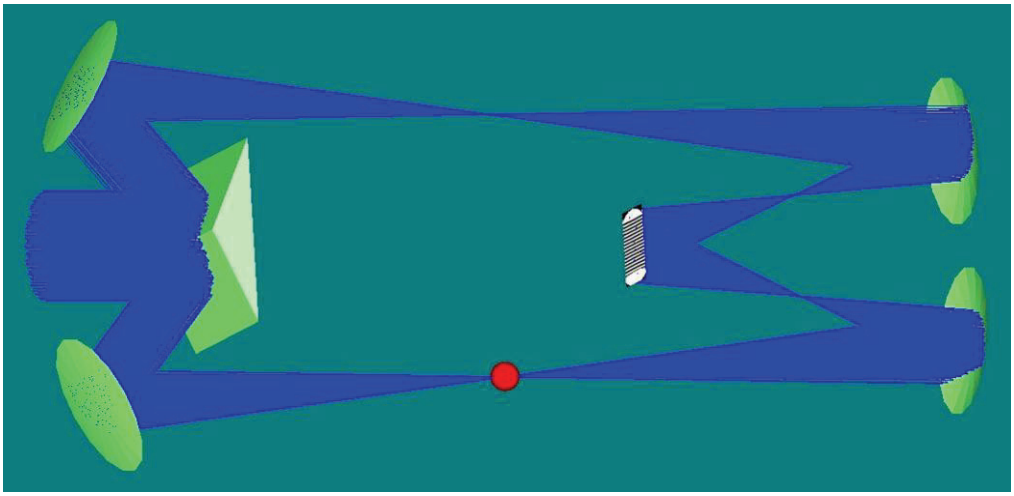

Figure 34: Zemax Layout with Spherical Specimen

The sphere is shown larger here for illustration purposes. If the sphere is made small, for example, 5 mm diameter, we can investigate the effect of the location of the specimen with respect to the focal point of the object beam. The next two figures show a change in position of the specimen and its effect on the hologram. Figure 35 shows the spherical specimen at the focal point of the object beam and Figure 36 shows the spherical specimen in front (to the left) of the focal point.

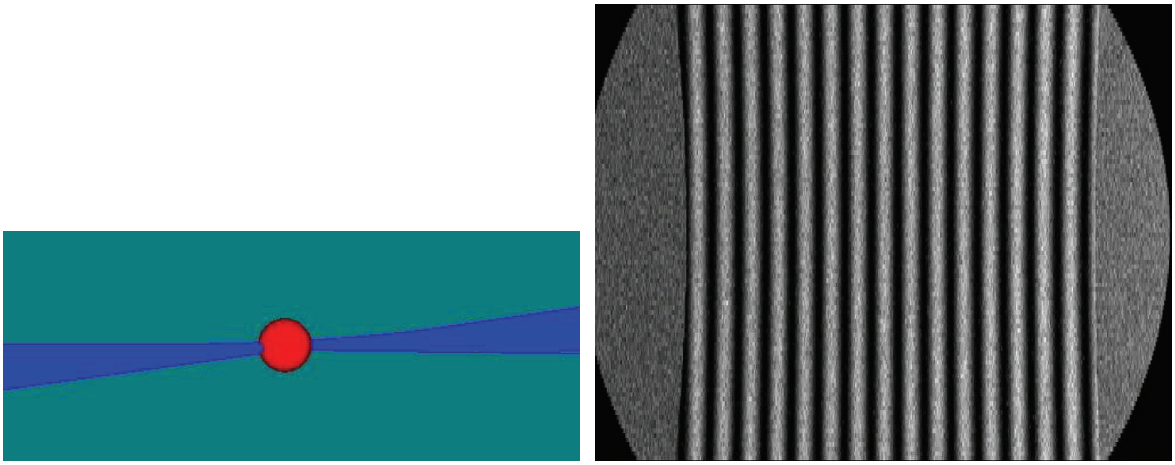

Figure 35: Hologram for Spherical Specimen at Focal Point

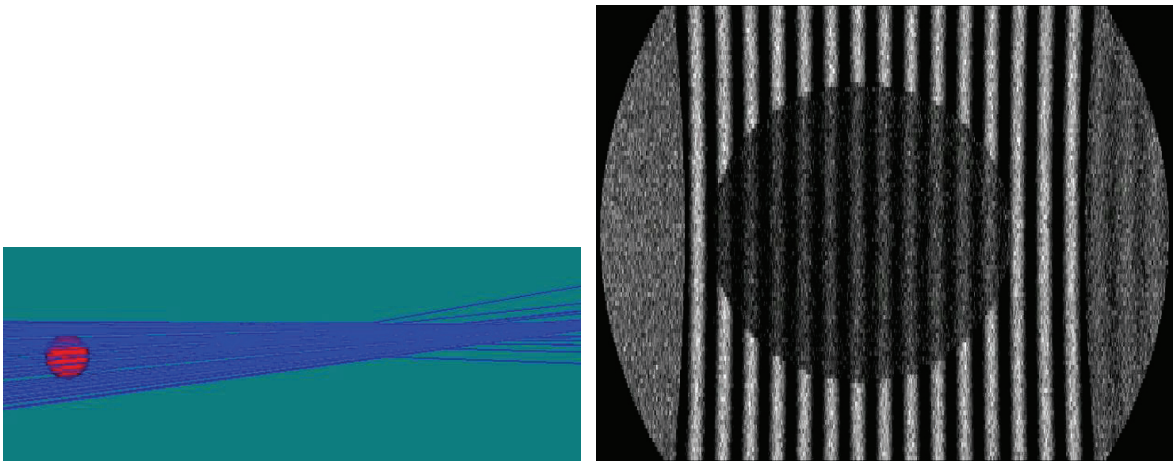

Figure 36: Hologram for Spherical Specimen in front of Focal Point

We can see that highest intensity fringes are in the same location for the two cases, but the second case has a big difference in contrast, where a "shadow" of the specimen can be seen. We can see that the rays that pass through the specimen are refracted in Figure 36 and their path is different than the rays of Figure 35, when the specimen is at the focal point. Hence, the contrast is poor in the shadow region of the hologram because fewer rays are getting to this area of the detector. Note that the fringes outside the shadow region will not change if the specimen index changes, because the rays that make up these fringes do not pass through the specimen. In other words, the high contrast fringes are due to the reference hologram and the low contrast fringes are due to the specimen. In practise, it is possible to subtract out the reference hologram data to enhance the contrast of the specimen fringes, as described in section 2.1.4. If the specimen index is changed, the interior specimen fringes (in the shadow region) will shift according to equation (53), while the exterior fringes will stay the same. Hence, it is possible to extract depth information about the specimen using the convergent beam and even some information about its size and shape. The same idea applies if the sphere shown above was a small volume element (*voxel*) within a larger specimen. In this case, a 2D array detector would be needed to capture the full hologram. Researchers at UVic are currently developing better algorithms to reconstruct the 3D specimen information from a series of measured 2D holograms.

4.10 Reflective Design

A reflective design of the CAHM was also considered, since it would be more practical for measuring specimens that are opaque to ultrasound frequencies. Figure 37 shows a simulated reflective design.

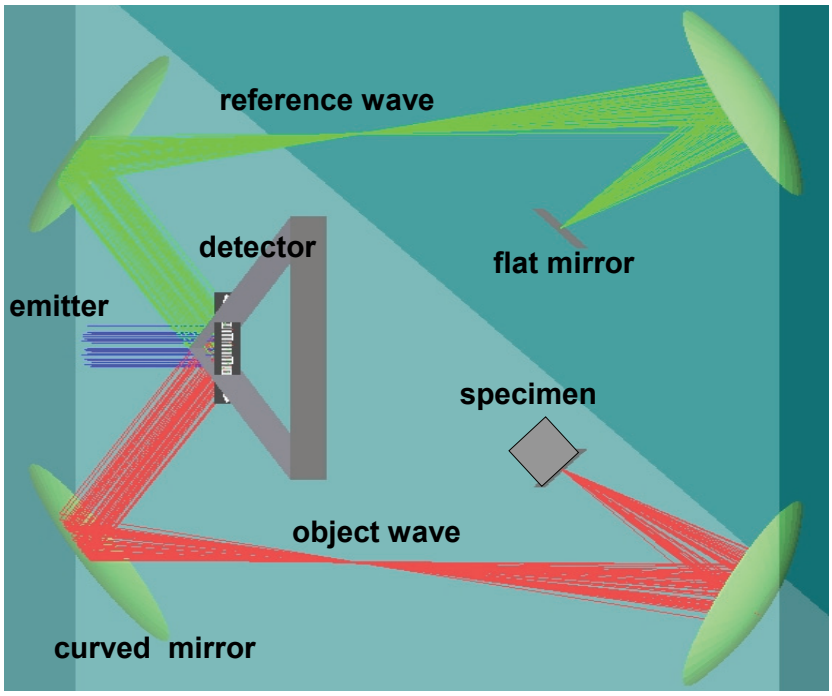

Figure 37: 3D Zemax Layout of CAHM Reflective Design

The sound beam gets split by the biprism, as before, but in this case the sound reflects off of the specimen and travels back to left side of the diagram. The reference beam reflects off of a flat mirror and also travels back to the left side. The two beams overlap inside the biprism, where the detector is positioned. The biprism would have to have an automated mechanical shutter that remains closed at first, but then opens to let the two interfering beams through. The phase information measured with this type of design will give useful information about the surface of the specimen and possibly about shallow internal interfaces. Reflective imaging is often used for non-destructive testing of mechanical components to find defects such as cracks.

The reflective version of the CAHM has only been theoretically proposed at this point. In the future, this design may prove to be very useful for medical imaging purposes, since ultrasound frequencies are scattered and attenuated very strongly by the human body. Therefore, it is easier to do reflective imaging in the body, rather than transmissive imaging. In the human body, most of the incident ultrasound will be reflected at interfaces with large differences of acoustic impedance, according to the Rayleigh equations (section 2.5.4).

The reflective design could also incorporate the fact that the phase of the reflected sound depends on the acoustic impedances at the interface, and incidence angle, as given in equation (18). Hence, the reflected phase measurement, along with knowledge of the

instrument geometry, could be used to reconstruct the acoustic impedances at the specimen interfaces.

4.11 Simplified Holography Setup

In absence of the ideal equipment to build the complete CAHM design, a simplified version was designed and built for testing purposes, as explained in section 5.7. The simulation of the simplified version is given in this section. Figure 38 shows a top view of the design.

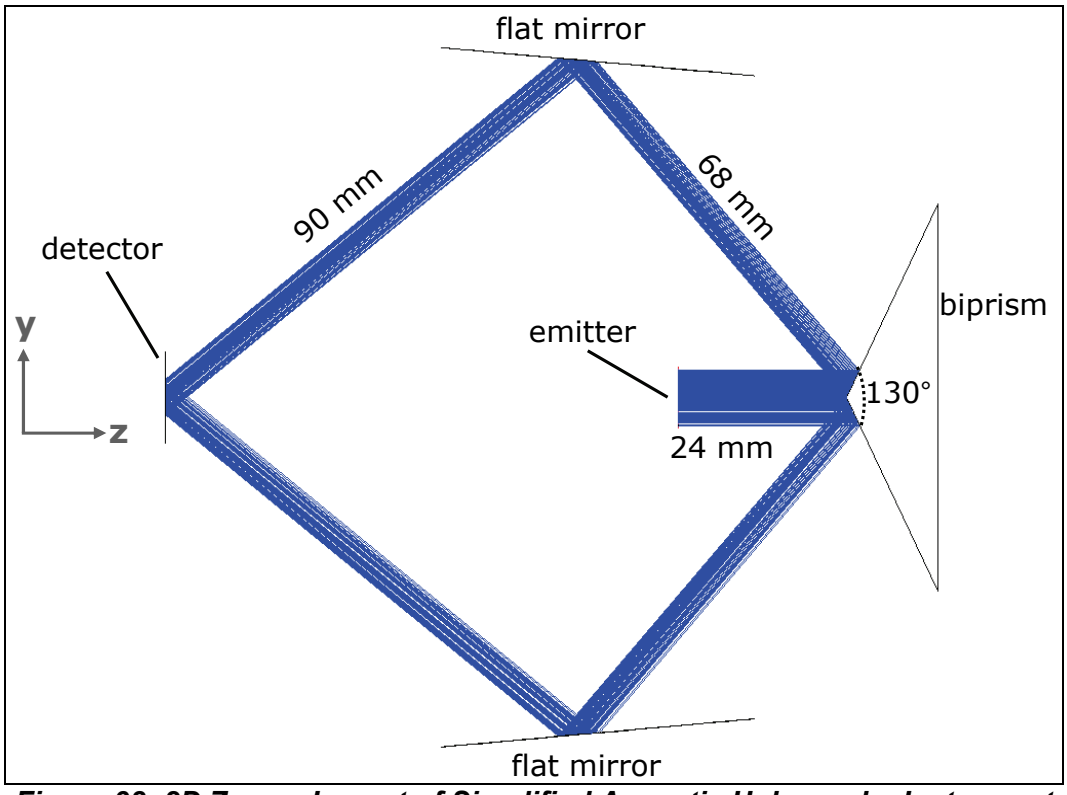

Figure 38: 2D Zemax Layout of Simplified Acoustic Holography Instrument

The emitted pulse is split by the same biprism as in the previous design. The 130° biprism is used because it allows the shortest path length between the biprism and the two flat mirrors The mirrors in this design are flat mirrors, rather than curved, since flat mirrors are already available in the lab. In the absence of a line array detector, a single element detector is used, which must be scanned horizontally (along the y-axis) across the hologram to build up the intensity information. The total beam path is 182 mm. Some of the positions of the parts needed to be determined experimentally and fed back into the Zemax simulation. This is because the experimental setup is restricted to the opto-mechanical equipment that was available in the lab. The dimensions shown above match the actual experimental setup used. The 3D shaded model shown in Figure 39 illustrates the simulated hologram at the detector on the left-hand-side.

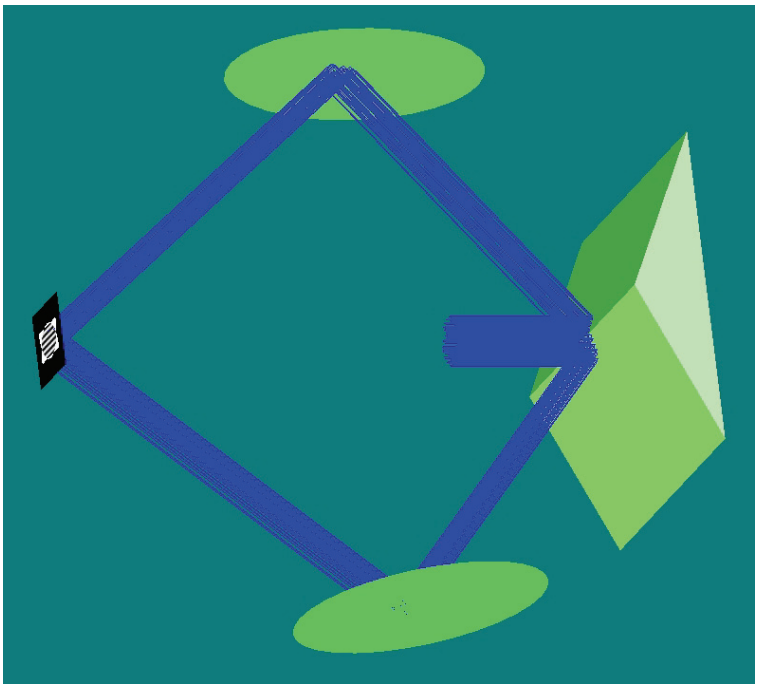

Figure 39: 3D Zemax Layout of Simplified Acoustic Holography Instrument

A larger view of the simulated hologram is shown in Figure 40.

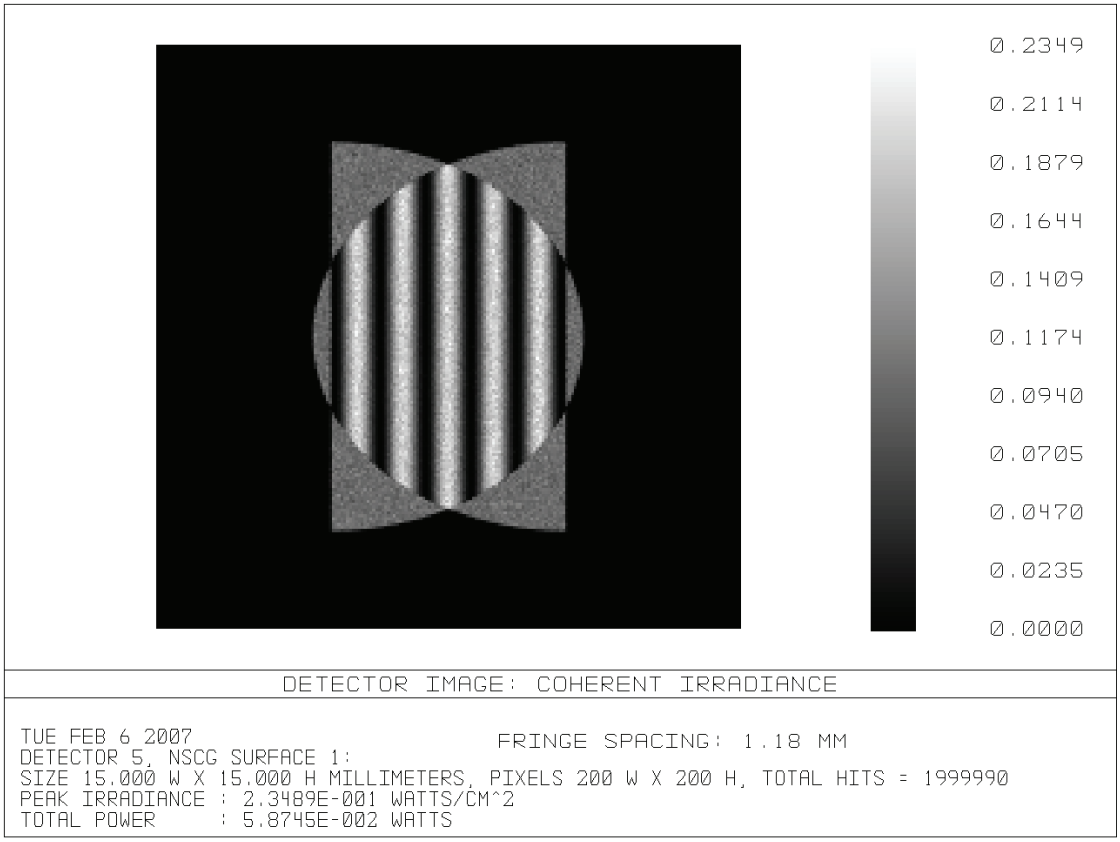

Figure 40: Simulated Hologram for Simplified Acoustic Holography Instrument

The fringe spacing for this simulation is 1.18 mm. This spacing will be compared to the experimental result of section 5.7. Since the two half-beams are made up of parallel (collimated) rays and there are no focal points, it does not matter where the specimen is placed, (recall Figure 9). An arbitrary position for a cube specimen was selected, as shown in Figure 41.

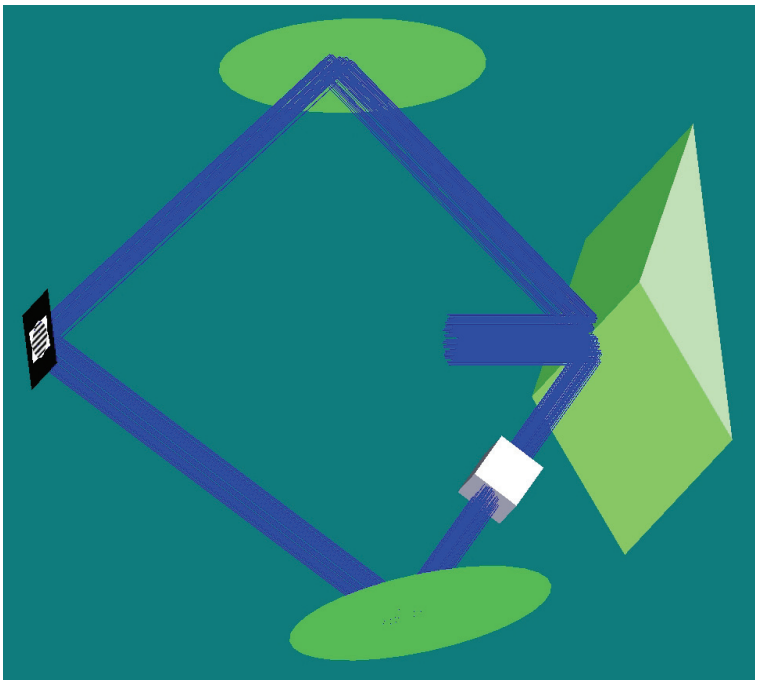

Figure 41: Simplified Acoustic Holography Instrument with Specimen

Some simulations were performed to observe the fringe shifts of some sample specimens using this configuration. These simulations yielded the same result as section 4.7, and therefore the results do not need to be repeated here. That is, the simulated fringe shifts matched up well with equation (53), regardless of whether a parallel or convergent beam is used to probe the specimen. The Zemax prescriptions and relevant parameters for these simulations are given in Appendix A.

5 EXPERIMENTAL RESULTS

In addition to designing the prototype CAHM, the goal of the current research was to use currently available equipment to design and construct a low cost proof-of-concept acoustic holography instrument. Using two transducers borrowed from Dr. Zielinski, some preliminary experiments were performed to characterize the transducers and test the types of signals that would be sent and received in the CAHM. Using the borrowed transducers and some signalling equipment, a simplified version of an acoustic holography device was constructed and tested. The knowledge obtained by doing these proof-of-concept experiments will aid in the future construction of the actual CAHM instrument.

5.1 Transducer Resonance

The two transducers (previously labelled "#1" and "#3" by the owner) were assumed to be approximately identical in construction, and were known to resonate at approximately 1 MHz. To test the resonance characteristics, a tuneable frequency generator was used to excite one of the emitters with a continuous sinusoidal signal. The output peak-to-peak voltage across the transducer was also measured with an oscilloscope, while varying the input frequency. A schematic diagram of the circuit is shown in Figure 42.

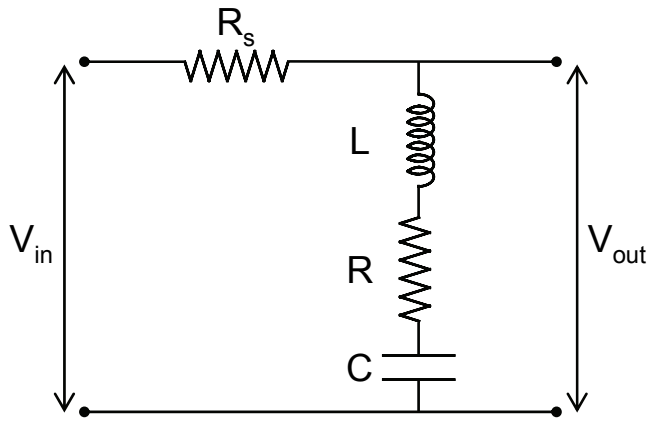

Figure 42: Circuit Diagram of Transducer Measurement

The transducer acts like a LRC circuit, with an inductance L, capacitance C, and resistance R. The signal generator has a source resistance, represented by R_s. The sinusoidal voltage, in the range of frequencies of 250 kHz - 5.3 MHz, was input into the circuit. Both the input and output voltages were measured and the results for transducer #1 are shown in Figure 43.

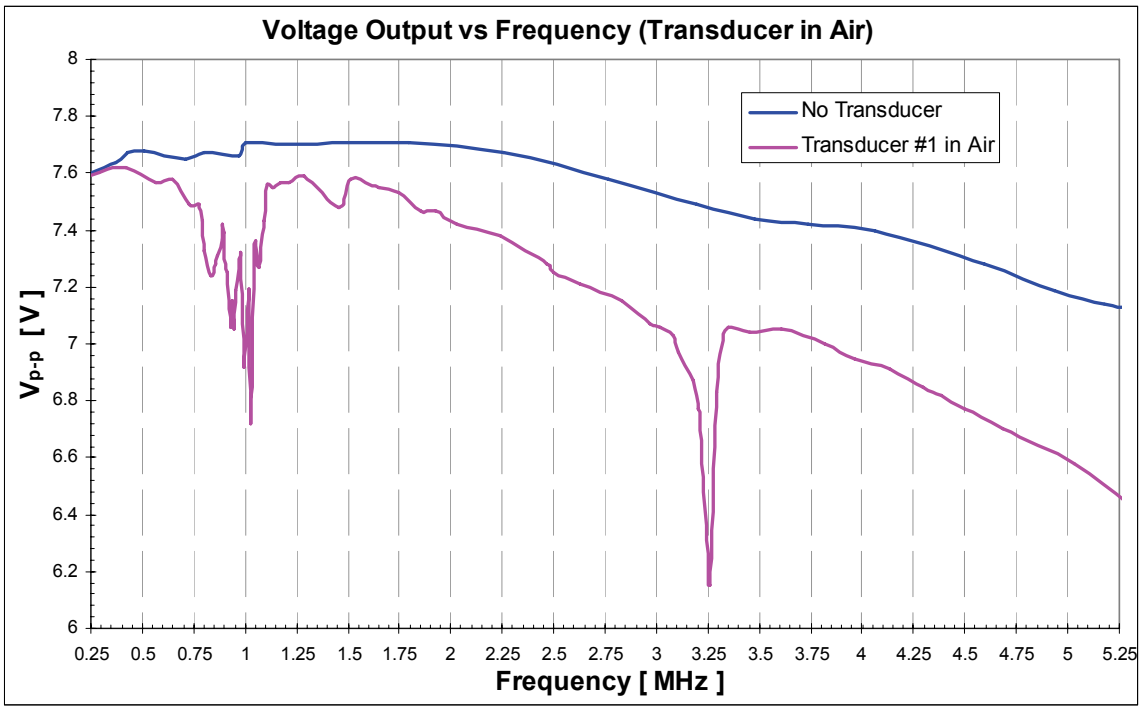

Figure 43: Resonance of Transducer #1 in Air

The input voltage is shown in the figure with the blue (darker) line. This line represents the case where there is no transducer connected to the circuit. We can see that the input voltage from the wave generator decreases slightly with increasing frequency, even without a load. The output voltage, when the transducer (ie. the load) is connected, is shown in pink (lighter colour). We can see that the output voltage also decreases with increasing frequency, but also there are large dips in voltage, at about 1 MHz and 3.25 MHz. These dips correspond to the resonance of the transducer, since the input energy goes into oscillating the piezoelectric disc, and therefore the output voltage drops as more energy is used up. Therefore, these two voltage drops represent the resonant frequencies of the transducer. The 1 MHz resonance was found to be the dominant one, and this frequency was used to transmit underwater sound in subsequent experiments, as described in the next sections. The same test was performed for transducer #3, and the results are shown in Figure 44.

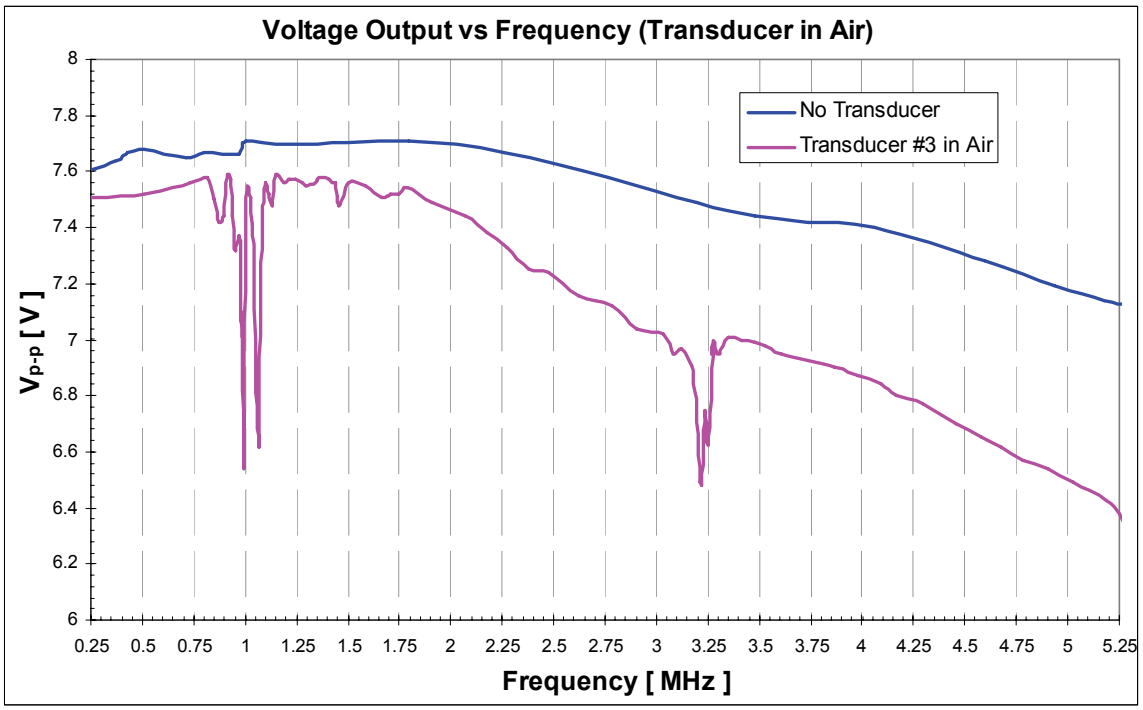

Figure 44: Resonance of Transducer #3 in Air

The resonances for this transducer match those of the previous transducer, with the most dominant resonance at 1 MHz. These tests were performed in air. Similar results were obtained in water, despite the change in the load of the circuit and different sound speed and attenuation. In water, the absolute voltage values were measured to be different than in air, but the resonant frequencies were found to be the same.

5.2 Simple Tests of Emitting and Detecting

A simple experiment was set up to send underwater signals between the two transducers, as shown in Figure 45. The emitter (transducer #3) is shown on the left and receiver (transducer #1) is shown on the right.

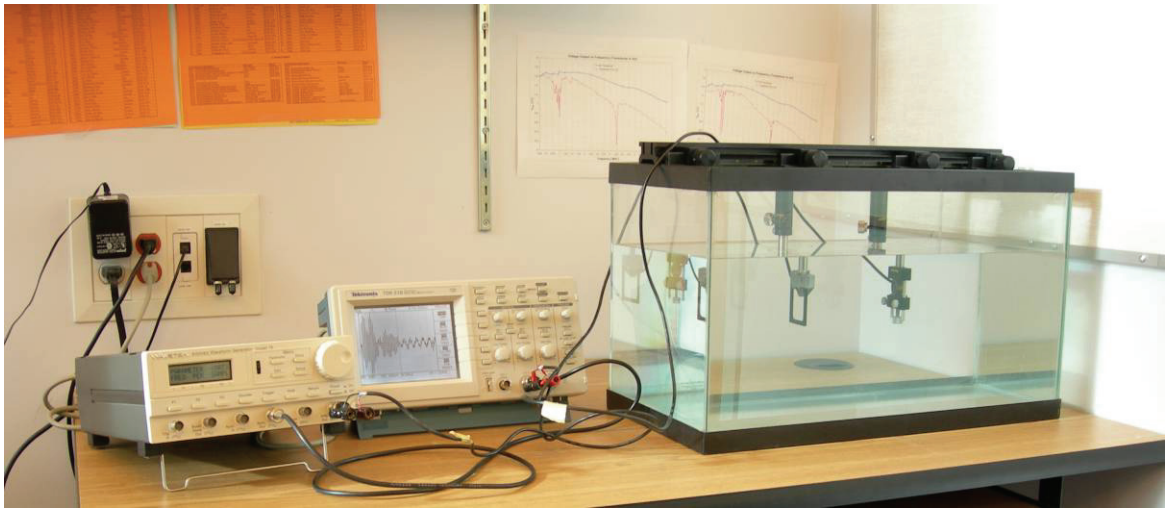

Figure 45: Experimental Setup for Preliminary Transducer Tests

The transducers were fixed to standard *Melles Griot* opto-mechanical positioning equipment and submerged in a tank of distilled water. The emitter was excited with a single negative impulse, 1 µs long, as shown in left side of Figure 46, using a *WaveTek* arbitrary waveform generator (model 75). The signal received by the other transducer is shown on the right side. The separation distance between the emitter and detector was 34 mm.

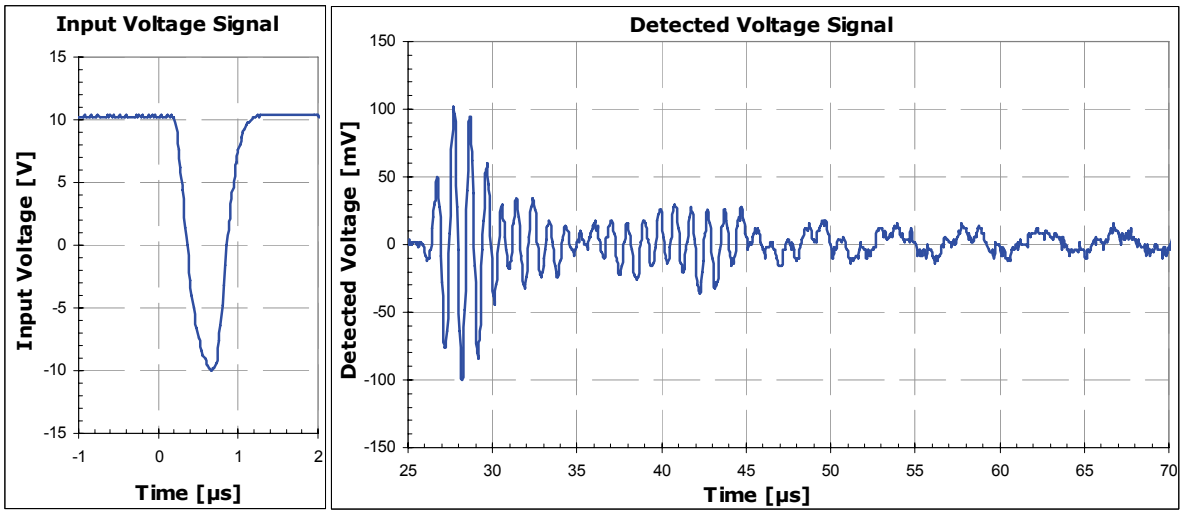

Figure 46: Transmitted Signal (Single Impulse) and Received Signal

An *Agilent Technologies* Digital Storage Oscilloscope (DSO 3062A) was used to measure the signal from the receiver and transmit it through a USB link to a computer. Even though the transmitted amplitude was 20.4 V, the received signal was in the mV range, (maximum peak-to-peak voltage 202 mV). The measured received signal shown above can be explained as follows: The single negative impulse excites the emitter and causes it to oscillate at its resonance frequency (1MHz) for about 10 or 11 cycles before dying down after about 10 µs. This sound pulse travels through the water, for approximately 25 µs, and then reaches the detector, where it excites an oscillation of the same frequency. This initial

pulse is shown on the graph between 25–35 µs. Another version of the pulse seems to show up at the receiver between 35-45 µs. It was thought that this second received pulse may be due a reflection from the water surface or bottom of the tank, but this possibility has been ruled out since the signal shape shown in Figure 46 remained the same, regardless of the depth and separation distance. The second pulse may be due to an internal reflection in the casing of the emitter, which would cause a smaller amplitude version of the original pulse to arrive a short time after the original pulse. After these two 1 MHz pulses are received, a lower frequency oscillation is also observed at the receiver beyond 45 µs, which continues for several hundred µs. This portion may be due to a resonance of the emitter and/or detector transducer at these lower frequencies, since it is likely not perfectly damped. Only the high amplitude, 1 MHz portion of the signal is of interest.

The frequency spectrum of the received signal in Figure 46 can be found by taking the Fourier Transform of the signal, which is shown in Figure 47.

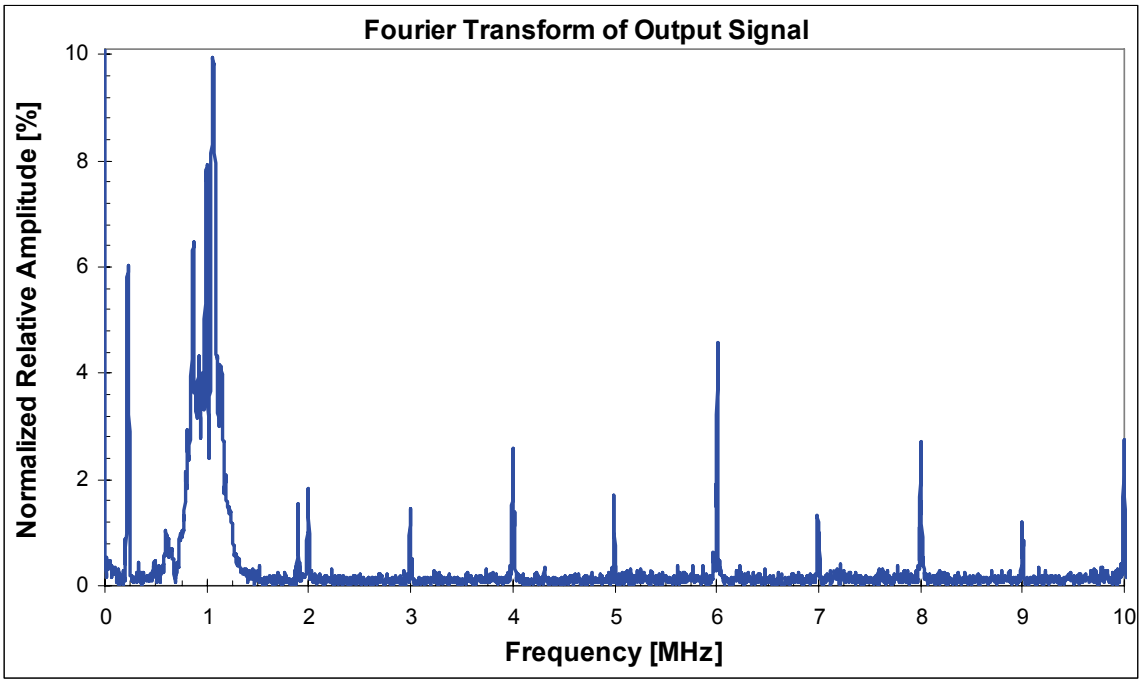

Figure 47: FT of Output Signal, for a Single Negative Impulse

The original data consisted of 4096 data points, with a sample period of 0.05 µs, or a sample frequency of 20 MHz. From the frequency spectrum, we can see a large peak in intensity at about 1 MHz, and also a lower low frequency peak at about 220 kHz. There are also peaks at 2, 3, 4, 5, 6, 7, 8, 9, 10 MHz. These are assumed to be harmonics of the original 1 MHz peak, or possibly some external high frequency noise. The vertical scale is normalized to the maximum value in Figure 52, as explained below.

The smallest pulse duration possible with the *WaveTek* AWG is 1 µs. The period of a 1 MHz oscillation also happens to be 1 µs. Therefore, in order to try and increase the energy output by the emitter, a chain of 1 µs impulses should be used. Using one of the AWG's options, called "*burst mode*", the number of impulses was varied from 1, 2, 3, etc. It was found that for small numbers of impulses (sent to the emitter), increasing the number of impulses increased the received amplitude at the detector, as expected. For example Figure 48 shows a chain of 7 negative impulses that was produced by the signal generator.

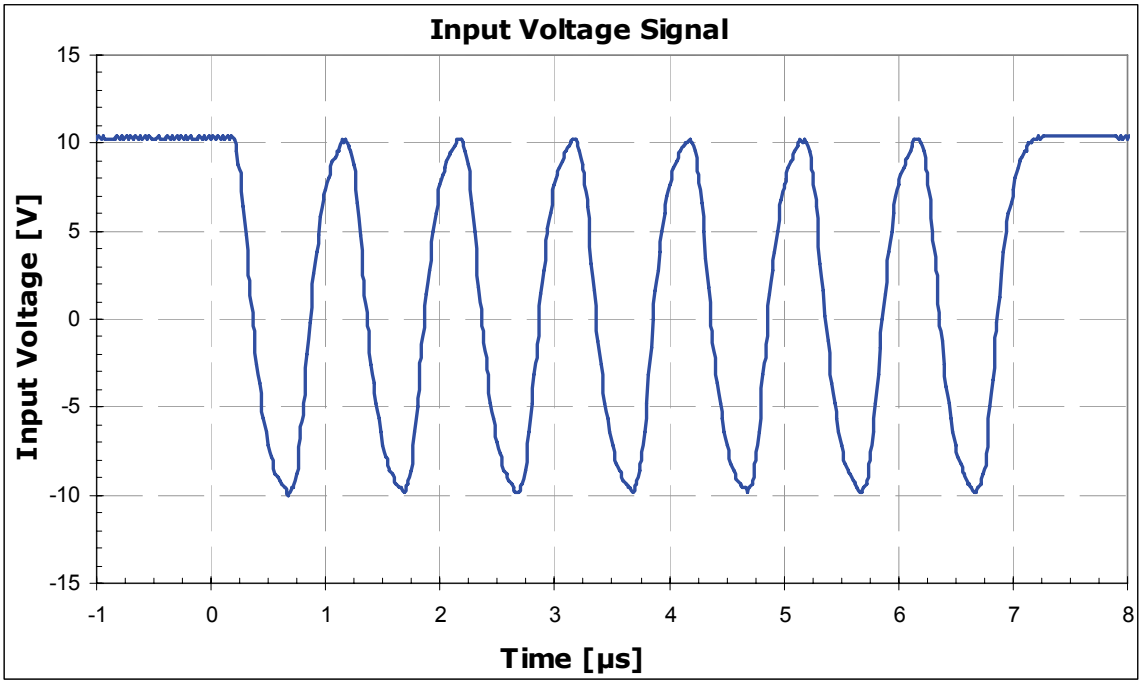

Figure 48: Transmitted Signal, 7 Negative Impulses

For the above input signal, used to excite the emitter, the resulting received signal at the detector is shown in Figure 49.

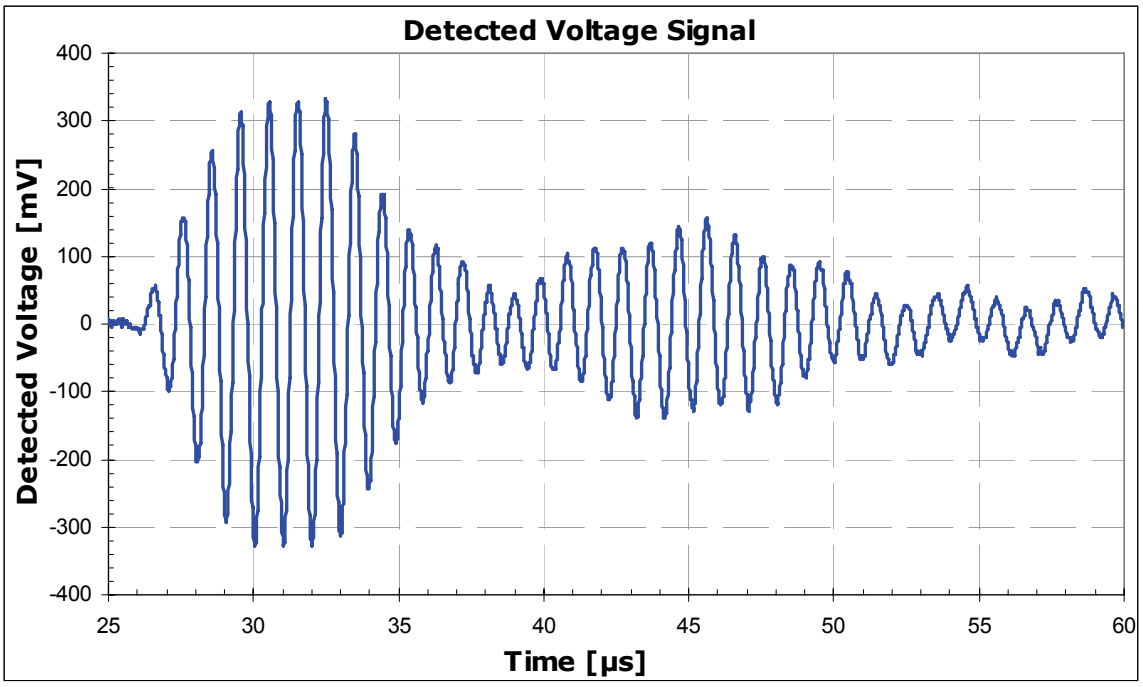

Figure 49: Received Signal, for 7 Negative Impulses

In this case, the output is much higher than for a single negative impulse (Figure 46). The maximum peak-to-peak value is 660 mV, compared to 202 mV for a single negative inpulse. Also, the pulse duration was increased slightly, since there are approximately 14 cycles in the initial pulse packet shown here. Increasing the number of impulses beyond 7 increased the pulse duration, but did not significantly increase the received amplitude. For example, using 13 negative impulses, the following received signal was measured:

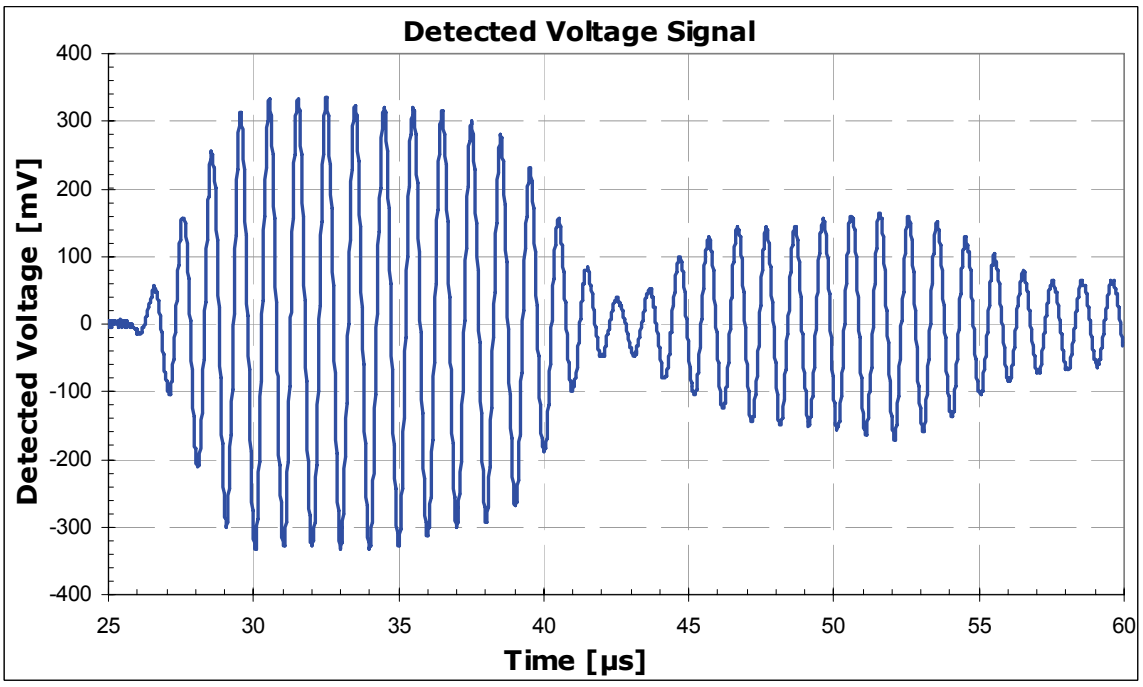

Figure 50: Received Signal, for 13 Negative Impulses

In this case, the received pulse is longer than before, approximately 18 cycles for the initial pulse packet. However, there is not a significant increase in the maximum peak-to-peak voltage, which is 668 mV. In general, increasing the number of impulses beyond 13 did not help with increasing the amplitude, but only increased the pulse duration. A large number of cycles of sound waves is not desired because it can increase the effects of unwanted reflections in the water tank. An optimal value of 13 impulses was chosen for the experiments in the following sections. The frequency spectrum for the "7 impulses" received signal (from Figure 49) is shown in Figure 51.

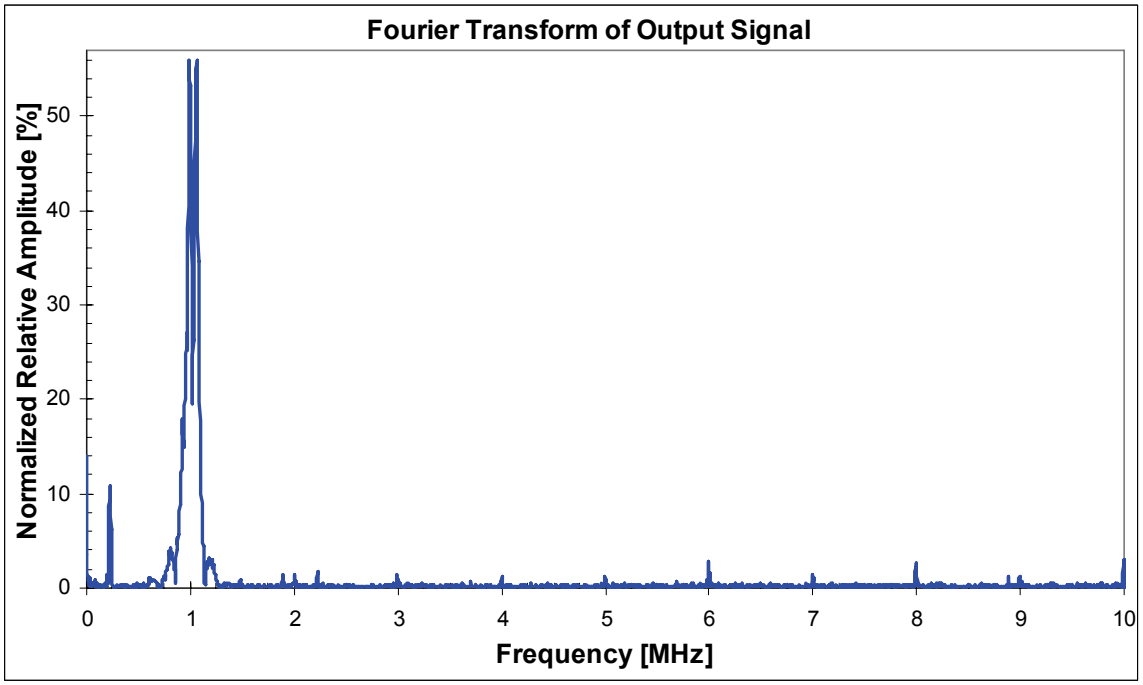

Figure 51: FT of Received Signal, for 7 Negative Impulses

The 1 MHz peak in this case is narrower than in the previous frequency spectrum (Figure 47). In other words, increasing the pulse length causes the bandwidth to decrease. Also, the lower frequency component (235 kHz) is much lower now, compared to the main 1 MHz peak. The higher frequency components have dropped to negligible levels. As we would like, more energy is going into the 1 MHz oscillation and less energy into the other frequencies. The vertical scale is normalized to the maximum value in Figure 52, as explained below. The Fourier spectrum of the "13 impulses" received signal (from Figure 50) is shown in the Figure 52.

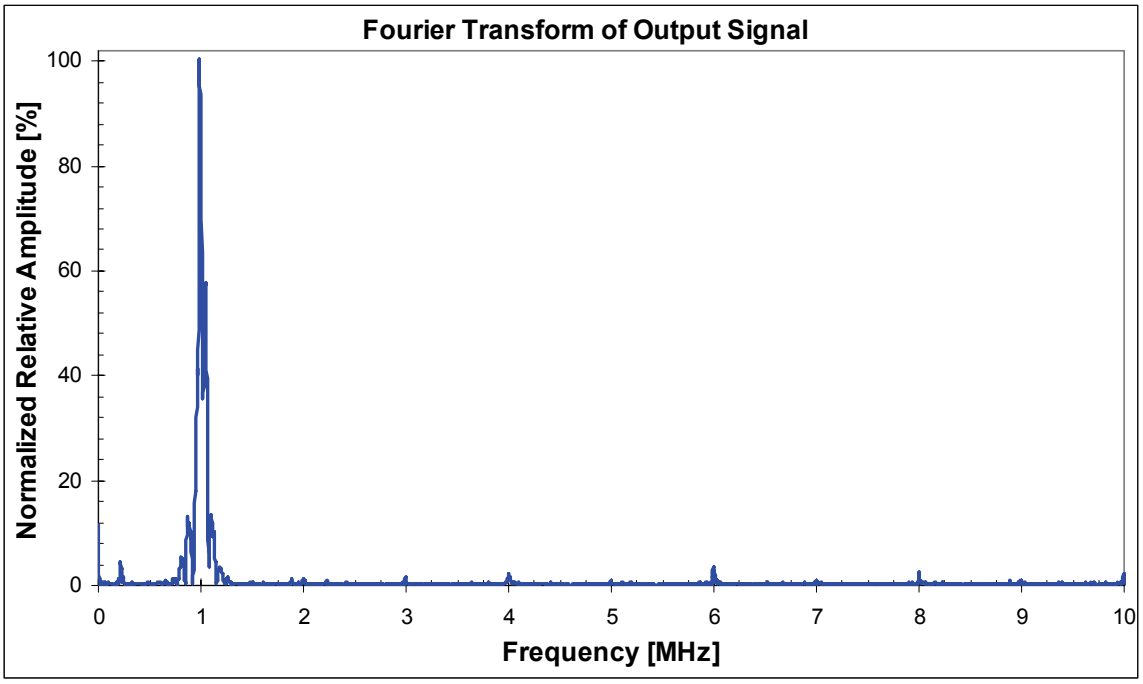

Figure 52: FT of Received Signal, for 13 Negative Impulses

In this case, the 1 MHz peak is even narrower than before, and all other unwanted frequencies are now negligible. This narrow bandwidth will be ideal for the holography measurements, where a constant narrow frequency is essential. The amplitude in this figure is normalized to the maximum at 1 MHz. Looking back at the previous two spectra, the maximum relative amplitude for Figure 47 was only 10% and the maximum for Figure 51 was only 50% of the maximum amplitude in Figure 52. An optimal value of 13 impulses was chosen for the experiments in the following sections. Note that a pulsed signal is desired in acoustic holography, since a continuous wave signal would lead to many unwanted reflections in the water tank, which would contaminate the observation of a hologram.

Other factors that affected the received transducer amplitudes included the transducer rotational orientations, the relative heights of the emitter and detector, the length of time the transducers were in water, and which transducer was used as the emitter/detector. Other unknown factors seemed to change the amplitudes from day to day or hour to hour. Also, the received amplitudes decreased over the course of the few months that they were used. This may be due to the build up of ionic deposits on the transducer surfaces and the wearing of the protective coating, which is meant to match the acoustic impedance of water. Although the water used was de-ionized, metals from the presence of the opto-mechanical equipment in the tank may have increased the ion concentration over time. The water in the tank was changed with fresh de-ionized water approximately once a week. Under ideal conditions, and when the separation distance was small, the maximum received amplitude

achieved using these transducers was about 1.2 V. In the future, amplification of the input signal may be required to achieve better results, especially for the holography experiments where the amplitudes are very low. For the duration of the experiments, transducer #3 was used as the emitter and transducer #1 was used as the detector.

5.3 Transmission Loss Measurement

Using the opto-mechanical positioners, accurate translations of the transducers were possible, down to a minimum step size of 1 µm. By varying the separation between the transducers and recording the maximum peak-to-peak received voltage, the following graph was produced.

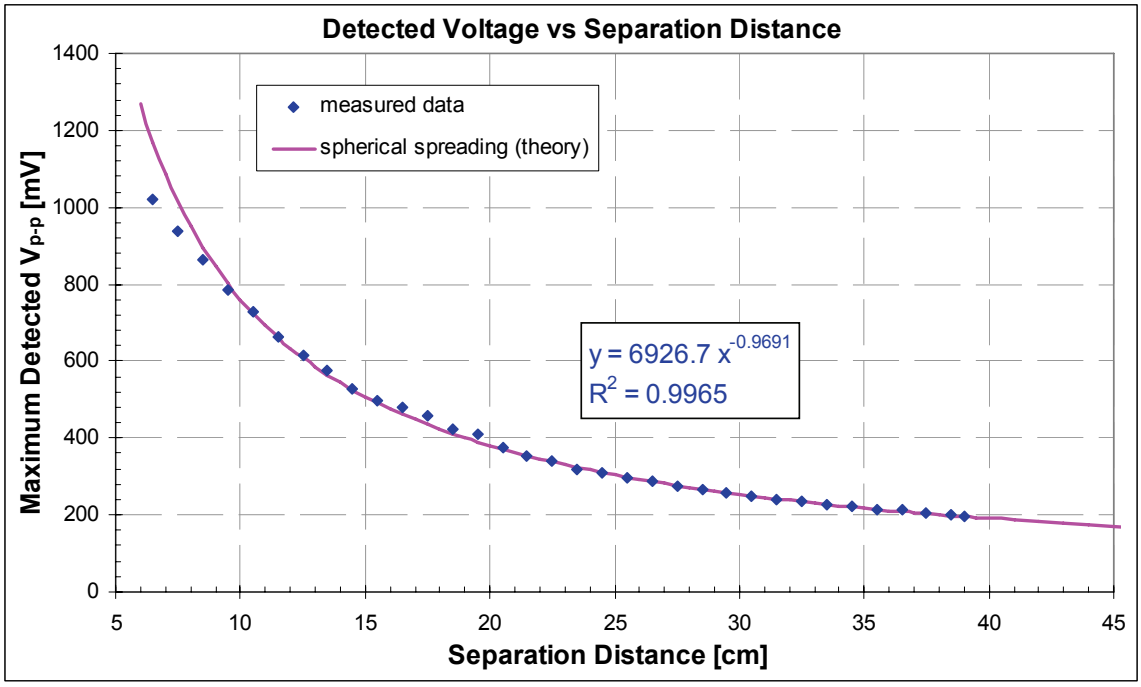

Figure 53: Detected Peak-to-Peak Voltage vs Emitter-Detector Separation

The measured intensity at the detector (blue line) appears to drop with distance, as expected from the spherical spreading theory of equation (21). The pink line shows the theoretical pressure/voltage drop from equation (21), which matches up with the measured data very well. The least squares fit of the measured data to a "power" equation is shown in the figure. The exponent in this equation is very close to -1. Absorption effects can be ignored in this case, since the absorption coefficient at this frequency, calculated with equation (26), is only: $\alpha_{dB} = 0.22 \frac{dB}{m}$. Either the theoretical equation or the least squares equation can be used to predict the detected voltage, y, at an arbitrary distance simply by inputting the distance value, x, in cm. This result is useful to apply to the holography designs, since the beam path distance for these transducers should be chosen to provide

sufficient signal intensity. For the holography experiments, we also need to take into account that the beam is split in two, which would cut the pressure/voltage in half, in addition to the spherical spreading loss. The lowest signal that can be reliably detected with this experimental setup is around 20 mV. Signals lower than this become washed out with noise. In the future, an automated system would be desirable, which could take many measurements and average them to improve the signal-to-noise.

5.4 Speed of Sound Measurement

In Figure 50 and the previous figures of received signals, the 25 μs delay of the signal was due to the transit time of the sound through the water. The received signal will shift to the right as the separation distance increases, since the time for the signal to travel through the water increases. This shift or time delay can be used to measure the speed of sound in water. In Figure 54, the transducer separation is plotted vs. the time delay of the signal.

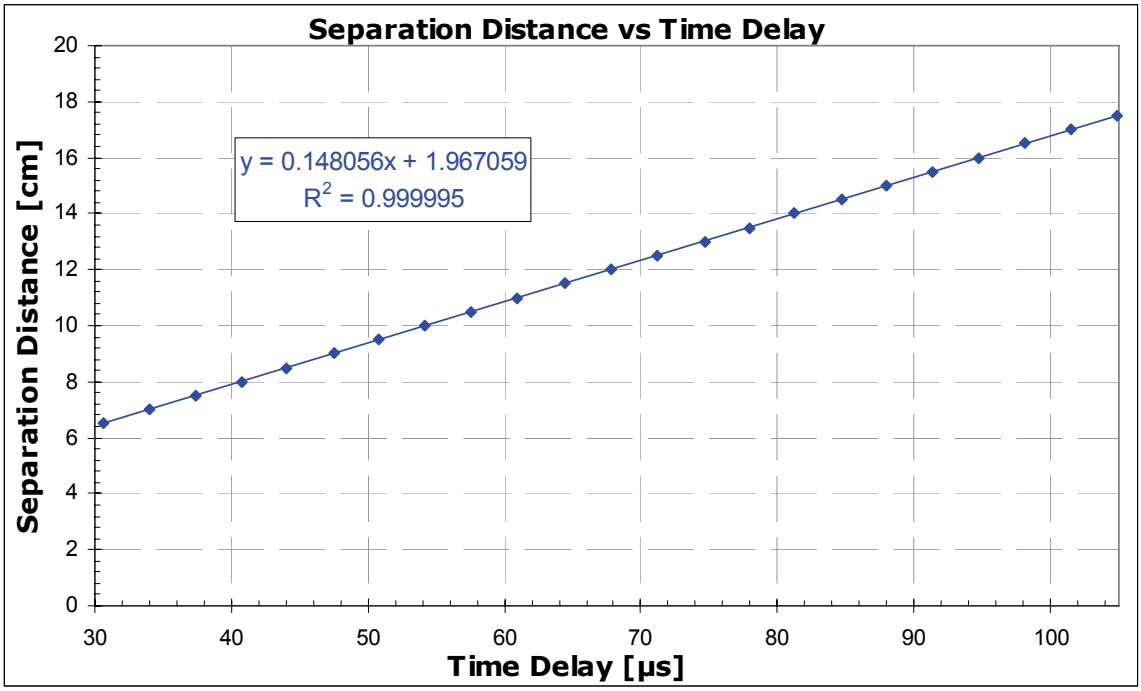

Figure 54: Separation Distance vs the Relative Time Delay of Received Pulse

As expected the separation distance varies linearly with the time for the sound to travel. From the slope of the line, the speed of sound was measured to be c = 1480.6 m/s. The temperature was measured with a mercury thermometer to be 19.8°C. For this temperature, the speed of sound calculated using equation (6) is 1482.2 m/s. This gives a difference of only 0.1% between the theoretical and calculated speed of sound. Hence, for the experiments in the following sections, we can simply measure the temperature of the water to determine the speed of sound, and we can be confident in the accuracy of equation (6).

5.5 Speed of Sound Measurements of Cuvette Specimens

There are two methods used in this investigation to measure the speed of sound in a liquid specimen, both of them using a phase shift measurement. The first method measures the phase shift of the sound pulse travelling through a specimen by observing the time delay of the signal, (described in this section, 5.5). The second method measures the phase shift by observing the spatial hologram, (described in section 5.7). For the first method, measurements of the speed of sound of various liquid specimens were performed using a set of polypropylene cuvettes. The cuvettes are manufactured to be identical, with an internal thickness of 10 mm, and a wall thickness of 1.2 mm. For a particular liquid specimen, a cuvette was filled and sealed, and then positioned in the water tank between the emitter and detector transducers, as shown in Figure 55.

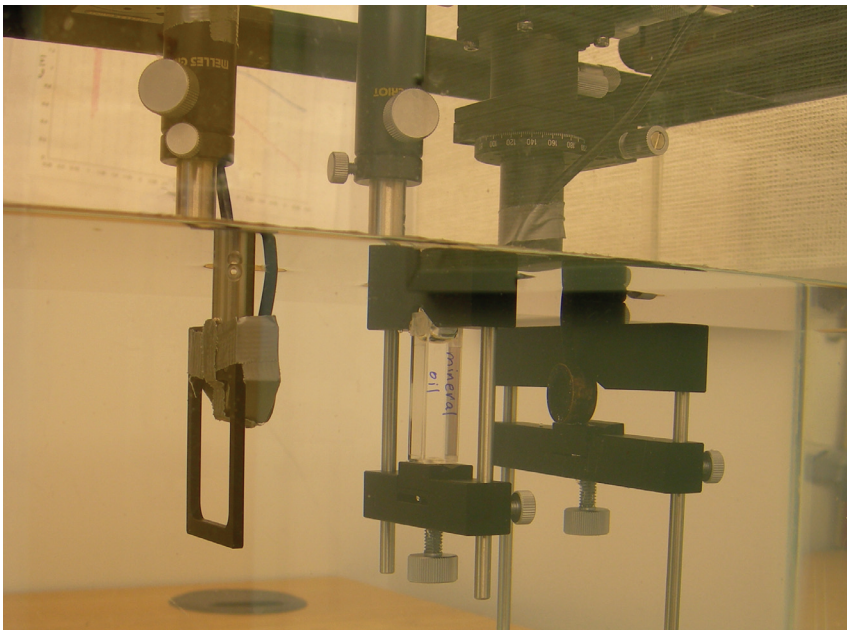

Figure 55: Setup for Measurement of Cuvette Specimens

The figure shows a transparent cuvette, labelled "mineral oil", between the emitter and detector. The transducer separation distance was 100 mm. For an input pulse of 13 impulses, the received pulse was measured in the absence of any specimen. Next, a cuvette specimen of water was measured. Figure 56 shows the received pulse for the two cases.

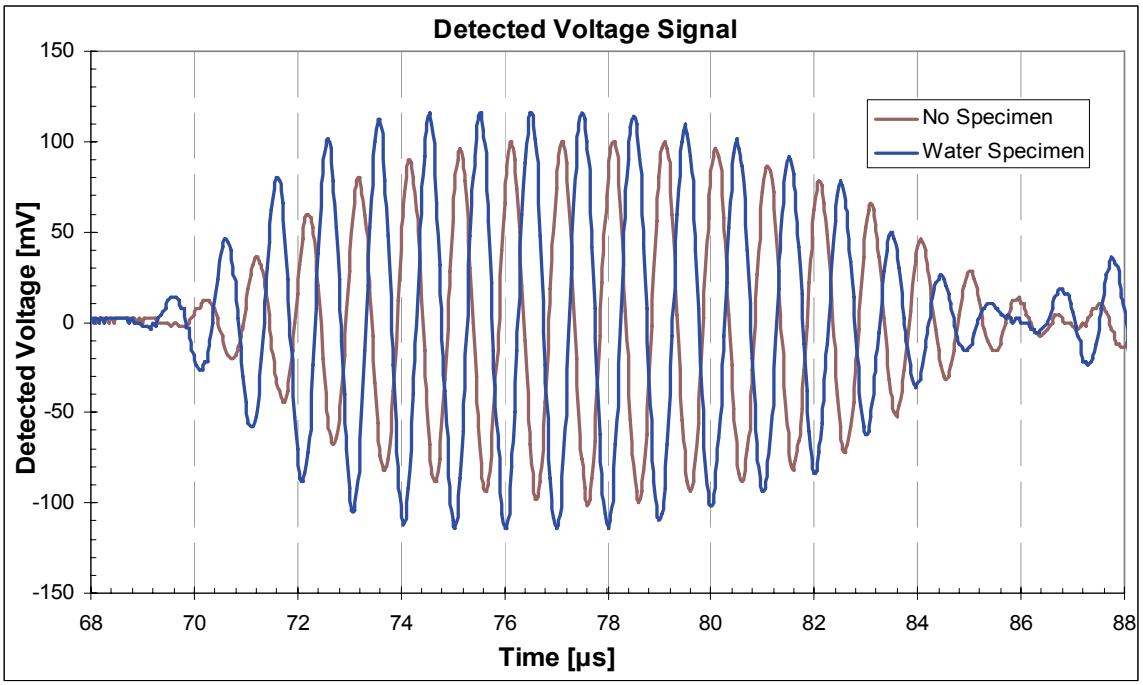

Figure 56: Received Signals, No Specimen and Water Specimen

The brown (lighter) line shows the case where there is no specimen (ie. only water, no cuvette) present between the transducers. The blue (darker) line shows the case where the cuvette specimen is filled with water. For the water specimen, no lid is used to seal the cuvette, so the water inside the cuvette is connected to the water in the rest of the tank. The only difference between the two cases is the presence of the polypropylene cuvette. As we would expect, there is a slight phase shift (or time shift) of this signal for the water specimen because the sound pulse has to travel through a small amount of polypropylene. There is only a slight drop in intensity with the cuvette present, which means that the material chosen is appropriate to test other liquid specimens, since the reflection and absorption of sound due to the cuvette are minimal. This is due to the fact that the acoustic impedance of polypropylene, 2.24 MRayl, is pretty close to that of water, 1.5 MRayls [47].

The signal for the water specimen shown above arrives slightly before the "no specimen" case. This is expected since the speed of sound in the cuvette walls (2.4 mm total thickness) is greater than the equivalent thickness of water. The blue signal above is time-shifted by Δt = -0.6 µs. Using this time shift, a calculation was performed to measure the speed of sound in the polypropylene cuvette. A similar calculation is shown below for the other specimens tested. The speed of sound in the polypropylene was calculated to be 2380 m/s, which has a difference of 4.5% from the theoretical value of 2492 m/s for polypropylene [47]. This test was not essential, but it helped confirm that the cuvettes were indeed made of polypropylene.

The following figures show the other specimens that were measured, and are compared to the reference case, (ie. the water specimen). Figure 57 shows the received signal for a specimen of ethanol, also known as ethyl alcohol.

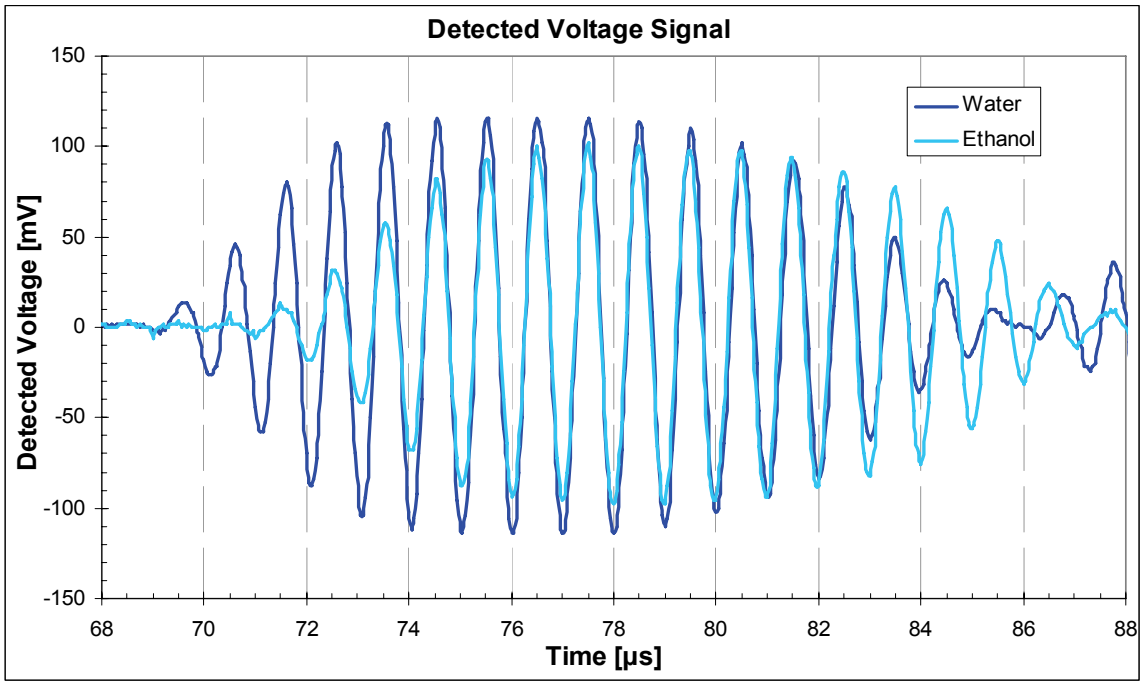

Figure 57: Received Signals, Water Specimen and Ethanol Specimen

The dark blue line is for the water specimen, and the light blue line is for the ethanol. The phase shift between the two cases can be measured via the time delay. Since the speed of sound in the ethanol is slower than water, the ethanol signal is delayed slightly, with a time shift of Δt = 1.97 µs. This value can be found "by eye", or more accurately using an autocorrelation algorithm (see section 5.7.3.3). Since the water and ethanol specimens were measured using an identical cuvette, the effect of the sound travelling through the polypropylene is cancelled.

The time delay can be used to determine the speed of sound in the specimen, as follows. The average water temperature for the duration of these experiments was 20.1°C. From equation (6), this gives a speed of sound in the water of: c_w = 1481.9 m/s. Both signals shown above travel through equal amounts of polypropylene, so the effect of the cuvette can be ignored. The time for sound to travel through 10 mm of water is: $t_w = \frac{d}{c_w} = \frac{10\ mm}{1481.9\ \frac{m}{s}} = 6.748\ \ \mu s$. The time for the sound to travel through 10 mm of ethanol is $t_{sp} = \frac{d}{c_{sp}}$. The time difference (signal shift) is: $\Delta t = t_{sp} - t_w$, and the travel time through the

specimen is $t_{sp} = 1.97\ \mu s + 6.748\ \mu s = 8.718\ \mu s$. Therefore, the speed of sound in the ethanol can be calculated as: $c_{sp} = \frac{d}{t_{sp}} = \frac{10\ mm}{8.718\ \mu s} = 1147\ \frac{m}{s}$. This value is within 1.5% of the theoretical speed of sound, which is 1130 m/s [47]. The ethanol used in this experiment was *Caledon* 1500-1 Denatured CH_3CH_2OH. The resulting speed of sound measurements for all the specimens are compiled below in Table 7. Figure 58 shows the received signal for a specimen of isopropanol, also known as isopropyl alcohol.

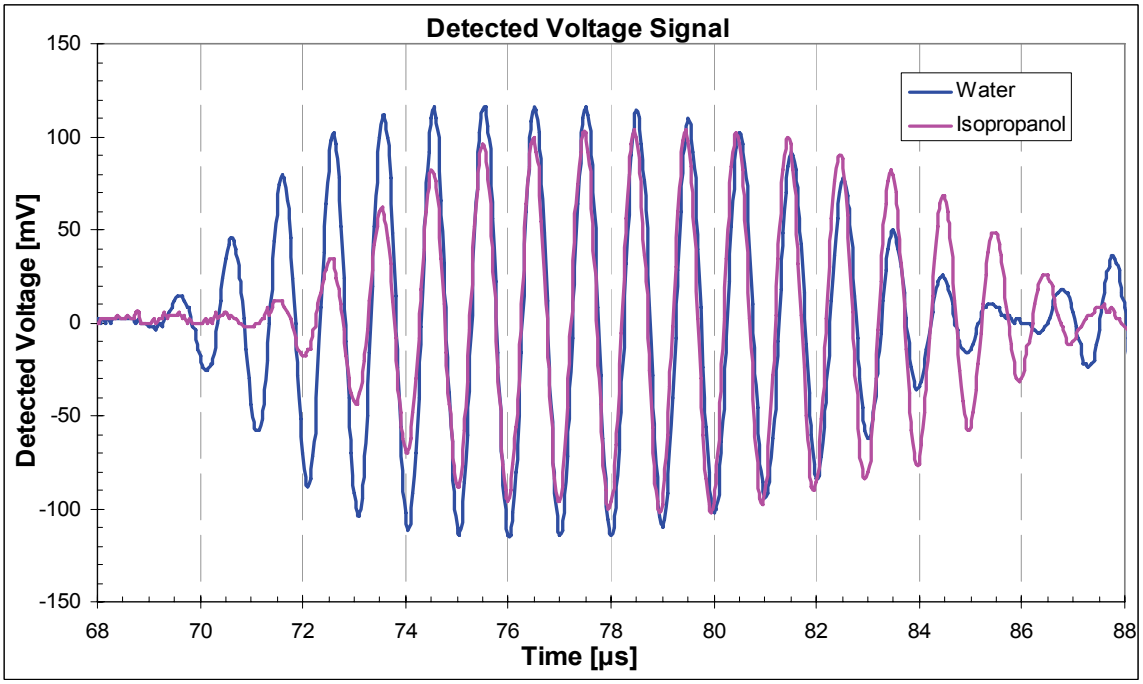

Figure 58: Received Signals, Water Specimen and Isopropanol Specimen

The speed of sound in the isopropanol is slower than in water, so the isopropanol signal is delayed slightly, by approximately 1.93 µs. The resulting speed of sound was calculated to be 1153.1 m/s. *Rougier* 99% Isopropanol USP was used in this experiment. Figure 59 shows the received signal for a specimen of mineral oil, also known as paraffin oil.

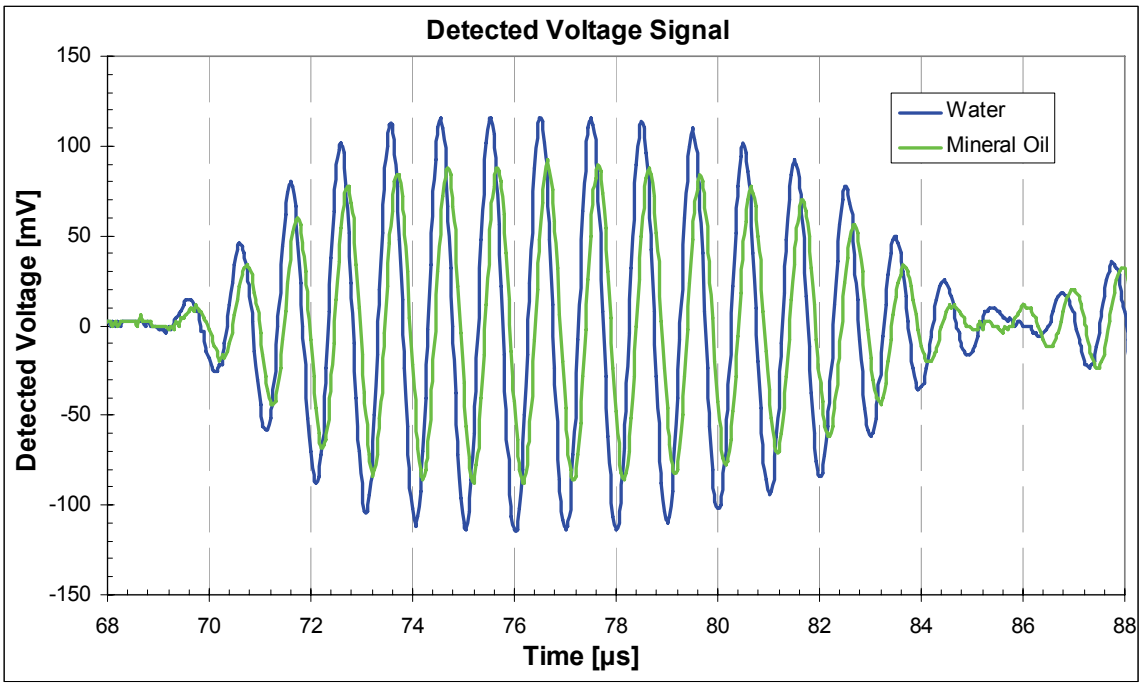

Figure 59: Received Signals, Water Specimen and Mineral Oil Specimen

The speed of sound in the mineral oil is slower than in water, so the mineral oil signal is delayed slightly, by approximately 0.15 µs. Using the method above, the resulting speed of sound was calculated to be 1450.9 m/s. *Rougier* 100% heavy mineral oil USP was used in this part of the experiment. Figure 60 shows the received signal for a specimen of vinegar.

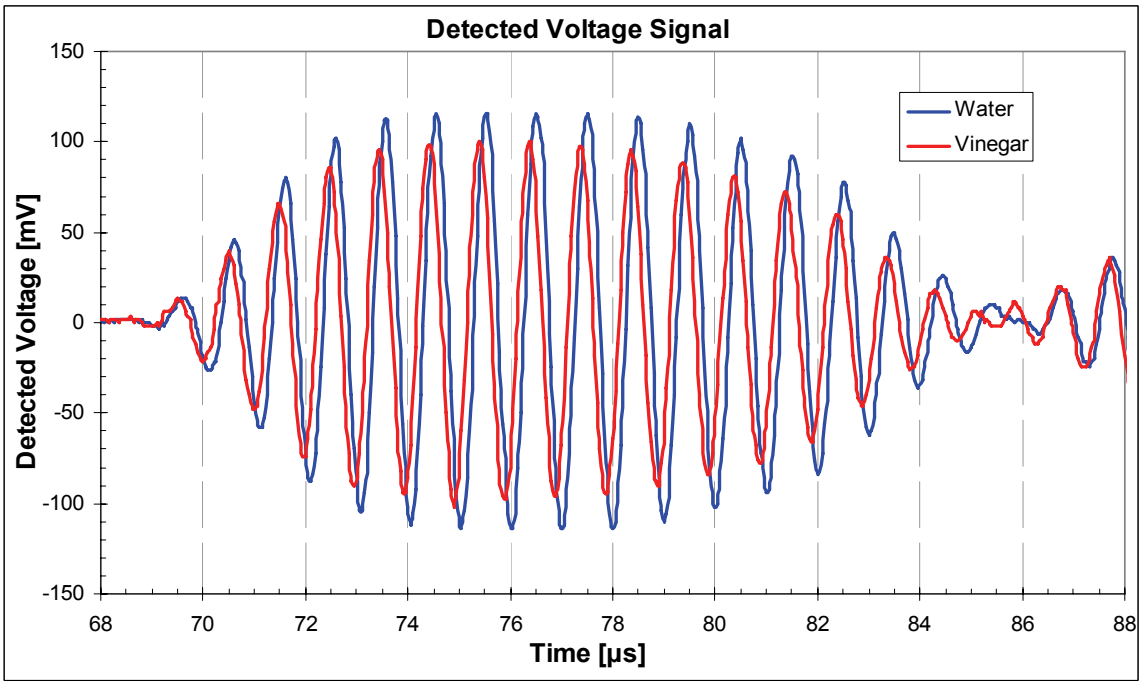

Figure 60: Received Signals, Water Specimen and Vinegar Specimen

The speed of sound in the vinegar is slightly faster than in water, so the vinegar signal arrives slightly sooner in time, by approximately 0.14 µs. The resulting speed of sound was calculated to be 1513.9 m/s. Allen's pure white vinegar (5% acetic acid solution) was used in this part of the experiment. Figure 61 shows the received signal for a specimen of glycerine.

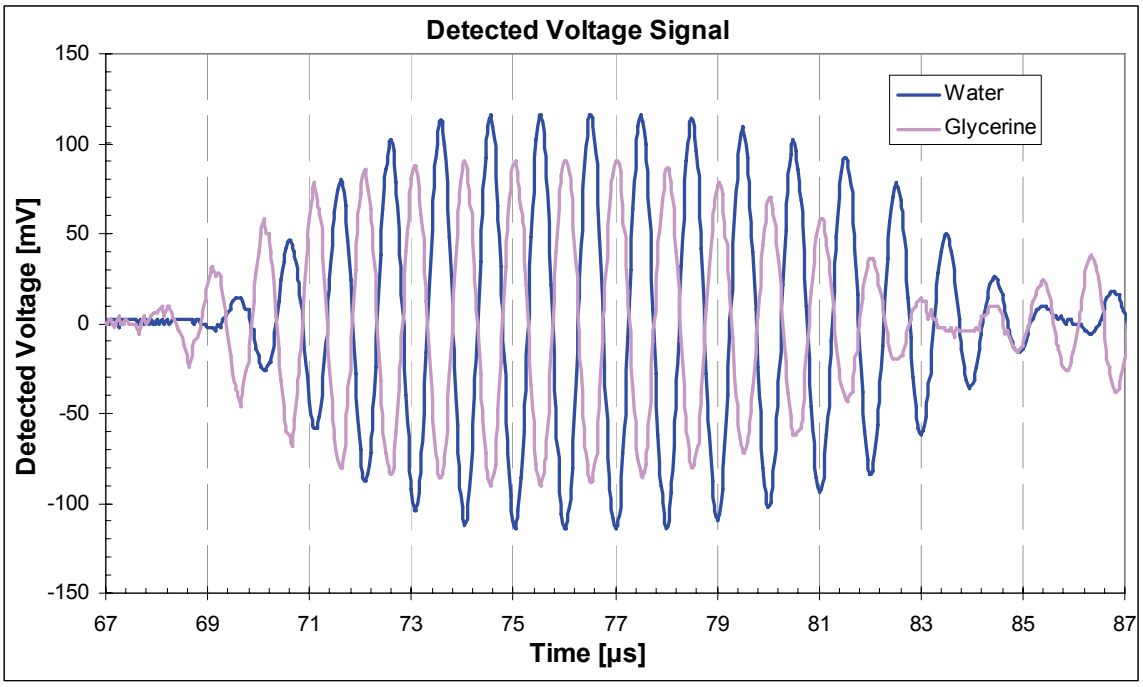

Figure 61: Received Signals, Water Specimen and Glycerine Specimen

The speed of sound in the glycerine is much faster than in water, so the glycerine signal arrives much sooner in time, by approximately 1.48 µs. The resulting speed of sound was calculated to be 1900.3 m/s. *Rougier* 100% Glycerine USP was used for this part of the experiment.

The following table summarizes the results of the speed of sound measurements. The time shifts were measured using an autocorrelation algorithm (see section 5.7.3.3).

Table 7: Measured and Theoretical Speed of sounds of Tested Specimens

tested specimen	time shift, Δt	measured speed	theoretical speed	difference
Ethanol	1.97 µs	1147.8 m/s	1130 m/s [47]	1.6 %
Isopropanol	1.93 µs	1153.1 m/s	1170 m/s [47]	-1.4 %
Mineral Oil	0.15 µs	1450.9 m/s	1460 m/s [47]	-0.6 %
Water (20.1°C)	-	-	1482 m/s	-
Vinegar	-0.14 µs	1514.6 m/s	1528 m/s [51]	-0.9 %
Glycerine	-1.48 µs	1900.3 m/s	1900 m/s [47]	0.1 %

Water at 20.1°C, which was the average temperature for the duration of these experiments, is included in table for comparison. All measured values for the specimens tested match up

very well with the theoretical speed of sound values in the literature. However, the theoretical values may not account for solution concentrations, impurities, and temperature variations. Hence, the measured speeds will be taken as the true values, and will be used for the holography experiments in sections 5.7.2 and 5.7.3.

5.6 Test of Transducer Spatial Sensitivity

Both transducers have an active area on the front surface with a diameter of approximately 1 cm. By scanning the detector transducer horizontally, across the beam axis of the emitter transducer, and measuring the maximum peak-peak voltage, the following beam profile was measured.

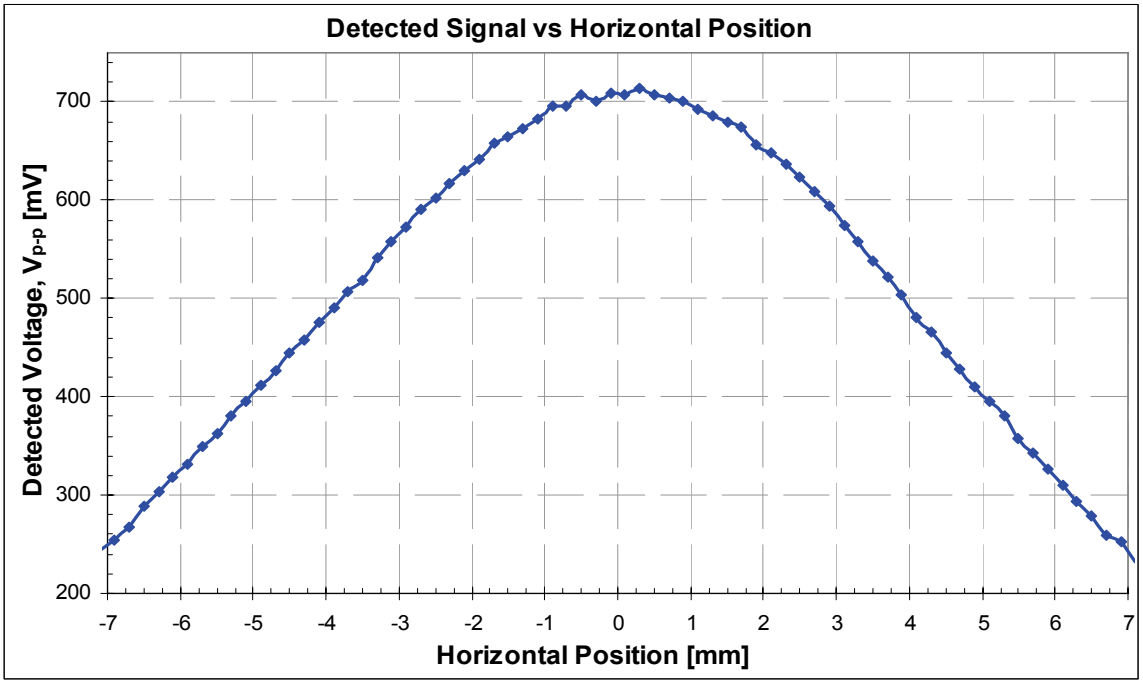

Figure 62: Detector Response to Horizontal Scan

The separation distance between the emitter and detector was 34 mm for this experiment. The maximum intensity occurs at a position of approximately 0 mm, which is along the beam axis of the emitter and detector, (recall Figure 24). From equation (44), the nearfield distance of the transducer should be approximately: $N = \frac{(1cm)^2}{4 \cdot (1481.9 \mu m)} \approx 17 mm$. Therefore the above beam-profile was measured within the farfield. The beam-profile was found to be roughly the same shape for different separation distances, however the peak voltage drops according to spherical spreading, given in equation (21). Also, the results were similar, regardless of which transducer emits and which detects. Only a few beam-profiles were collected, since it is very time consuming to measure the output beam via manual scanning.

If we were able to do full 3D scan of the farfield of one of the transducers, we would expect the measurement to follow the theoretical radiation pattern of a piston transducer, which is shown in Figure 63, [52].

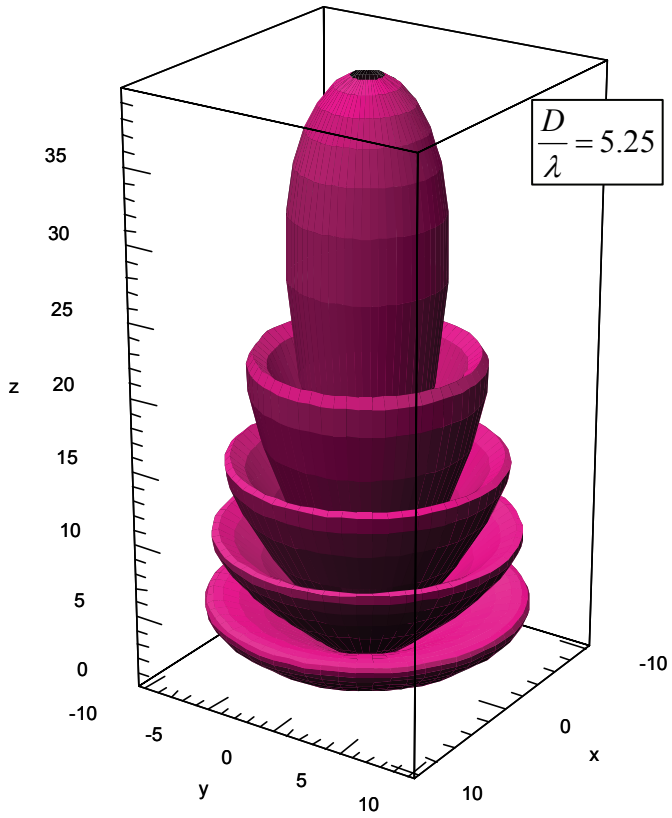

Figure 63: Theoretical 3D Radiation Pattern of a Piston Transducer

In this diagram, we can see that the intensity is greatest along the beam axis, and the intensity is cylindrically symmetric about this axis. The cigar shaped region with the highest intensity is called the main lobe. There are also 4 regions of lower intensity, called the side lobes. The exact intensities and number of lobes will depend on the diameter of the emitter and the wavelength of sound, or more specifically, on the ratio $\frac{D}{\lambda}$. This ratio is 5.25 for the piston transducer shown. For the transducer used in the experiment, it is $\frac{D}{\lambda} = \frac{1cm}{1482\,\mu m} = 6.75$, so its radiation pattern should be very similar to the one shown in Figure 63. Note that the intensity in the diagram (represented by the height) is scaled in decibels. When an automated version of the CAHM is eventually constructed, a similar 3D measurement of the emitter/detector radiation pattern will be possible and will be very useful for experimentation. The 1D scan shown previously in Figure 62 corresponds to the main lobe region of the piston transducer in Figure 63.

5.7 Holography Measurements

The holography method can measure the speed of sound of a specimen by detecting changes in the spatial hologram with respect to a reference hologram. A simple holography experiment was setup, as shown in the schematic simulation diagrams in section 4.11. A picture of the setup is shown in the Figure 64. A 30 cm (12") ruler is shown for comparison.

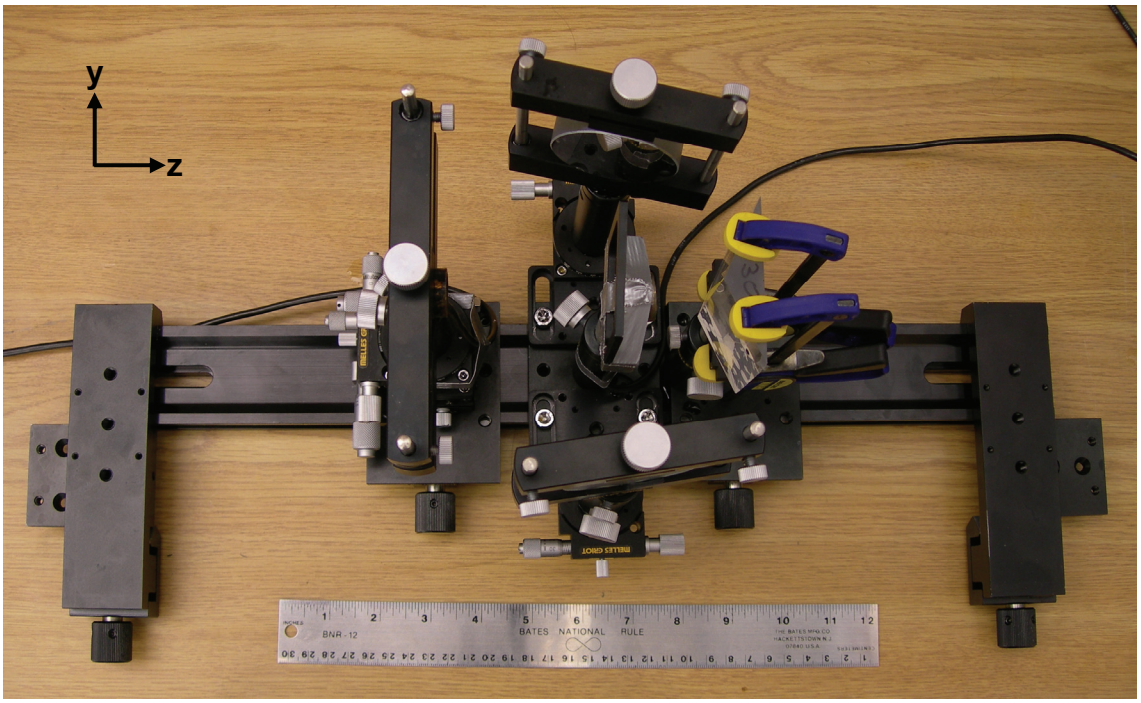

Figure 64: Holography Experimental Setup (out of water)

Transducer #3 acts as the emitter, which is shown in the centre of the diagram and transducer #1 acts as the detector, shown on the left-hand side. Two identical flat mirrors are positioned above and below the emitter. The 130° glass biprism is on the right-hand side. Note that the two beams hit the detector off-axis, as illustrated previously in Figure 38. This off-axis angle is the same for both beams.

The above picture shows the experimental setup out of water. When putting the apparatus in the water tank, it is turned upside-down and the rail rests on the top lid of the tank, as shown previously in Figure 45. The other components hang from the rail inside the water, and all positioning and rotational controls are easily accessible by hand. This is important when aligning all the components. The positioning and rotational controls were used to align the components and to make sure that the incoming pressure wave from the emitter was split approximately in half by the biprism. The alignment procedure can be time consuming, typically taking 30-60 min. However, once the alignment is complete, many measurements can be taken on various specimens without needing to realign the apparatus.

By covering one of the half-beams using a thick plastic shield, it is possible to measure the pressure signal at the detector due to the other half-beam. In this case, there is no interference. Using this technique, the signal from each of the half-beams was measured individually, and is shown in Figure 65.

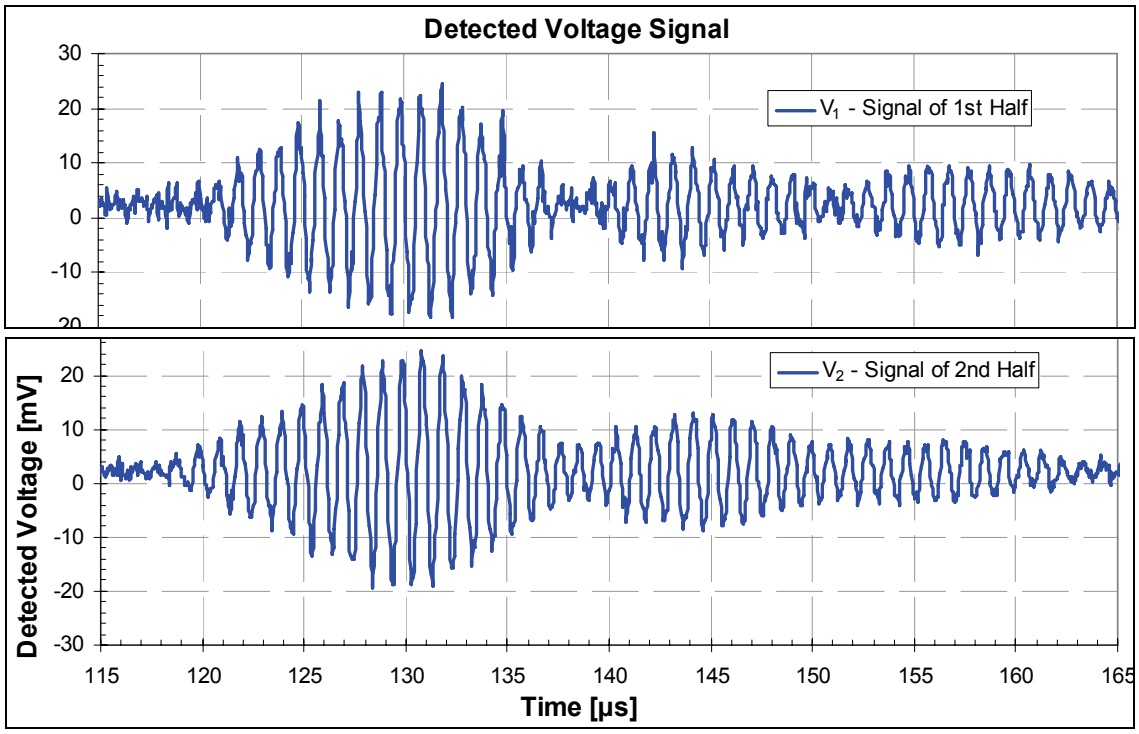

Figure 65: Individual Signals from the 2 Branches of the Interferometer

There are two important things to check when aligning the apparatus:

1) the two half-signals should be approximately equal in amplitude
2) the two half-signals should arrive at the detector at the same time

From the figure above, the signal of the 1st half has a maximum peak-peak amplitude of 47 mV, and the 2nd half has a maximum V_{p-p} of 43 mV. These are close enough to consider them as being approximately equal. Also, both signals arrive at the detector at approximately the same time. This is clear by considering one of the peaks, for example, the positive peak at 125 µs. For both V_1 and V_2, the peak at 125 µs matches up in time. Note that the voltage signals represent the pressure waves that travel through the water, since voltage is proportional to pressure. Therefore the incoming pressure wave is split into two equal pressure waves and the alignment procedure was successful.

When the two pressure waves are allowed to overlap, they interfere, and the resulting measured inference signal is shown in Figure 66. The blue (dark) line shows the measured interference signal.

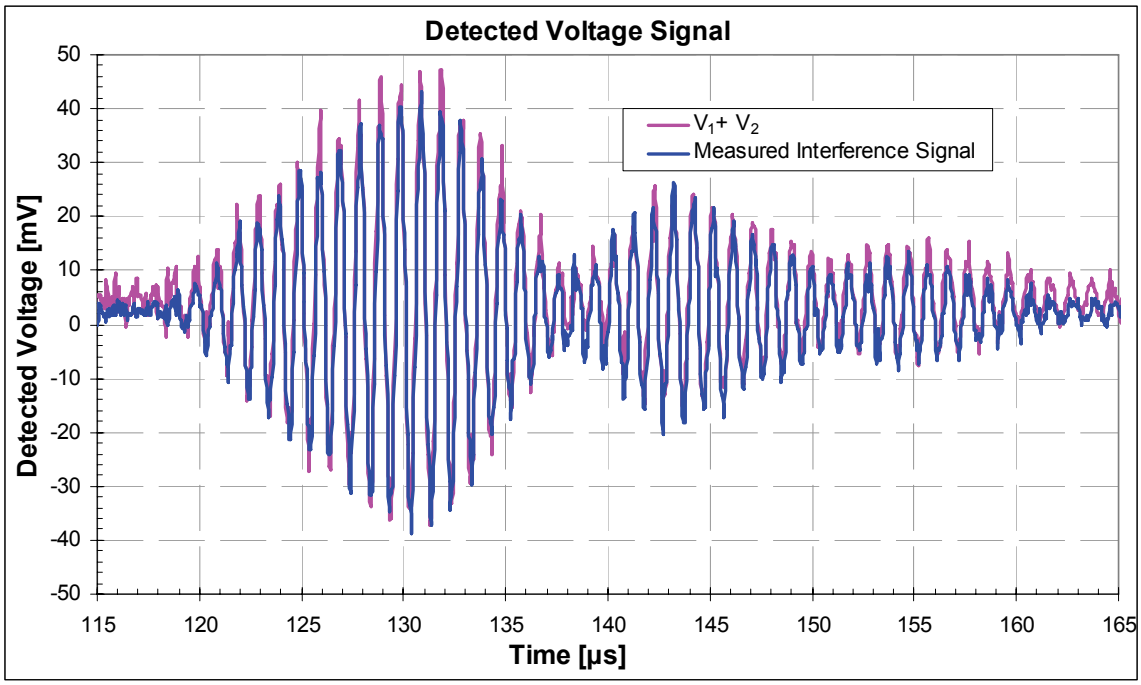

Figure 66: Measured Interference Signal and Mathematical Addition of Signals

The measured interference pressure signal is approximately double the amplitude of the original V_1 and V_2 signals, with a maximum peak-peak value of 81 mV. The pink (light) line, labelled, "V_1 + V_2" shows the result of mathematically adding the two original signals. As shown in the figure, the measured interference signal matches almost perfectly with the mathematical addition. This confirms that the voltage signals, and hence the pressure waves are additive, as predicted by equation (30). When we speak of interference in acoustics, we are really referring to the addition of pressure waves.

5.7.1 Reference Hologram

By scanning the detector horizontally (in the y-direction) across the interference pattern, and measuring the maximum peak-to-peak amplitudes, a spatial hologram can be constructed, as shown in Figure 67.

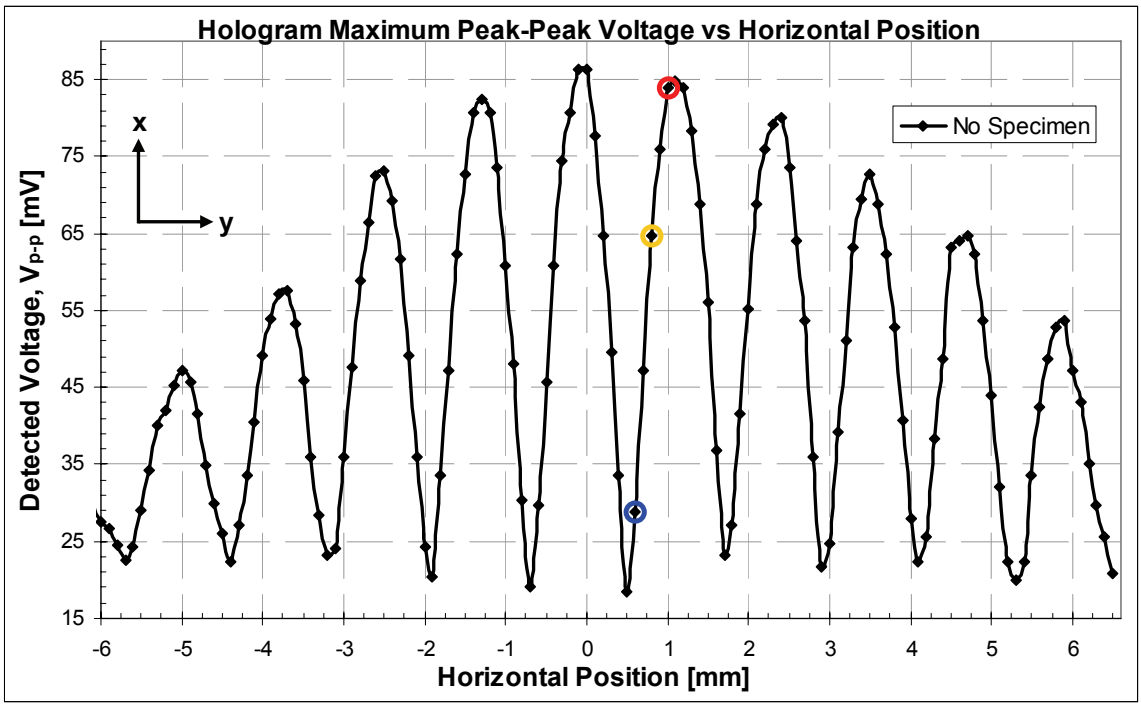

Figure 67: Measured Reference Hologram (Interference Pattern)

The fringe spacing for this spatial hologram, which is the distance between successive crests or troughs, is approximately 1.22 mm. The average water temperature during these measurements was 21.6°C This result matches up very well with the Zemax simulation shown previously in Figure 40, which had a fringe spacing of 1.18 mm. The small discrepancy (3%) can be accounted for by possible slight errors in the positions of the components in the experimental setup. The position of the detector, shown on the left side of Figure 64, is the most critical parameter that effects the fringe spacing. If the detector is moved backward, the fringe spacing will get larger, as shown previously in Figure 6.

When the fringe shifts are measured in units of *waves*, then the fringe shifts between two holograms will not depend on the fringe spacing. Likewise, phase shifts measured in units of *degrees* will not depend on the fringe spacing. This was shown previously in equation (53), which gives the fringe shift in terms of the index change, the specimen thickness, and the wavelength. Therefore, the exact value of the fringe spacing for the reference hologram is not significant, as long as it is kept constant for all subsequent measurements. However, the sample spacing should be such that several points are measured per oscillation. For the fringe spacing of 1.24 mm shown in Figure 67, scanning the detector in increments of 0.1 mm worked well.

The two interfering acoustic beams are not perfectly collimated, as in the simulated layout of Figure 38. Rather, the object and reference beams overlap and interfere more like the

spherical waves shown in Figure 6. In practise, the edges of the hologram are not nearly as well defined as in the simulated 2D hologram of Figure 40. Indeed, fringes could still be observed experimentally in the side region that appeared black (no intensity) in the simulated hologram. Despite the fact that Zemax uses collimated rays whereas experimentally sound travels as spherical waves (for small distances), the fringe spacing values do match up very well.

The maximum interference signal occurs at approximately 0 mm on the hologram in Figure 67. This corresponds to the case where the detector is exactly in the middle of the two incident interference beams. As an example of the hologram data collected, the voltage signal data for the three encircled points in Figure 67 are shown below in Figure 68.

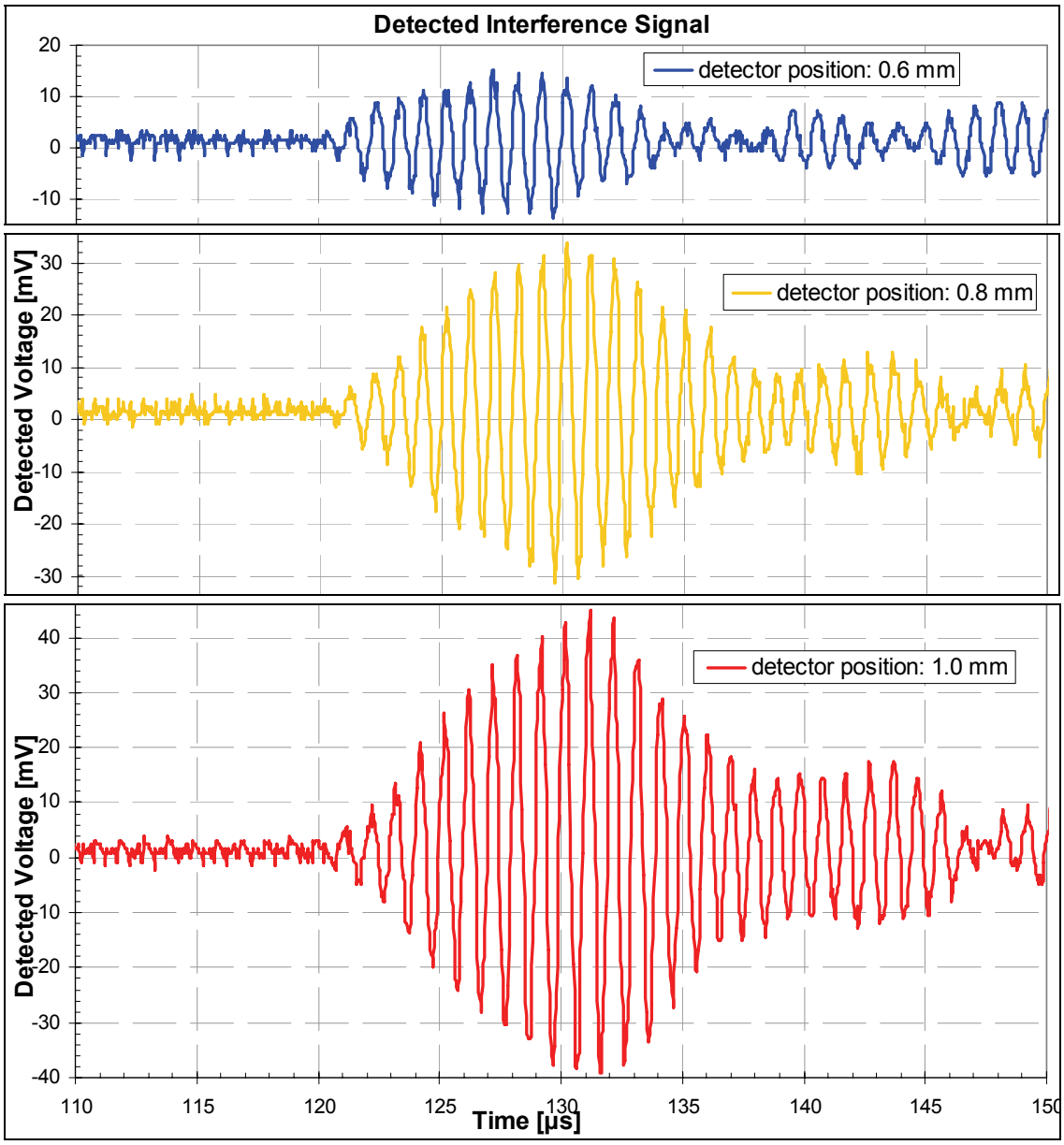

Figure 68: Three Interference Signals Measured for Spatial Hologram

The measured voltage signals shift slightly in time depending on the detector position, however it is only their maximum amplitude that is of interest. The maximum peak-peak voltages of the three signals are 28.8 mV, 64.8 mV, and 84 mV, respectively. These are the values for the encircled points in the spatial hologram of Figure 67. The time delay of approximately 120 µs corresponds to the 182 mm path length for each of the interfering beams. This path length is only technically valid when the detector is in the centre position (marked "0 mm" in Figure 67). It will be slightly shorter or longer for the two beams when the detector is scanned to an off-centre position. Note that crests in the hologram of Figure 67 appear rounded, while the troughs appear slightly narrower. This is likely because the error in the $V_{p\text{-}p}$ measurement is higher for the smaller amplitudes of the troughs. Conversely, the

V_{p-p} values for the crests of Figure 67 are numerically larger, so the relative error in their measurements is smaller for the crests than for the troughs.

The z-position of the detector was optimized experimentally in order to achieve the largest interference signal at y = 0 mm. There are two conflicting parameters: transmission loss due to spherical spreading and the directional sensitivity of the detector. The detector was positioned in the z-direction in such a way to optimize the two effects. For example, if the detector is moved to the right in Figure 64 or Figure 38, then the signal will drop, even though the beam path is shortened. This occurs because the two incident beams will hit the detector at a broader angle. The detector is most sensitive to incoming pressure waves along its "beam axis", shown previously in Figure 62 and Figure 63. It is less sensitive to incident pressure waves that are off-axis, where the wave vector is tilted with respect to the beam axis. However, if the detector is moved too far back, then spherical spreading loss will begin to dominate. The Zemax simulations do not take into the account the directivity of the detector or spherical spreading, therefore the position of the detector needed to be optimized experimentally (during the alignment procedure). This information was then fed back into the Zemax design before the simulation of the fringe spacing was performed, (Figure 40).

The detector used in these experiments was not an ideal point detector. Instead, it contains a circular disc with an active area of approximately 1 cm diameter. With a point detector, the acoustic intensity (energy per unit area) measured at a crest would be very high, and at a trough, it would be very low. In other words, the contrast of the fringes would be greatly increased with a smaller detector area. However, with the 1 cm detector, using scanning steps of 0.1 mm, the hologram fringe locations were measured exactly as we would expect if we used an array of very small detectors, as in the Zemax simulations. This seems to be a surprising result, since we would not have expected that such a large detector would be able to measure the fine fringe spacing of 1.22 mm. The fact that it was possible to measure the fringes suggests that the detector measures the average pressure, and the voltage values measured in Figure 67 were actually an average of the total number of crests and troughs within the active area of the detector. This concept is illustrated schematically in Figure 69, which shows two different scan positions for the same detector. The left side represents scan position "1.0 mm" and the right side represents scan position "0.6 mm".

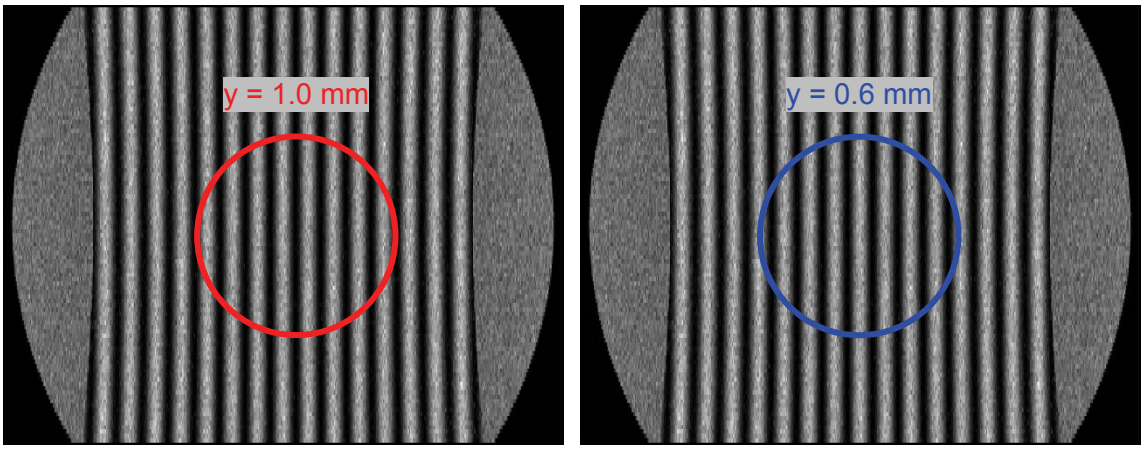

Figure 69: Scanning of a Circular Detector over a 2D Acoustic Hologram

The interference patterns represent a 2D acoustic hologram, with high relative pressure shown as a bright (white) and low relative pressure shown as dark (black). The circle represents the active area of the detector at two different positions within the same hologram. Although this diagram was fabricated for conceptual purposes, it is scaled approximately to represent a fringe spacing of 1.22 mm and a detector diameter of 1 cm. In scan position "1.0 mm", the circular detector "sees" 8 bright fringes and 7 dark fringes. Therefore, the average pressure measured over the whole area of the detector will be high, (recall that the measured voltage value was 84 mV). However, for scan position "0.6 mm", the circular detector "sees" 7 bright fringes and 8 dark fringes. Therefore, the average pressure measured over the whole area of the detector will be low, (recall that the measured voltage value was 28.8 mV). Also, the detector is more sensitive near its central beam axis than towards the edges (recall Figure 63) which would further contribute to this averaging effect. Overall, this means that a larger detector area will cause a decrease in the fringe contrast, because it will average multiple pressure peaks and valleys in the measurement at each horizontal position in the hologram. On the other hand, if a small point detector was used, it would get better fringe contrast.

Note also that the overall amplitude of the fringes in Figure 67 is high near the middle of the hologram (0 mm) and gets lower towards the left and right edges (near -5 and 6 mm). As expected, the fringe contrast is highest near the centre, where the beam overlap is greatest, and lowest near the edges, where the beam overlap is smallest. This trend is almost identical to the pressure variation measured in the beam-profile in Figure 62. In other words, the hologram of Figure 67 can be thought of as the multiplication of a constant amplitude sinusoid function times the overall amplitude "*envelope*" of Figure 62.

The horizontal scanning is very time consuming. It can take up to 60 minutes to collect a single reference hologram. Unfortunately, the water temperature can change over the

course of the measurements. It was observed to change as much as 1°C / hour, which would cause an error in hologram measurements. Ideally, we would want to use a 1D or 2D array of point detectors that could collect all the data points in Figure 67 simultaneously. Also, through automation several hologram measurements could be taken and averaged for each scan position in the specimen. The entire 3D scan of the specimen would only take a few minutes, and therefore temperature variation of the water in the tank would not be an issue. This sort of ideal design is the goal for the future, when more funding is available.

5.7.2 Specimen Holography Measurements

Holograms were measured for specimens of mineral oil and vinegar, in the polypropylene cuvettes. The apparatus used to hold one of the cuvettes is shown in the Figure 70.

Figure 70: Holder for Polypropylene Cuvette, with Liquid Specimen

Rather than using the "No Specimen" hologram of Figure 67 as the reference case, a cuvette filled with water was used as a reference for the other measured specimens. By doing this, any phase shift of the holograms caused by the polypropylene would cancel out, and only the effect of the actual specimen would be measured. The complete hologram measurement setup is shown in Figure 71, including the specimen holder, which sits on the bottom of the tank.

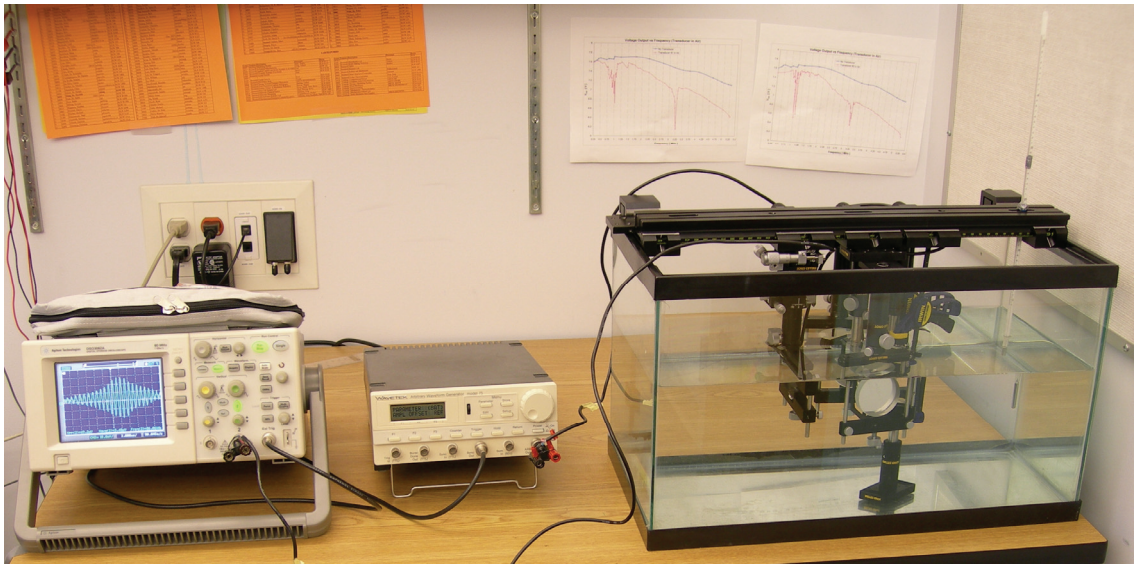

Figure 71: Complete Holography Experimental Setup with Specimen

The instrument on the left is an *Agilent* Technologies DSO3062A Digital Storage Oscilloscope, which was used to measure the signal from the detector. The instrument in the middle is a *WaveTek* Arbitrary Waveform Generator model 75, which was used to excite the emitter. A cable connecting the AWG to the scope acted as a trigger to set zero-time for the scope. On the right-hand side of the tank is an immersion mercury thermometer, used to measure the temperature of the water, to an accuracy of 0.1°C. The average water temperature was measured to be 21.7 °C for the duration of the holography experiments. From equation (6), this corresponds to a speed of sound of c_w = 1488.1 m/s. For a frequency of 1 MHz, this corresponds to a wavelength of λ = 1488.1 μm. Using equation (53), and a specimen thickness of 10 mm, this gives an index change of:

$$\Delta n = \frac{\lambda}{L} = \frac{1488.1\,\mu m}{10\,mm} = 0.14881 \qquad \text{[per fringe shift]}$$

Using the measured speed of sound values shown in Table 7 along with equation (46), a prediction of the expected fringe shift and phase shift was made for each specimen, as shown in the following table.

Table 8: Expected Fringe and Phase Shifts for Specimens

specimen	c_{sp} [m/s]	$n = \frac{c_w}{c_{sp}}$	$\Delta n = n_w - n_{sp}$	expected fringe shift [# of fringes]	expected phase shift [°]
Ethanol	1147.8	0.7713	-0.2287	-1.537	-553.2°
Isopropanol	1153.1	0.7749	-0.2251	-1.513	-544.6°
Mineral Oil	1450.9	0.9750	-0.0250	-0.168	-60.5°
Water (21.7°C)	1488.1	1	0	0	0°
Vinegar	1514.6	1.0178	0.0178	0.120	43.2°
Glycerine	1900.3	1.2770	0.27702	1.862	670.2°

Since we already confirmed that the Zemax simulations matched up well with the theoretical calculation for the fringe shifts (section 4.7), the final step was to measure the fringe shifts experimentally and compare them to the expected values. When placing a specimen in the object beam, the fringe spacing should stay the same, but the fringe positions are expected to shift, depending on the "strength" of the phase object. A strong phase object will cause a large fringe shift and a weak phase object will cause a small fringe shift. The two smallest phase objects were chosen for these experiments to avoid any ambiguity of phase shifts larger than 360° (fringe shifts > 1 spacing). These specimens were mineral oil and vinegar, which should have a phase shift of -59° and +42°, respectively, when compared to the water specimen. Figure 72 shows the actual results of the hologram measurements for these three specimens.

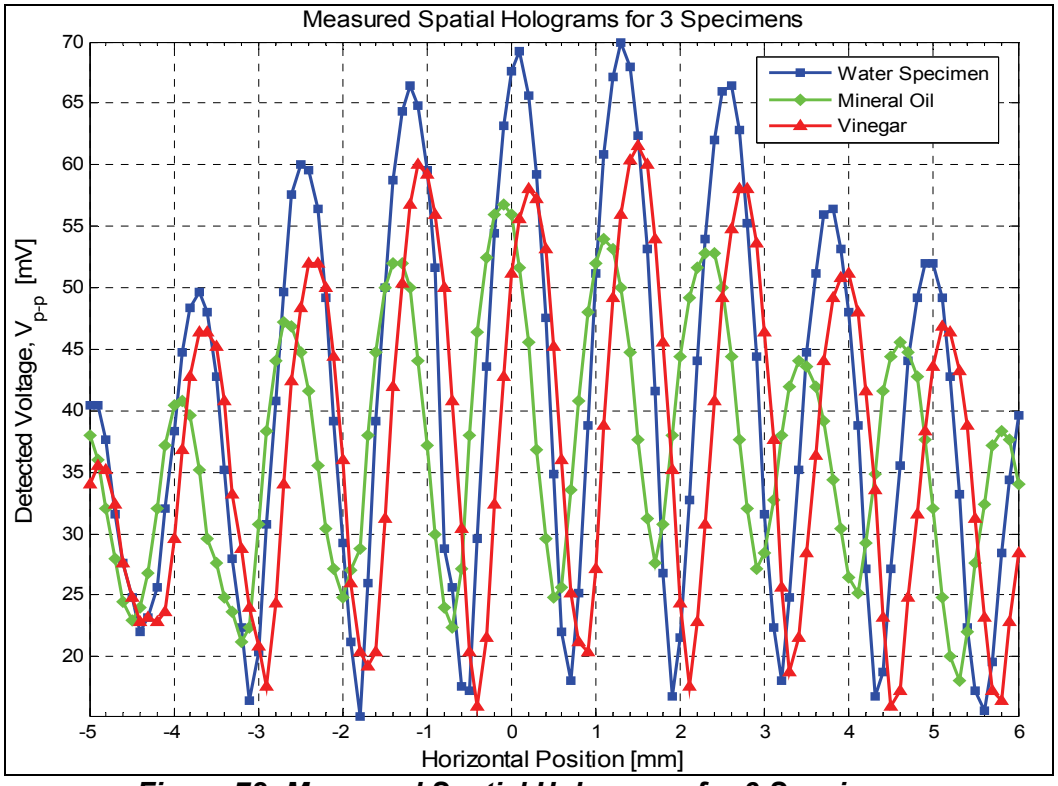

Figure 72: Measured Spatial Holograms for 3 Specimens

For the three holograms, the fringe spacing is approximately 1.24 mm. Compared to the water specimen reference hologram, the mineral oil hologram is shifted slightly to the left and the vinegar hologram is shifted slightly to the right. Although the actual direction of the fringe shift will depend on which half-beam is chosen as the object beam (recall Figure 41), the two specimens have their fringe shifts in opposite directions, as expected from the prediction in Table 8. Note that it does not matter where the specimen is placed within the object beam, but an approximate specimen position was used, as shown in Figure 41. The

measurement of the fringe shifts and phase shifts was done mathematically, using the three methods described in the following section.

5.7.3 Phase Shift Measurements

There are three methods that were used to calculate the fringe shift between the holograms of the previous figure. They are: the Fourier Transform (FT) method, the Curve Fitting method, and the Autocorrelation method, which are described in the next three sections. The Curve Fitting method was found to work the best, especially for a limited number of collected data points. The results for the three methods are summarized in Table 9. The last column shows the expected theoretical phase shifts from Table 8.

Table 9: Measured Phase Shifts of Holograms

Specimen Holograms	Measured Phase Shift (3 methods)			Theoretical Phase Shift
	FT	Curve Fit	Autocorrelation	
Mineral Oil	-61.1°	-60.9°	-58.4°	-60.5°
Water	0°	0°	0°	0°
Vinegar	45.5°	45.6°	46.7°	43.2°

The results of all three methods were all very similar to each other, with the FT method and the Curve Fitting method giving almost the same result. The Autocorrelation value did not quite match up with the other two methods and it bears the largest error in the currently used experimental conditions (as explained in section 5.7.3.3) so it was rejected as less accurate than the other two methods. For the FT and Curve Fitting values, the mineral oil phase shift was within 3% of the predicted value, and the vinegar phase shift was within 6%, which were both very close. Note that the average temperature for the hologram measurements was 21.7°C, while the specimen speed of sound values from Table 7 and Table 8 (used in the predictions) were measured at an average temperature of 20.1°C. This small temperature difference would affect the measured speed of sound values and this could account for the discrepancy between the phase shift measurements and the prediction. Overall these results are very encouraging, despite the crude methods used for data acquisition, (ex. manual scanning and large detector size). This confirms that the experimentally measured phase shifts, the theoretical calculations, and the Zemax simulations are all in good agreement.

Before applying one of the three mathematical methods to measure phase shift, the three specimen signals shown above in Figure 72 were first shifted vertically so that their average value was zero. They were also normalized to have a maximum amplitude of 100%, as shown in Figure 73.

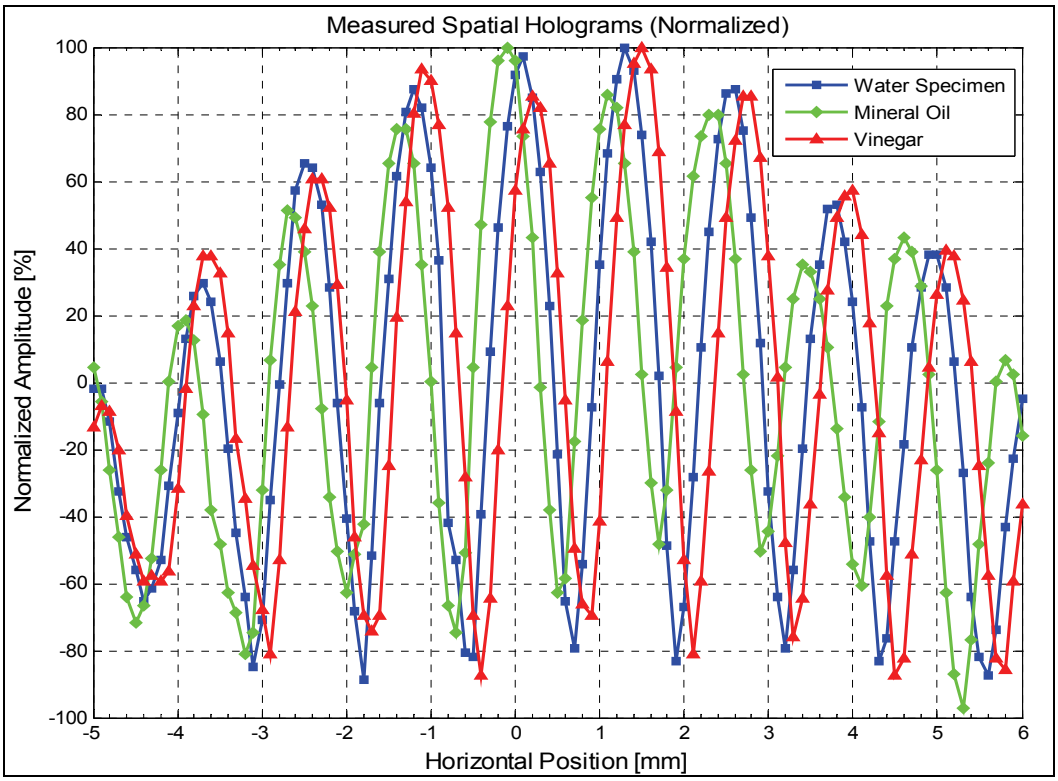

Figure 73: Measured Spatial Holograms for 3 Specimens (Normalized)

5.7.3.1 Fourier Transform Method

The Fourier Transform method is the most frequently used method to measure phase shifts in holography. The FT method is ideal for analysing differences in 2D holograms since the FT function can easily extend to two-dimensional data. The Matlab code used for this method is given in Appendix B. The FT method uses the following steps:

1) take the Fourier Transform of the hologram signal
2) find the spatial frequency with the maximum (peak) intensity
3) put a window around the maximum frequency peak using a Hanning filter (optional)
4) set all other frequency components to zero intensity
5) shift the windowed peak intensity to the zero frequency position
6) take the Inverse Fourier transform of the filtered frequency data
7) take the argument of the signal to calculate its constant phase value

Note that steps 2-6 are performed in the frequency domain, while steps 1 and 7 are in the spatial domain. Applying step 1 for the three holograms above produced the following spatial frequency spectra shown in Figure 74. The position spacing was 0.1 mm, the sample frequency was 10 mm^{-1}, and the frequency spacing in the Fourier domain was 0.091 mm^{-1}. The average spatial frequency for the three holograms is f_f = 0.81 mm^{-1}, which corresponds to an average fringe spacing of λ_f = 1.24 mm.

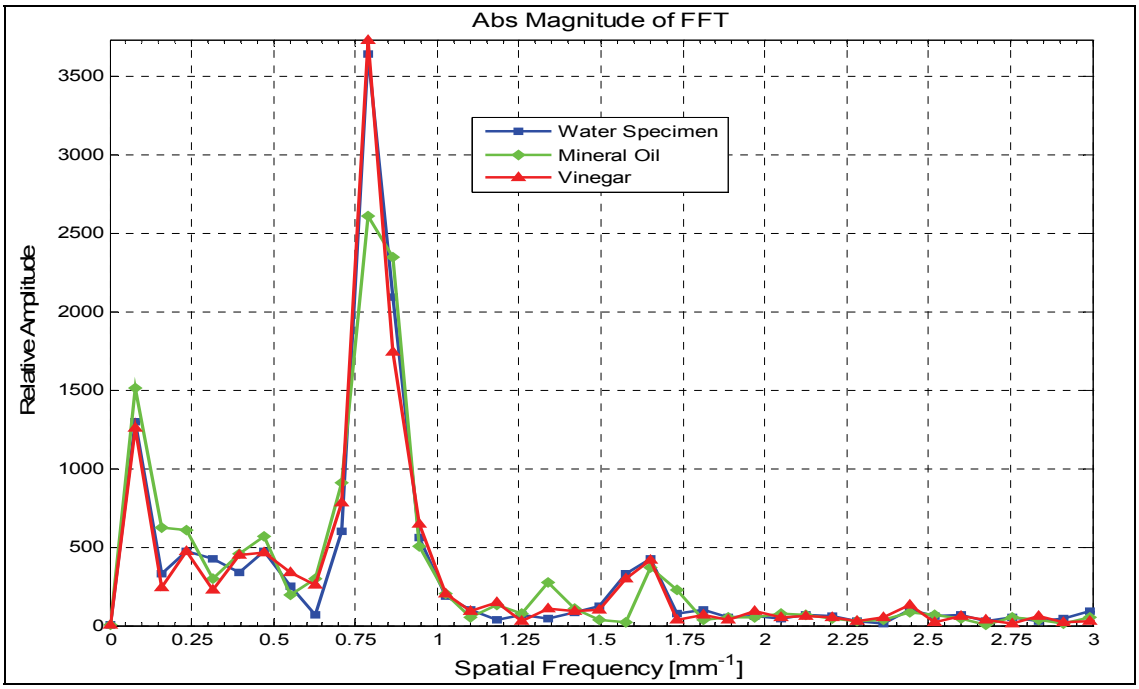

Figure 74: Spatial Frequency Spectrum of 3 Measured Holograms

To better illustrate the differences between the Fourier Transforms of the holograms, the FTs are broken into their real and imaginary components in Figure 75.

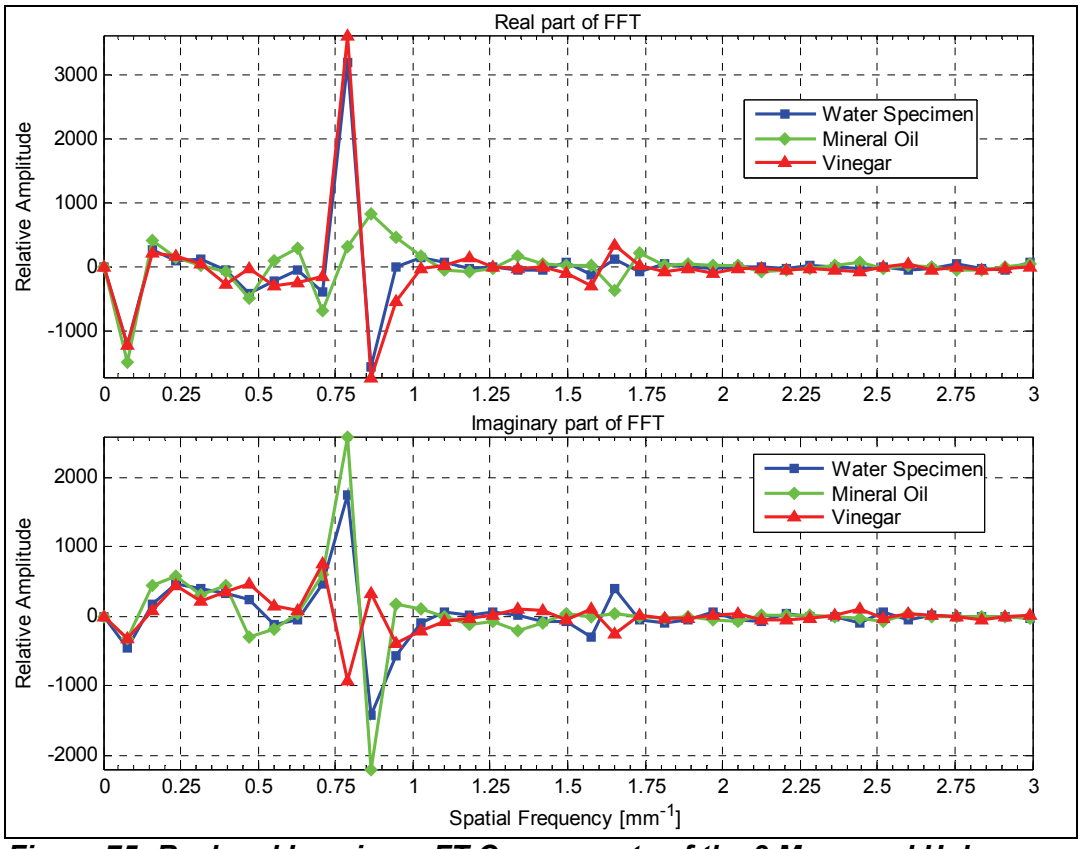

Figure 75: Real and Imaginary FT Components of the 3 Measured Holograms

Step 3 is optional and it was not used since it was still possible to obtain reasonable results without resorting to such detailed filtering in the frequency domain. The results of steps 4 and 5 are shown in Figure 76.

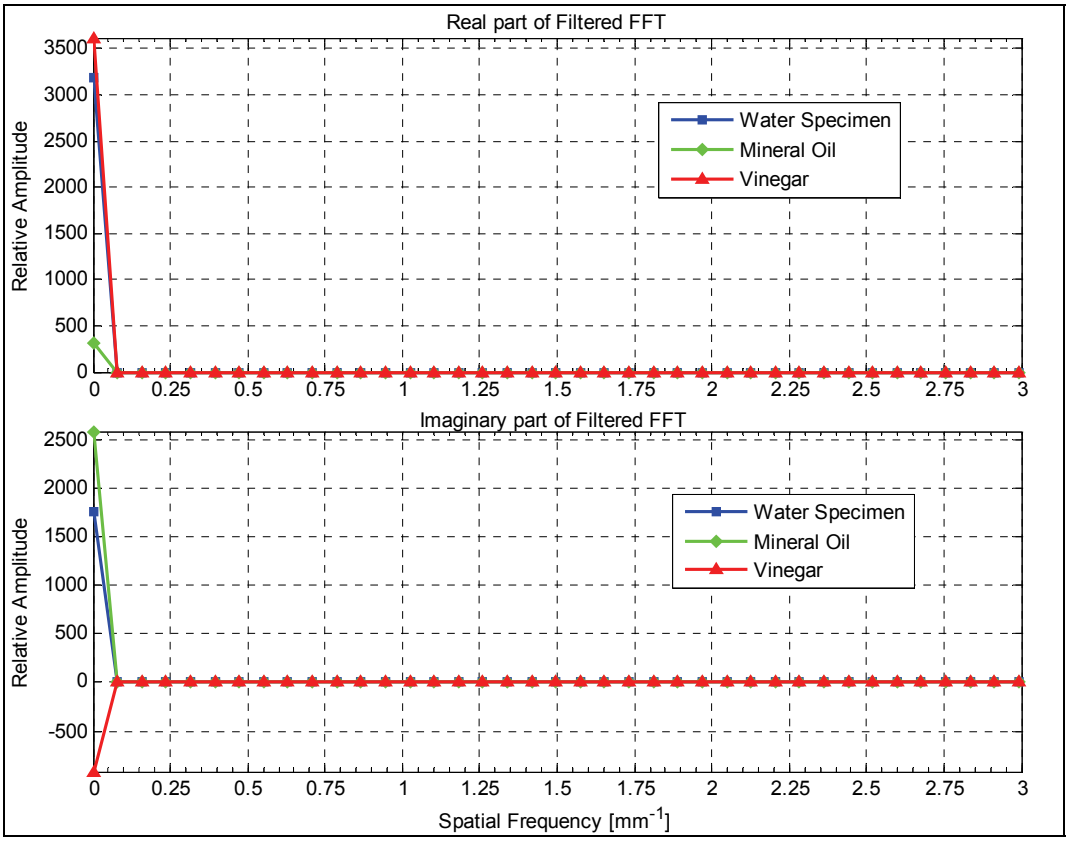

Figure 76: Real and Imaginary FT Components of 3 Holograms after Filtering

The resulting phase measurements of step 7 are given in Figure 77.

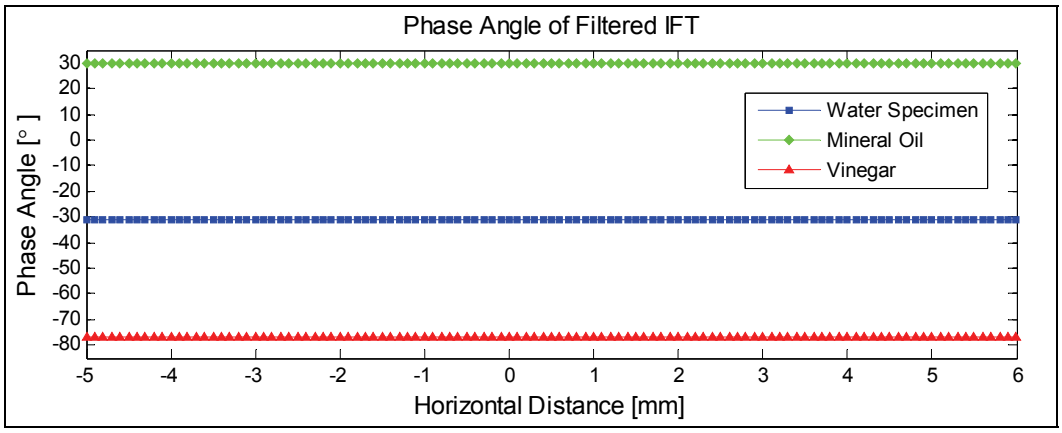

Figure 77: Phase Angle of Filtered IFT for 3 Holograms

The figure shows the measured phase angles of the water, mineral oil, and vinegar holograms to be -31.2°, 29.9°, and -76.6°, respectively. This means that the phase shift between the water hologram and the mineral oil hologram is -61.1°, and the phase shift

between the water hologram and the vinegar hologram is 45.5°. These are the values shown in Table 9.

In general, the FT method gives a better result for a large number of fringes in the collected hologram, because the resolution in frequency space increases for a larger sampling window. In the future, if 2D holographic information is collected, the FT method can be easily extended to use 2D transforms and a 2D Hanning filter.

5.7.3.2 Curve Fitting Method

The code for the curve fitting algorithm is given in Appendix C. For this method, each of the three holograms was fitted to a general sinusoid function:

$$y(x) = A \cdot Sin\left(\frac{2\pi x}{\lambda_f} + \phi\right) + y_{ave} \tag{55}$$

where: A is a constant amplitude
x is the horizontal distance in [mm]
λ_f is the constant fringe spacing (distance between consecutive peaks)
y_{ave} is the average value, set to zero in this case
φ is the unknown phase of the sinusoid function in [rad]

The parameters used for the curve fitting algorithm were:

$y_{ave} = 0$
$A = 65$
$\lambda_f = 1.24$ [mm]

and the only unknown value was φ. The constant fringe spacing value of 1.24 mm was determined separately using the Fourier Transform Method, (described in section 5.7.3.1). Using least squares fitting of the y vs x data, the φ value was determined for the three holograms. Figure 78 shows the results of the curve fitting for the water specimen (reference) hologram.

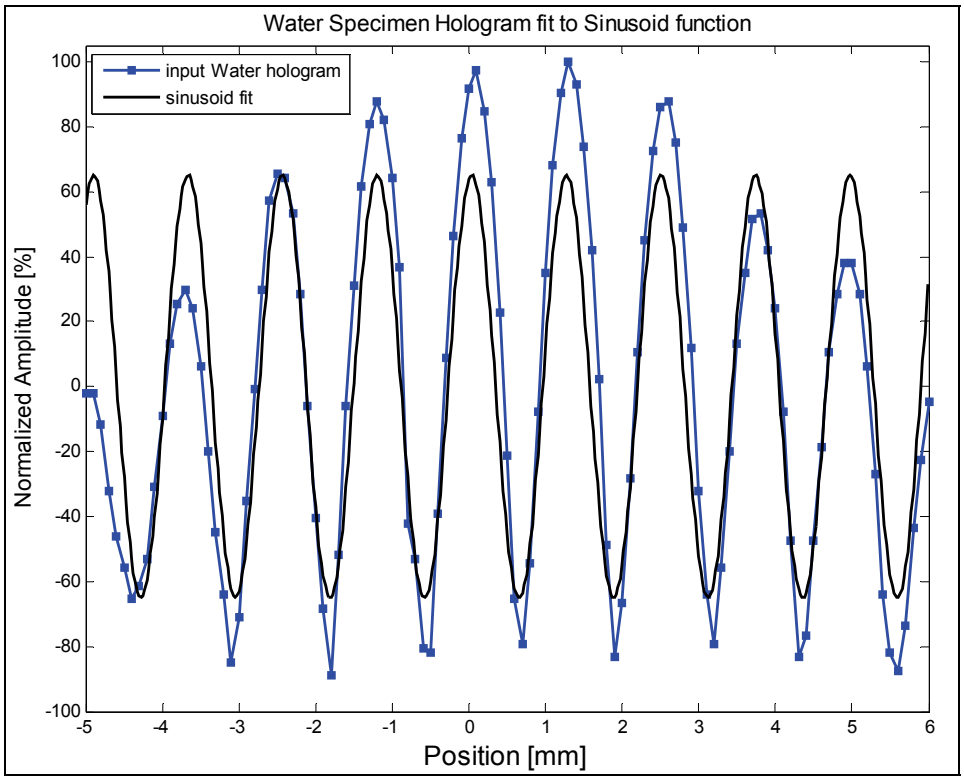

Figure 78: Sinusoid Fitting for Water Hologram

The blue squares represent the actual collected data for the water hologram (after normalization). The blue line connecting the blue squares is shown for illustrative purposes only. The black line represents the least-squares fit of the hologram data to the general sinusoid function. Note that the sinusoid fit has a constant amplitude, whereas the original hologram data has highest amplitude at the centre (0 mm) with decreasing amplitude towards the edges (-5 mm and 6 mm). A constant amplitude of 65 and a fringe spacing was chosen for the sinusoid-fit curve. Despite the mismatch in amplitudes, the phase of the sinusoid-fit curve matches up very well with the phase of the original hologram data. Therefore, the fitting algorithm was very successful in finding the unknown phase of the hologram. This phase was measured to be 78.4° for the water hologram.

Note also that the fringes near the middle of the hologram (around 0 mm) fit better than the fringes near the left and right edges (near -5 and 6 mm). This better fit is due to the better overlap of the two beams when the detector is at the centre, which is where the fringe contrast is highest. As discussed in section 5.7.1, the acoustic beams act like spherical waves. Therefore, there is likely some measurement error for the points near the edges of the holograms, where the beam overlap is less than ideal and the fringe contrast is low. Also, it is quite possible that some of the sound rays that make up the fringes near the edges of the holograms did not actually pass through the specimen, (recall Figure 36).

Consequently, the fringe spacing appears to change slightly near the left and right edges of three measured holograms.

Using the same parameters for the fitting algorithm as above, the phase of the mineral oil hologram was found, and the result of the curve fitting is shown in Figure 79.

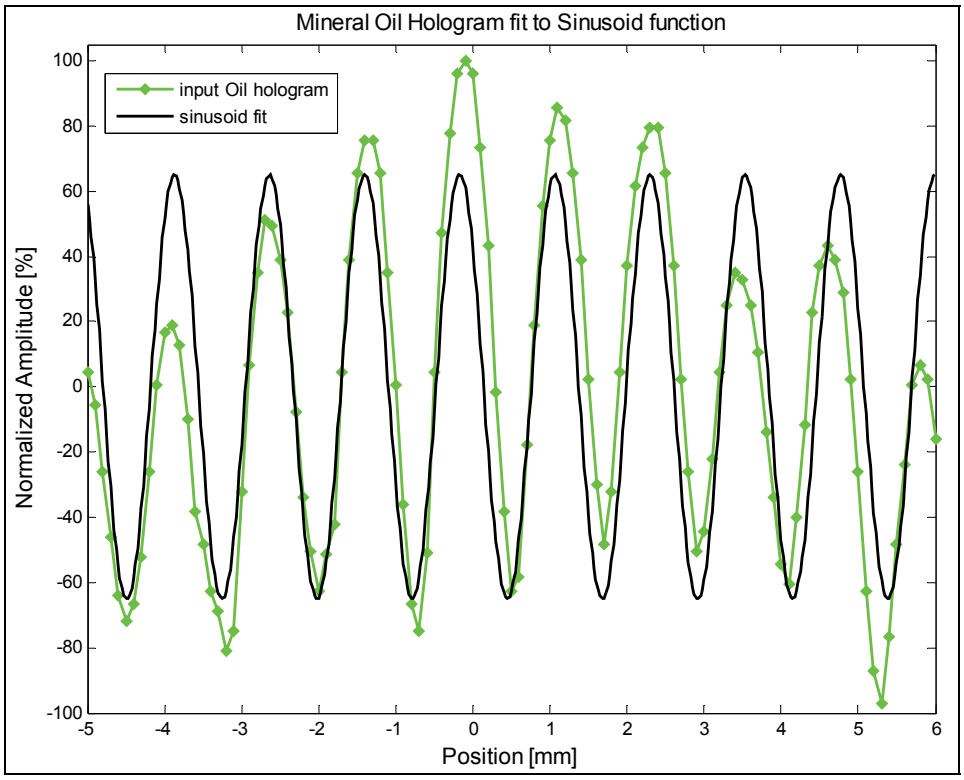

Figure 79: Sinusoid Fitting for Mineral Oil Hologram

The green coloured (diamond) points and green line show the original hologram data and the black line is the least-squares fitting of the data to the sinusoid function. The phase for this hologram was measured to be 139.3°, giving a phase shift of -60.9° between the water and mineral oil holograms. This is the value shown in Table 9. The result of the curve fitting for the vinegar hologram is shown in Figure 80.

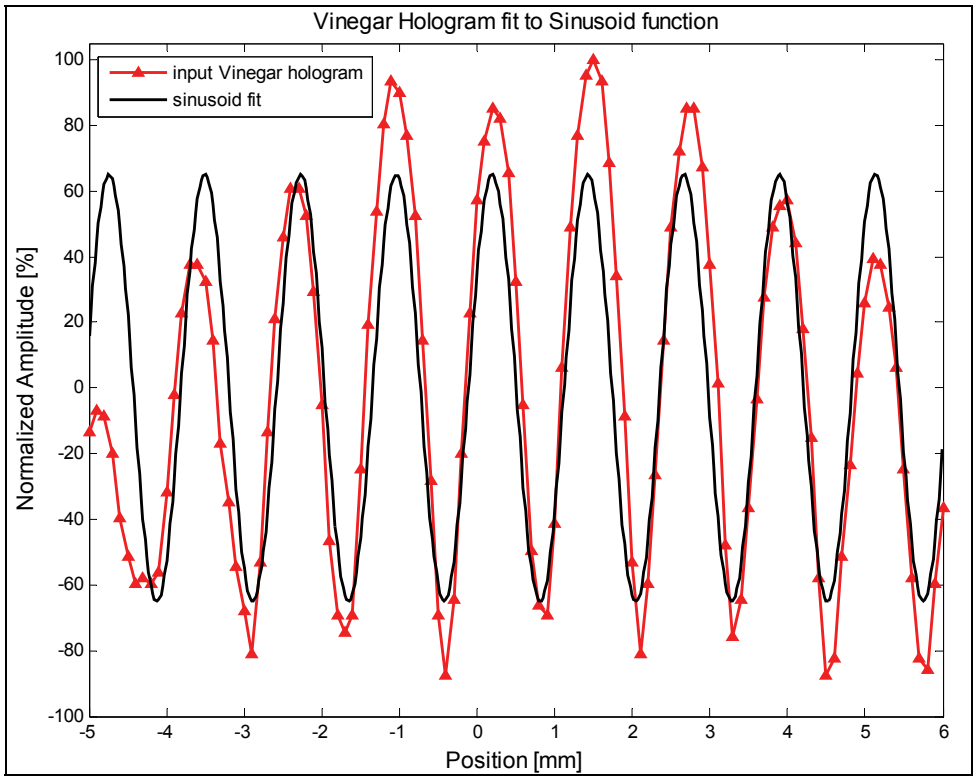

Figure 80: Sinusoid Fitting for Vinegar Hologram

The red coloured (triangle) points and red line show the original hologram data and the black line is the least-squares fitting of the data to the sinusoid function. The fitting does not appear to be very good near the left edge of the hologram. As mentioned earlier, there will be a larger error in the hologram measurements near the edges, where the beam overlap is less than ideal. The phase for this hologram was measured to be 33.0°, giving a phase shift of 45.4° between the water and mineral oil holograms. This is the value shown in Table 9.

The Curve Fitting method was found to work very well with the measured holograms, all of which contained 111 data points. This method may work even better when there are more data points, however it is likely to be the most accurate out of the three methods for a small number of data points.

5.7.3.3 Autocorrelation Method

Autocorrelation or Crosscorrelation are commonly used to compare time-varying electrical signals and to determine how similar they are. Two electrical signals that are highly correlated usually have some physical connection between them. In other words, the correlation function would have one or more non-zero values. Conversely, for two phenomena that not physically connected or related, we would not expect any correlation between them. In other words, all values of the correlation function would go to zero. When the two signals being compared are the same or approximately the same, the technique is

called autocorrelation. The algorithm works as follows. Two signals s and k, with N discrete elements, can be represented by two arrays of elements:

s_1	s_2	s_3	…	s_i	s_{i+1}	…	s_N
k_1	k_2	k_3	…	k_i	k_{i+1}	…	k_N

In order to generate the autocorrelation sequence, the lower row is progressively shifted (one cell at a time) to the right and the s and k elements are multiplied and summed. The 0th term of the autocorrelation sequence is: $r_0 = \sum_{i=1}^{N} s_i k_i$. The 1st term is $r_1 = \sum_{i=1}^{N} s_i k_{i-1}$, the 2nd term is $r_2 = \sum_{i=1}^{N} s_i k_{i-2}$, and so on for the complete autocorrelation sequence: $r = (r_{-N}, \ldots, r_0, \ldots, r_N)$, having a total of 2N+1 elements. In general, the nth term of the autocorrelation sequence has the value: $r_n = \sum_{i=1}^{N} s_i k_{i-n}$. Two identical signals that are displaced horizontally will have the strongest correlation (highest value of r_n) when they overlap perfectly. Two signals that are only approximately equal will still have a maximum value of r_n when the signals match up the best. The Matlab code used for this process is shown in Appendix D. Figure 81 shows the correlation sequence for the mineral oil and vinegar holograms, both with respect to the water hologram.

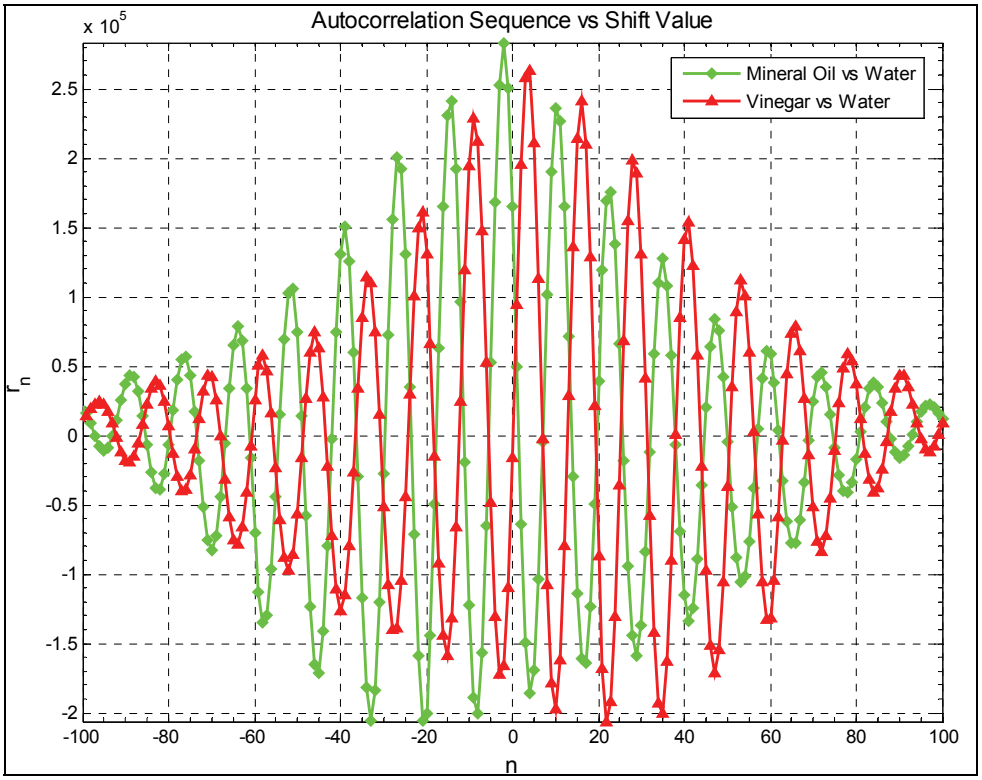

Figure 81: Autocorrelation Sequences

For the "Mineral Oil vs Water" data, since both of the input signals are periodic, then the output autocorrelation sequence is also periodic. The same is true for the "Vinegar vs Water" data. Both of these autocorrelation sequences have a peak value near n = 0. The green line peaks at n = -2, and red line at n = 2. This means the mineral oil and water holograms match up the best when the mineral oil hologram is shifted 2 pixels to the left. The vinegar oil hologram matches up best with the water hologram when it is shifted 4 pixels to the right. Normally, autocorrelation has a resolution of 1 data point (pixel), which is limited by the original spacing of the collected data. In this case the sample spacing was 0.1 mm, so n = ±2 would correspond to a shift of ±0.2 mm. However, the original data can be interpolated to improve the resolution of this measurement. Figure 82 shows the results of the autocorrelation when the data is interpolated by a factor of 5. The original data had 111 data points, whereas the interpolated data has 555 data points. This figure shows a zoom-in view of the central peaks in the two autocorrelation sequences.

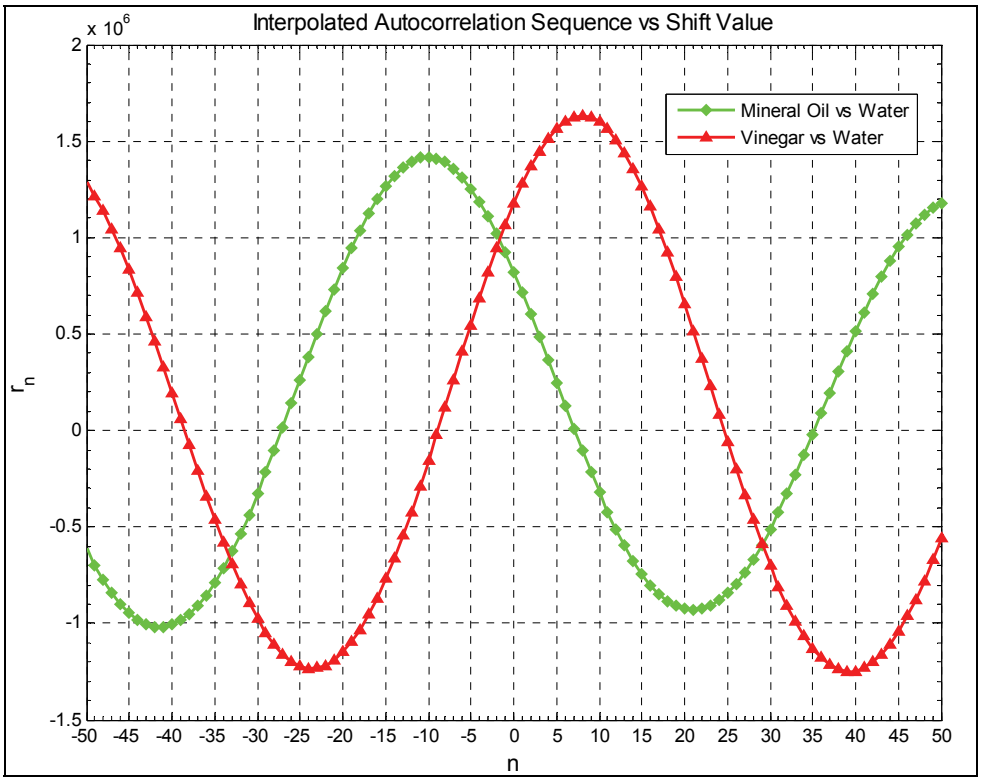

Figure 82: Zoom-in of Central Peak of Autocorrelation Sequences (Interpolated)

In this case, the green sequence peaks at n = -10 pixels and the red sequence peaks at n = 10 pixels. The phase shift in degrees can be calculated using the following conversion:

$$\Delta\phi = \text{pixel shift} \cdot \frac{\text{sample spacing}}{\text{interpolation factor}} \cdot \frac{360^\circ}{\lambda_f} \tag{56}$$

Using this equation, the phase shift for the mineral oil hologram with respect to the water hologram is:

$$\Delta\phi = -10\,\text{pixels} \cdot \frac{0.1\,\frac{\text{mm}}{\text{pixel}}}{5} \cdot \frac{360°}{1.24\,\text{mm}} = -58.4°$$

For the vinegar hologram it is:

$$\Delta\phi = 8\,\text{pixels} \cdot \frac{0.1\,\frac{\text{mm}}{\text{pixel}}}{5} \cdot \frac{360°}{1.24\,\text{mm}} = 46.7°$$

These are the values shown in Table 9. The constant fringe spacing value of 1.24 mm was determined separately using the Fourier Transform Method, (described in section 5.7.3.1). The autocorrelation results did not match up quite as well to the theoretical predictions as the other two methods. This is likely because autocorrelation is limited by the spacing of the collected data points. Interpolating between the collected data points to give a smaller sample spacing was somewhat useful, however autocorrelation would work much better if the original holograms were sampled with a finer spacing.

6 DISCUSSION & CONCLUSIONS

6.1 Discussion

In this research, we successfully designed a prototype Confocal Acoustic Holography Microscope. The estimated specifications of the design included a frequency of 2.25 MHz, a resolution in sound speed changes of 16 m/s, a resolution in temperature changes of 5°C, and a spatial resolution of 660 μm. With future improvements to the CAHM, utilizing the latest technologies such as 2D array detectors, MEMS, and acoustic lenses, we expect to be able to measure changes in sound speed of 1 m/s, changes in temperature of 0.5°C, and a spatial resolution of 150 μm.

In addition to designing and evaluating the prototype CAHM, the goal of the current research was to use currently available equipment to design and construct a low cost proof-of-concept acoustic holography instrument. This simplified acoustic holography instrument used a collimated object beam rather than a convergent object beam and did not use confocal apertures. A detector with a 1 cm diameter active area was used to manually scan across the acoustic holograms and build up the holographic information, rather than using an ideal linear array detector. The total cost of the simplified experiment was effectively zero, since all of the components were borrowed. The cost of the prototype CAHM design shown in section 3 would be approximately $40,000, as detailed in Table 3.

Using the simplified acoustic holography setup, some very successful acoustic holography results were obtained, which validated the proof-of-concept of the instrument. The acoustic holograms were scanned by a 1 cm diameter detector in steps of 0.1 mm. The measured fringe spacing for the reference hologram was 1.22 mm and this value matched up well with the Zemax simulations, which predicted a fringe spacing of 1.18 mm. The small discrepancy (3%) was attributed to slight errors in the positions of the components in the experimental setup.

Acoustic holograms were also collected for fluid specimens of acetic acid and mineral oil and were compared to the reference case (distilled water). The fringe spacing measured for these three cases was 1.24 mm, which matched up well with the Zemax simulations (5% difference). The predicted phase shifts for the holograms were -60.5° for the mineral oil and 43.2° for the acetic acid. These predictions were based on the theoretical calculation of equation (53), which were shown to match well with the Zemax simulations in Figure 33, with no detectable discrepancy. The experimentally measured phase shifts of the specimen holograms were then found to match up well with the theoretical calculations and the Zemax

simulations, as outlined in Table 9. The measured mineral oil phase shift was within 3% of the predicted value, and the vinegar phase shift was within 6%.

In another set of experiments, the sound speed of fluid specimens of ethanol, isopropanol, acetic acid, glycerine, and mineral oil were measured by observing the time delay of a 1 MHz sound pulse travelling through a 1 cm thick specimen-filled cuvette. The measured speed of sound values matched up well with the literature, as shown in Table 7, with the discrepancies all less than 2%. These results showed that despite using less than ideal equipment, the simplified experimental setup could still make accurate speed of sound measurements. The experiments also confirmed that the acoustic phase shift caused by a specimen could be observed by either a spatial measurement (hologram fringe shift) or a temporal measurement (time advance/delay).

The mathematical methods used to process the 1D holograms and measure the phase shifts included the Fourier Transform method, the Curve Fitting method, and the Autocorrelation method. The Curve Fitting method was found to work the best out of the three methods, however the FT method may prove more useful in the future when processing information from 2D holograms.

The Nearfield Acoustic Holography method described in section 2.4.1 makes use of only a single object beam, whereas our CAHM method uses both an object beam and a reference beam to generate an interference pattern. Usually in NAH, the detector is required to have a very small spatial resolution, in the sub-millimetre range. However, for the simplified acoustic holography experiments performed in this investigation, it was possible to make useful measurements with a relatively large (1 cm diameter) detector. The reconstruction algorithm given in section 2.5.9.3 will work well only if the pressure data is measured to a high spatial resolution. On the other hand, the interferometry method used in our experiments does not require very high spatial resolution and the experiments worked well with our inexpensive detector.

6.2 Final Conclusions

Through our research, we successfully designed a prototype Confocal Acoustic Holography Microscope. The knowledge obtained from the proof-of-concept acoustic holography experiments will aid in the future construction of the actual prototype CAHM. The good agreement between the Zemax simulations and the experiments of the simplified acoustic holography instrument gives us confidence in the accuracy of the Zemax simulations for the

prototype CAHM. Therefore, the popular Zemax optical software can be effectively used to design acoustic instruments. To our knowledge, this is the first use of Zemax for acoustic designs.

Based on the successful results of the experiments and simulations obtained to date, the CAHM is expected to have many useful applications, such as in medical diagnostics where it could be used to measure density and temperature within the human body. Phase contrast images could also be used to help identify suspicious tissue lesions. Many other applications of the CAHM include non-destructive testing of electronic and mechanical parts, measurements of fluid samples, material science experiments, and microgravity experiments, where non-invasive examination is required.

6.3 Future Work

Further work in the construction of the CAHM will include the manufacturing of parabolic reflectors and apertures to implement the confocal property of the microscope, as discussed in the CAHM design of section 3. In addition, the microscope can be improved in the future by incorporating new features such as Micro-Electro-Mechanical Systems (MEMS), a 2D array detector, acoustic lenses, automatic scanning, and faster acquisition time. When the CAHM prototype is built, tests of more complicated specimens, including tissue samples, will verify the usefulness of the instrument for medical diagnostics. Research is ongoing at the University of Victoria [21,53] to develop new algorithms for reconstructing the 3D information collected when scanning a specimen with both an Acoustic and an Optical Confocal Holography Microscope.

6.4 Applications

With further development, the CAHM is expected to be a very useful tool for non-invasively measuring temperature and composition, with applications in fluids experiments, non-destructive testing of materials, and medicine. For example, there is currently no method to accurately measure temperature non-invasively in the human body and the CAHM would be an ideal candidate for this application. The CAHM, which is sensitive to small variations in sound speed, may also be able to detect subtle early signs of cancer or other diseases that affect the mechanical properties of tissue. A medical devices company called *Pentax Medical* has expressed interest in developing the CAHM technology for endoscopic ultrasound. Endoscopes are commonly used to probe the epithelial layers of the body, such as the respiratory and gastro-intestinal track. This implementation would require a miniature version of the CAHM.

7 REFERENCES & NOTES

[1] R. A. Herring, "Confocal scanning laser holography, and an associated microscope: A proposal", *Optik,* vol. 105, pp. 65-68, April 1997.

[2] P. Jacquemin, R. McLeod, D. Laurin, S. Lai, and R. A. Herring, "Design of a confocal holography microscope for three-dimensional temperature measurements of fluids in microgravity", *Microgravity Science and Technology,* vol. 17, pp. 36-40, 2005.

[3] T. Vo-Dinh, Biomedical photonics handbook. Boca Raton, Fla.: CRC Press, 2003.

[4] Y. Saijo, T. Ohashi, H. Sasaki, M. Sato, C. S. Jorgensen, and S. I. Nitta, "Application of scanning acoustic microscopy for assessing stress distribution in atherosclerotic plaque", *Annals Of Biomedical Engineering,* vol. 29, pp. 1048-1053, Dec 2001.

[5] Y. Saijo, T. Miyakawa, H. Sasaki, M. Tanaka, and S. Nitta, "Acoustic properties of aortic aneurysm obtained with scanning acoustic microscopy", *Ultrasonics,* vol. 42, pp. 695-698, Apr 2004.

[6] J. F. Greenleaf, M. Fatemi, and M. Insana, "Selected methods for imaging elastic properties of biological tissues", *Annual Review Of Biomedical Engineering,* vol. 5, p. 57, 2003.

[7] Y. Saijo, H. Sasaki, H. Okawai, S. Nitta, and M. Tanaka, "Acoustic properties of atherosclerosis of human aorta obtained with high-frequency ultrasound", *Ultrasound In Medicine And Biology,* vol. 24, p. 1061, Sep 1998.

[8] Y. Saijo, M. Tanaka, H. Okawai, H. Sasaki, S. I. Nitta, and F. Dunn, "Ultrasonic tissue characterization of infarcted myocardium by scanning acoustic microscopy", *Ultrasound In Medicine And Biology,* vol. 23, pp. 77-85, 1997.

[9] H. Sasaki, Y. Saijo, M. Tanaka, S. Nitta, T. Yambe, and Y. Terasawa, "Characterization of renal angiomyolipoma by scanning acoustic microscopy", *Journal Of Pathology,* vol. 181, pp. 455-461, Apr 1997.

[10] Y. Saijo, M. Tanaka, H. Okawai, and F. Dunn, "The ultrasonic properties of gastric-cancer tissues obtained with a scanning acoustic microscope system", *Ultrasound In Medicine And Biology,* vol. 17, pp. 709-714, 1991.

[11] U. Techavipoo, T. Varghese, Q. Chen, T. A. Stiles, J. A. Zagzebski, and G. R. Frank, "Temperature dependence of ultrasonic propagation speed and attenuation in excised canine liver tissue measured using transmitted and reflected pulses", *Journal of the Acoustical Society of America,* vol. 115, p. 2859, 2004.

[12] DCITA. "The eidola suite: Holograms at questacon", Department of Communications, Information Technology and the Arts, Australian Government, updated October, 2006. http://archive.dcita.gov.au/2002/08/artbeat_winter_2002/the_eidola_suite_holograms_at_questacon.

[13] D. Gabor, "Microscopy by reconstructed wave fronts", *Proceedings of the Royal Society of London, A,* vol. 197, pp. 454-487, 1949.

[14] D. Gabor, "Microscopy by reconstructed wave fronts: II", *Proceedings of the Physical Society, Section B.,* vol. 64, pp. 449-469, June 1951.

[15] This figure was provided by Dr. Rodney Herring.

[16] H. J. Kreuzer, M. J. Jericho, I. A. Meinertzhagen, and W. B. Xu, "Digital in-line holography with photons and electrons", *Journal Of Physics-Condensed Matter,* vol. 13, p. 10729, Nov 2001.

[17] Dalhousie. "Digital inline holographic (DIH) microscopy", Department of Physics and Atmopsheric Science, updated. http://www.physics.dal.ca/~kreuzer/DIH.html.

[18] E. Hecht, Optics, 4th ed. San Francisco: Addison-Wesley, 2002.

[19] H. J. Kreuzer, K. Nakamura, A. Wierzbicki, H. W. Fink, and H. Schmid, " Theory of the point-source electron microscope", *Ultramicroscopy,* vol. 45, pp. 381-403, Nov 1992.

[20] S. C. Lai, B. King, and M. A. Neifeld, "Wave front reconstruction by means of phase-shifting digital in-line holography", *Optics Communications,* vol. 173, p. 155, Jan 2000.

[21] P. B. Jacquemin, D. Laurin, S. Atalick, R. McLeod, S. Lai, and R. A. Herring, "Non-intrusive, three-dimensional temperature and composition measurements inside fluid cells in microgravity using a confocal holography microscope", *Acta Astronautica,* vol. 60, pp. 723-727, 2007.

[22] J. Colombani and J. Bert, "Holographic interferometry for the study of liquids", *Journal of Molecular Liquids,* vol. In Press, Corrected Proof.

[23] X. D. Xiao and I. K. Puri, "Digital recording and numerical reconstruction of holograms: An optical diagnostic for combustion", *Applied Optics,* vol. 41, p. 3890, Jul 2002.

[24] This figure was provided by Dr. Rodney Herring.

[25] This figure was provided by Robert McLeod.

[26] P. Suetens, Fundamentals of medical imaging: Cambridge University Press, 2002.

[27] C. Huang, G. W. Auner, and H. J. Caulfield, "Direct ultrasonic holography: Feasibility demo", *Acoustics Research Letters Online-Arlo,* vol. 6, pp. 30-34, Jan 2005.

[28] H. Becher and P. N. Burns, Handbook of contrast echocardiography: Left ventricular function and myocardial perfusion. Berlin, 2000.

[29] P. Greguss, "Ultrasonic holograms", *Res. Film,* vol. 5, pp. 330-337, 1965.

[30] B. B. Brenden, "Acoustical-holography", *Journal Of Physics E-Scientific Instruments,* vol. 8, pp. 885-894, 1975.

[31] J. L. Kreuzer, "Ultrasonic holography for nondestructive testing", *Materials Evaluation,* vol. 26, p. 197, 1968.

[32] E. G. Williams, B. H. Houston, and P. C. Herdic, "Fast Fourier transform and singular value decomposition formulations for patch near-field acoustical holography", *Journal Of The Acoustical Society Of America,* vol. 114, pp. 1322-1333, Sep 2003.

[33] W. Bicz, D. Banasiak, P. Bruciak, Z. Gumienny, S. Gumulinski, D. Kosz, A. Krysiak, W. Kuczynski, M. Pluta, and G. Rabiej, "Fingerprint structure imaging based on an ultrasound camera", *Instrumentation Science & Technology,* vol. 27, pp. 295-303, 1999.

[34] E. Twerdowski, M. von Buttlar, N. Razek, R. Wannemacher, A. Schindler, and W. Grill, "Combined surface-focused acoustic microscopy in transmission and scanning ultrasonic holography", *Ultrasonics,* vol. 44, pp. e1301-e1305, 2006.

[35] D. E. Hall, Basic acoustics. New York: Harper & Row, 1987.

[36] G. Martin and E. T. Carroll, "Tables of the speed of sound in water", *The Journal of the Acoustical Society of America,* vol. 31, pp. 75-76, 1959.

[37] M. V. Lobur and Y. P. Kosobutskii, "On the determination of the phase of a plane sound wave transmitted through a layer", *Acoustical Physics,* vol. 50, pp. 612-613, Sep-Oct 2004.

[38] W. S. Burdic, Underwater acoustic system analysis. Englewood Cliffs, NJ: Prentice-Hall, 1984.

[39] X. Lurton, An introduction to underwater acoustics : Principles and applications. London: New York, 2002.

[40] E. G. Williams, Fourier acoustics: Sound radiation and nearfield acoustical holography. San Diego, Calif.: Academic Press, 1999.

[41] O. A. Sapozhnikov, A. E. Ponomarev, and M. A. Smagin, "Transient acoustic holography for reconstructing the particle velocity of the surface of an acoustic transducer", *Acoustical Physics,* vol. 52, p. 324, May-Jun 2006.

[42] K. Fink, "Computer simulation of pressure fields generated by acoustic lens beamformers." Master of Science thesis in *Electrical Engineering*: University of Washington, 1994.

[43] Sound Metrics. "DIDSON - dual frequency identification sonar", Sound Metrics Corp, updated 2007. http://www.soundmetrics.com/PRODUCTS/PR-UNI/productUNI.html.

[44] A. Cittadine, "MEMS reshapes ultrasonic sensing", *Sensors (Peterborough, NH),* vol. 17, p. 17, 2000.

[45] The schematic design for the CAHM was conceived of by Dr. Rodney Herring. This figure was provided by him.

[46] Olympus. "Ultrasonic transducer for nondestructive testing", Panametrics-NDT, updated 2007. http://www.olympusndt.com/en/panametrics-ndt-ultrasonic/.

[47] Onda. "Tables of acoustic properties of materials", Onda Corporation, updated 2006. http://www.ondacorp.com/tecref_acoustictable.html.

[48] Sonora. "FirstCall, the only quantitative transducer tester", Sonora Medical Systems, Inc, updated 2007. http://www.4sonora.com/news/downloads.html.

[49] Y. Abe and A. Iwasaki, "Observation of single and dual vapor bubbles in microgravity", *Denshi Gijutsu Sogo Kenkyusho Iho/Bulletin of the Electrotechnical Laboratory,* vol. 64, p. 67, 2000.

[50] R. E. Davidsen and S. W. Smith, "Two-dimensional arrays for medical ultrasound using multilayer flexible circuit interconnection", *IEEE Transactions on Ultrasonics Ferroelectrics and Frequency Control,* vol. 45, pp. 338-348, Mar 1998.

[51] B. Gonzalez, A. Dominguez, and J. Tojo, "Dynamic viscosities, densities, and speed of sound and derived properties of the binary systems acetic acid with water, methanol, ethanol, ethyl acetate and methyl acetate at t = (293.15, 298.15, and 303.15) K at atmospheric pressure", *Journal of Chemical and Engineering Data,* vol. 49, pp. 1590-1596, Nov-Dec 2004.

[52] This diagram was provided by Dr. Adam Zielinski.

[53] S. Lai, R. A. McLeod, P. Jacquemin, S. Atalick, and R. Herring, "An algorithm for 3-D refractive index measurement in holographic confocal microscopy", *Ultramicroscopy,* vol. 107, pp. 196-201, 2007.

APPENDIX A: ZEMAX MODELS

Zemax prescription for full CAHM design:

units: cm
wavelength: 659.04 µm

Ob	Object Type	Comment	ref ob	Inside	X Pos	Y Pos	Z Pos	X Tilt	T Tilt	Z Tilt	Material	P1	P2	P3	P4	P5	P6	P7	P12	P13	P14	P15
1	Source Ellipse		0	0	0	0	0	0	0	0	-	1000	5E+06	1	0	0	1.9	2	0	0	0	0
2	Detector Rect		0	0	0	0	5	0	0	0		1	1	100	100	1	1	0	-90	90	-90	90
3	Poly Object	130° biprism	2	0	0	0	1.481	0	0	0	MIRROR	1.588	1									
4	Detector Rect		0	0	0	0.95	0.443	0	0	0		0.001	0.001	1	1	1	1	0	-90	90	-90	90
5	Biconic Surface		2	0	0	5.545	-3.41	27	0	0	MIRROR	27.81	32.95	-1	-1	2.5	2.5	0	0	0		
6	Detector Rect		2	0	0	4.51	11.59	0	0	90		1	1	100	100	1	1	0	-90	90	-90	90
7	Biconic Surface		2	0	0	3.307	28.59	175	0	0	MIRROR	8.973	9.327	-1	-1	2.5	2.5	0	0	0		
8	Detector Rect		2	0	0	0	16.48	0	0	90	ABSORB	1.28	1	512	100	1	1	0	-90	90	-90	90
9	Biconic Surface		2	0	0	-5.54	-3.41	-27	0	0	MIRROR	27.81	32.95	-1	-1	2.5	2.5	0	0	0		
10	Biconic Surface		2	0	0	-3.31	28.59	-175	0	0	MIRROR	8.973	9.327	-1	-1	2.5	2.5	0	0	0		
11	Rectangular Volume	SPECIMEN	2	0	0	-4.51	11.09	0	0	0	stefan_n=1	0.5	0.5	1	0.5	0.5	0	0				

Listing of data for catalog: stefan_catalog.agf

Name	N_d	Density	λ_{min}	λ_{max}	Formula	A_0	Comment
STEFAN_VINEGAR		1	1	10000	Schott	1.0399354	n = 1.02, for vinegar
STEFAN_169000	1.69	1	0.31	2.325	Schott	2.8561	n = 1.69000
STEFAN_169025	1.69025	1	0.31	2.325	Schott	2.8569451	n = 1.69025
STEFAN_169050	1.6905	1	0.31	2.325	Schott	2.8577903	n = 1.69050
STEFAN_169075	1.69075	1	0.31	2.325	Schott	2.8586356	n = 1.69075
STEFAN_169100	1.691	1	0.31	2.325	Schott	2.859481	n = 1.69100
STEFAN_169125	1.69125	1	0.31	2.325	Schott	2.8603266	n = 1.69125
STEFAN_169150	1.6915	1	0.31	2.325	Schott	2.8611723	n = 1.69150
STEFAN_N=1329500	1.3295	1	0.31	700	Schott	1.7675703	n = 1.329500
STEFAN_N=1247125	1.247125	1	0.31	700	Schott	1.5553208	n = 1.247125
STEFAN_N=1164750	1.16475	1	0.31	700	Schott	1.3566426	n = 1.164750
STEFAN_N=1082375	1.082375	1	0.31	700	Schott	1.1715356	n = 1.082375
STEFAN_N=1065904	1.065904	1	0.31	700	Schott	1.1361513	n = 1.065904, c = 1391.16 m/s
STEFAN_N=1049428	1.049428	1	0.31	700	Schott	1.1012991	n = 1.049428, c = 1413.00 m/s
STEFAN_N=1032952	1.032952	1	0.31	700	Schott	1.0669898	n = 1.032952, c = 1435.54 m/s
STEFAN_N=1016476	1.016476	1	0.31	700	Schott	1.0332235	n = 1.016476, c = 1458.81 m/s
STEFAN_N=1000000	1	1	0.3	10000	Schott	1	n = 1.000000, c = 1482.84 m/s
STEFAN_N=0983524	0.983524	1	0.31	700	Schott	0.9673195	n = 0.983524, c = 1507.68 m/s
STEFAN_N=0967048	0.967048	1	0.31	700	Schott	0.9351818	n = 0.967048, c = 1533.37 m/s
STEFAN_N=0950572	0.950572	1	0.31	700	Schott	0.9035871	n = 0.950572, c = 1559.95 m/s
STEFAN_N=0934096	0.934096	1	0.31	700	Schott	0.8725353	n = 0.934096, c = 1587.46 m/s
WATER_V=1486		1	1	10000	Schott	4.08E+10	fake index used to produce sound waves at 1485.935m/s
WATER_V=1498		1	1	10000	Schott	4.01E+10	fake index used to produce sound waves at 1498m/s
WATER_V=1540		1	1	10000	Schott	3.79E+10	fake index used to produce sound waves at 1540m/s

Zemax prescription for simplified holography design:

units: mm
wavelength: 1487.76 µm

Ob	Object Type	Comment	ref ob	Inside	X Pos	Y Pos	Z Pos	X Tilt	T Tilt	Z Tilt	Material	P1	P2	P3	P4	P5	P6	P7	P12	P13	P14	P15
1	Source Ellipse		0	0	0	0	13	0	0	0	-	200	2E+06	0.1	0	0	5	5	0	0	0	0
2	Poly Object	130° biprism	0	0	0	0	55	0	0	0	MIRROR	15.88	1									
3	Standard Surface		0	0	0	55	0	95.2	0	0	MIRROR	0	0	25	0							
4	Standard Surface		0	0	0	-55	0	-95.2	0	0	MIRROR	0	0	25	0							
5	Detector Rect		0	0	0	0	-70	0	0	90	ABSORB	7.5	7.5	200	200	1	1	0	-90	90	-90	90
6	Null Object		0	0	0	0	0	0	0	0	-											
7	Rectangular Volume	SPECIMEN	0	0	0	-25	15.7	40	0	0	stefan_n=1	5	5	10	5	5	0	0				

APPENDIX B: FOURIER TRANSFORM ALGORITHM

The following Matlab code was used to measure the phase of the holograms and phase shifts using the Fourier Transform method.

filename: find_shift_ft.m

```
clc; clear;
load holograms; %load measured hologram data

%shift signals down so the average value is zero
signal_1 = water - mean(water);
signal_2 = oil - mean(oil);
signal_3 = vinegar - mean(vinegar);

%normalize the signals so that they are roughly the same amplitude
signal_1 = 100 * signal_1/max(signal_1);
signal_2 = 100 * signal_2/max(signal_2);
signal_3 = 100 * signal_3/max(signal_3);

% interpolate to make more data points in the signal
interp_factor = 5
signal_1 = interp (signal_1,interp_factor);
signal_2 = interp (signal_2,interp_factor);
signal_3 = interp (signal_3,interp_factor);

Ts = positions(2) - positions (1); %sample spacing [mm]
num_samples = length (signal_1) %recalculate # samples, should be 555 now

%Pad the data with zeros to make 1024 samples
% num_zeros = 1024 - old_num_samples; % zero_padding = zeros (1,num_zeros);
% signal_1 = [signal_1, zero_padding]; signal_2 = [signal_2, zero_padding];
% signal_3 = [signal_3, zero_padding];

Ts = Ts/interp_factor;
space_data = [0:Ts:(num_samples-1)*Ts] + positions (1);
Fs = 1/Ts;   %sample frequency [mm^-1]
half_samples = ceil (num_samples/2); %define where half of the data is

total_space_window = space_data(end)-space_data(1); %[mm]
freq_range = (0:num_samples-1)/total_space_window;  %[mm^-1] scale data for frequency
Fw = max (freq_range); %frequency window [mm^-1]
freq_spacing = freq_range (2) - freq_range (1);

figure (1); %plot interpolated hologram data
plot (space_data, signal_1,'b-s','MarkerFaceColor','b','MarkerSize', 3,'LineWidth', 2);
hold on; grid on;
plot (space_data, signal_2,'g-d','MarkerFaceColor','g','MarkerSize', 4.5,'LineWidth', 2);
plot (space_data, signal_3,'r-^','MarkerFaceColor','r','MarkerSize', 4.5,'LineWidth', 2);
hold off; title ('Measured Spatial Holograms','FontSize', 12);
xlabel ('Distance [mm]','FontSize', 12);
ylabel ('Amplitude [V]','FontSize', 12);
Signal_1_text = sprintf ('Water Specimen'); Signal_2_text = sprintf ('Mineral Oil');
Signal_3_text = sprintf ('Vinegar'); legend(Signal_1_text, Signal_2_text, Signal_3_text);
axis ([space_data(1) space_data(num_samples) -Inf Inf]);

%find FT of signals
ft_1 = fft (signal_1); ft_2 = fft (signal_2); ft_3 = fft (signal_3);

%take just the real part
real_ft_1 = real(ft_1); real_ft_2 = real(ft_2); real_ft_3 = real(ft_3);

%take just the imaginary part
imag_ft_1 = imag(ft_1); imag_ft_2 = imag(ft_2); imag_ft_3 = imag(ft_3);

%take the absolute value
abs_ft_1 = abs (ft_1); abs_ft_2 = abs (ft_2); abs_ft_3 = abs (ft_3);

figure(2); %Plot FT  (Absolute Magnitude)
plot (freq_range, abs_ft_1,'b-s','MarkerFaceColor','b','MarkerSize',3,'LineWidth', 2);
hold on; grid on;
plot (freq_range, abs_ft_2,'g-d','MarkerFaceColor','g','MarkerSize',4.5,'LineWidth', 2);
plot (freq_range, abs_ft_3,'r-^','MarkerFaceColor','r','MarkerSize',4.5,'LineWidth', 2);
hold off; title ('Abs Magnitude of FFT','FontSize', 12);
xlabel ('Spatial Frequency [mm^-^1]','FontSize', 12);
ylabel ('Relative Amplitude','FontSize', 12);
legend(Signal_1_text, Signal_2_text, Signal_3_text);

figure(3); subplot(2,1,1); %Plot FT  (Real Part & Imaginary Part)
```

```
plot (freq_range, real_ft_1,'b-s','MarkerFaceColor','b','MarkerSize',3,'LineWidth', 2);
hold on; grid on;
plot (freq_range, real_ft_2,'g-d','MarkerFaceColor','g','MarkerSize',4.5,'LineWidth', 2);
plot (freq_range, real_ft_3,'r-^','MarkerFaceColor','r','MarkerSize',4.5,'LineWidth', 2);
hold off; title ('Real part of FFT');
ylabel ('Relative Amplitude');
legend(Signal_1_text, Signal_2_text, Signal_3_text);
axis ([0 3 -Inf Inf]); set(gca,'xtick',[0:0.25:3],'xminortick','on')
subplot(2,1,2);
plot (freq_range, imag_ft_1,'b-s','MarkerFaceColor','b','MarkerSize', 3,'LineWidth', 2);
hold on; grid on;
plot (freq_range, imag_ft_2,'g-d','MarkerFaceColor','g','MarkerSize',4.5,'LineWidth', 2);
plot (freq_range, imag_ft_3,'r-^','MarkerFaceColor','r','MarkerSize',4.5,'LineWidth', 2);
hold off; title ('Imaginary part of FFT');
xlabel ('Spatial Frequency [mm^-^1]');
ylabel ('Relative Amplitude');
legend(Signal_1_text, Signal_2_text, Signal_3_text);
axis([0 3 min(imag_ft_2(1:half_samples)) Inf]);
set(gca,'xtick',[0:0.25:3],'xminortick','on');

%find the peak frequecies of the 3 FTs
max_value_1 = max (abs_ft_1); peak_positions_1 = find (abs_ft_1 == max_value_1);
peak_pos_1 = peak_positions_1 (1); peak_freq_1 = freq_range (peak_pos_1)

max_value_2 = max (abs_ft_2); peak_positions_2 = find (abs_ft_2 == max_value_2);
peak_pos_2 = peak_positions_2 (1); peak_freq_2 = freq_range (peak_pos_2)

max_value_3 = max (abs_ft_3); peak_positions_3 = find (abs_ft_3 == max_value_3);
peak_pos_3 = peak_positions_3 (1); peak_freq_3 = freq_range (peak_pos_3)

ave_peak_freq = mean ([peak_freq_1 peak_freq_2 peak_freq_3]); %find the ave fringe spacing

%filter the FT, shift peak to zero
filter_ft_1 (1:num_samples) = 0; filter_ft_1 (1) = ft_1 (peak_pos_1);
filter_ft_2 (1:num_samples) = 0; filter_ft_2 (1) = ft_2 (peak_pos_2);
filter_ft_3 (1:num_samples) = 0; filter_ft_3 (1) = ft_3 (peak_pos_3);

abs_filter_ft_1 = abs(filter_ft_1);
abs_filter_ft_2 = abs(filter_ft_2);
abs_filter_ft_3 = abs(filter_ft_3);

real_filter_ft_1 = real(filter_ft_1);
real_filter_ft_2 = real(filter_ft_2);
real_filter_ft_3 = real(filter_ft_3);

imag_filter_ft_1 = imag(filter_ft_1);
imag_filter_ft_2 = imag(filter_ft_2);
imag_filter_ft_3 = imag(filter_ft_3);

%Plot Filtered FT  (Absolute Magnitude)
figure(4); hold on;
plot (freq_range, abs_filter_ft_1,'b*-','linewidth', 2);
plot (freq_range, abs_filter_ft_2,'g*-','linewidth', 2);
plot (freq_range, abs_filter_ft_3,'r*-','linewidth', 2);
hold off;
title ('Abs Magnitude of Filtered FT');
xlabel ('Spatial Frequency [mm^-^1]');
ylabel ('Relative Amplitude');
legend(Signal_1_text, Signal_2_text, Signal_3_text);
axis ([0 freq_range(half_samples) -Inf Inf]);

%Plot Filtered FT  (Real & Imaginary Parts)
figure(5); subplot(2,1,1); hold on; grid on;
plot(freq_range,real_filter_ft_1,'b-s','MarkerFaceColor','b','MarkerSize',3,'LineWidth', 2);
plot(freq_range,real_filter_ft_2,'g-d','MarkerFaceColor','g','MarkerSize',4.5,'LineWidth',
2);
plot(freq_range,real_filter_ft_3,'r-^','MarkerFaceColor','r','MarkerSize',4.5,'LineWidth',
2);
hold off; title ('Real part of Filtered FFT');
ylabel ('Relative Amplitude');
legend(Signal_1_text, Signal_2_text, Signal_3_text);
axis ([0 3 -Inf Inf]); set(gca,'xtick',[0:0.25:3],'xminortick','on')
subplot(2,1,2); hold on; grid on;
plot(freq_range,imag_filter_ft_1,'b-s','MarkerFaceColor','b','MarkerSize',3,'LineWidth', 2);
plot(freq_range,imag_filter_ft_2,'g-d','MarkerFaceColor','g','MarkerSize',4.5,'LineWidth',2);
plot(freq_range,imag_filter_ft_3,'r-^','MarkerFaceColor','r','MarkerSize',4.5,'LineWidth',2);
hold off; title ('Imaginary part of Filtered FFT');
xlabel ('Spatial Frequency [mm^-^1]');
ylabel ('Relative Amplitude');
legend(Signal_1_text, Signal_2_text, Signal_3_text);
axis ([0 3 -Inf Inf]); set(gca,'xtick',[0:0.25:3],'xminortick','on');

% Take Inverse FT
```

```
ift_1 = ifft(filter_ft_1); ift_2 = ifft(filter_ft_2); ift_3 = ifft(filter_ft_3);

% find the angle of the IFT
angle_ift_1 = angle (ift_1); angle_ift_2 = angle (ift_2); angle_ift_3 = angle (ift_3);

% convert to degrees
angle_ift_1_deg = unwrap (angle_ift_1) * 180 / pi;
angle_ift_2_deg = unwrap (angle_ift_2) * 180 / pi;
angle_ift_3_deg = unwrap (angle_ift_3) * 180 / pi;

%Plot IFT Angle
figure(6); subplot(2,1,1); hold on;
plot (space_data,angle_ift_1_deg,'b-s','MarkerFaceColor','b','MarkerSize',3,'LineWidth',1);
plot (space_data,angle_ift_2_deg,'g-d','MarkerFaceColor','g','MarkerSize',4.5,'LineWidth',1);
plot (space_data,angle_ift_3_deg,'r-^','MarkerFaceColor','r','MarkerSize',4.5,'LineWidth',1);
hold off; title ('Phase Angle of Filtered IFT','FontSize', 12);
xlabel ('Horizontal Distance [mm]','FontSize', 12);
ylabel ('Phase Angle [ \circ ]','FontSize', 12);
legend(Signal_1_text, Signal_2_text, Signal_3_text);
axis ([-5 6 -85 35]); set(gca,'ytick',[-80:10:40],'yminortick','on');

angle_1 = mean (angle_ift_1_deg);
angle_2 = mean (angle_ift_2_deg);
angle_3 = mean (angle_ift_3_deg);

delta_angle_12 = angle_1 - angle_2; delta_angle_13 = angle_1 - angle_3;

%Output important values
fprintf ('\n'); fprintf ('%s',num2str(num_samples),' Samples');
fprintf ('\n'); fprintf ('%s','Sample spacing (period) = ', num2str(Ts), ' mm');
fprintf ('\n'); fprintf ('%s','Total spatial window = ',num2str(total_space_window), ' mm');
fprintf ('\n'); fprintf ('%s','Sample Frequency = ', num2str(Fs), ' mm^-1');
fprintf ('\n'); fprintf ('%s','Total Frequency Window = ',num2str(Fw),' mm^-1');
fprintf ('\n'); fprintf ('%s','Frequency Spacing = ', num2str(freq_spacing), ' mm^-1');

fprintf('\n\n');fprintf('%s','Measured Spatial Frequency: ',num2str(ave_peak_freq),' mm^-1');
fprintf ('\n'); fprintf ('%s','Measured Fringe Spacing = ',num2str(1/ave_peak_freq),' mm');

fprintf ('\n\n'); fprintf ('%s','Water Angle = ',num2str(angle_1),' degrees');
fprintf ('\n'); fprintf ('%s','Mineral Oil Angle = ',num2str(angle_2),' degrees');
fprintf ('\n'); fprintf ('%s','Vinegar Angle = ',num2str(angle_3),' degrees');

fprintf ('\n\n');
fprintf ('%s','Angle Shift between Water & Oil = ',num2str(delta_angle_12),' degrees');
fprintf ('\n');
fprintf ('%s','Angle Shift between Water & Vinegar = ',num2str(delta_angle_13),' degrees');
fprintf ('\n');
```

data file: holograms.mat

contains 4 variables:

```
water          <1x111 double>
oil            <1x111 double>
vinegar        <1x111 double>
positions      <1x111 double>
```

APPENDIX C: CURVE FITTING ALGORITHM

The following Matlab code was used to fit the measured holograms to a general sinusoid function, using least- squares fitting.

filename: find_shift_curve_fit.m

```
clear; clc;

load holograms;     % load measured hologram data

lamda = 1.2339;     % [mm]  measured separately using the FT method
amp_factor = 0.65;  % arbirtarily set constant, for amplitude

num_samples = length (water);

Ts = positions(2) - positions (1);    % sample spacing [mm]

est_Ts = Ts /4; %[mm]  increased resolution for plotting of the estimated curve fit
est_positions = positions(1):est_Ts:positions(end); %[mm]

%shift signals vertically so they oscillate above and below zero average
signal_1 = water - mean(water);
signal_2 = oil - mean(oil);
signal_3 = vinegar - mean(vinegar);

%normalize the signals so that they are roughly the same amplitude
signal_1 = 100 * signal_1/max(signal_1);
signal_2 = 100 * signal_2/max(signal_2);
signal_3 = 100 * signal_3/max(signal_3);

figure (1);
plot (positions, water,'b-s','MarkerFaceColor','b','MarkerSize', 3,'LineWidth', 2);
hold on;
plot (positions, oil,'g-d','MarkerFaceColor','g','MarkerSize', 4.5,'LineWidth', 2);
plot (positions, vinegar,'r-^','MarkerFaceColor','r','MarkerSize', 4.5,'LineWidth', 2);
title ('Measured Spatial Holograms for 3 Specimens', 'FontSize', 12);
xlabel ('Horizontal Position [mm]', 'FontSize', 12);
ylabel ('Detected Voltage, V_p_-_p  [mV]',  'FontSize', 12);
Signal_1_text = sprintf ('Water Specimen');
Signal_2_text = sprintf ('Mineral Oil');
Signal_3_text = sprintf ('Vinegar');
legend(Signal_1_text, Signal_2_text, Signal_3_text);
hold off; axis ([-Inf Inf -Inf Inf]); grid on; set(gca,'xminortick','on')

figure (2);
plot (positions, signal_1,'b-s','MarkerFaceColor','b','MarkerSize', 3,'LineWidth', 2);
hold on;
plot (positions, signal_2,'g-d','MarkerFaceColor','g','MarkerSize', 4.5,'LineWidth', 2);
plot (positions, signal_3,'r-^','MarkerFaceColor','r','MarkerSize', 4.5,'LineWidth', 2);
title ('Measured Spatial Holograms (Normalized)', 'FontSize', 12);
xlabel ('Horizontal Position [mm]', 'FontSize', 12);
ylabel ('Normalized Amplitude [%]',  'FontSize', 12);
Signal_1_text = sprintf ('Water Specimen');
Signal_2_text = sprintf ('Mineral Oil');
Signal_3_text = sprintf ('Vinegar');
legend(Signal_1_text, Signal_2_text, Signal_3_text);
hold off; axis ([-Inf Inf -100 100]); grid on; set(gca,'xminortick','on')

% fit the input data to a sine function, find the unknown phase
estimates_1 = fit_sine (positions,signal_1);
est_phi_1 = estimates_1 (1);    %estimated phi from curve fitting
est_amp_1 = amp_factor * max (signal_1);    %amplitude set as a constant
est_sig_1 = est_amp_1 * sin (2*pi/lamda * est_positions + est_phi_1);

estimates_2 = fit_sine (positions,signal_2);
est_phi_2 = estimates_2 (1);
est_amp_2 = amp_factor * max (signal_2);
est_sig_2 = est_amp_2 * sin (2*pi/lamda * est_positions + est_phi_2);

estimates_3 = fit_sine (positions,signal_3);
est_phi_3 = estimates_3 (1);
est_amp_3 = amp_factor * max (signal_3);
est_sig_3 = est_amp_3 * sin (2*pi/lamda * est_positions + est_phi_3);

figure(3);
plot(positions, signal_1, 'b-s','MarkerFaceColor','b','MarkerSize', 3,'LineWidth', 2);
hold on; plot(est_positions, est_sig_1, 'k', 'linewidth', 2);
xlabel ('Position [mm]', 'FontSize', 14);
```

```
ylabel ('Normalized Amplitude [%]',  'FontSize', 12);
title('Water Specimen Hologram fit to Sinusoid function', 'FontSize', 12);
legend('input Water hologram', 'sinusoid fit');
hold off; axis ([-5 6 -100 105]);

figure(4);
plot(positions, signal_2, 'g-d','MarkerFaceColor','g','MarkerSize', 5,'LineWidth', 2);
hold on; plot(est_positions, est_sig_2, 'k', 'linewidth', 2);
xlabel ('Position [mm]', 'FontSize', 12);
ylabel ('Normalized Amplitude [%]',  'FontSize', 12);
title('Mineral Oil Hologram fit to Sinusoid function', 'FontSize', 12);
legend('input Oil hologram', 'sinusoid fit');
hold off; axis ([-5 6 -100 105]);

figure(5);
plot(positions, signal_3, 'r-^','MarkerFaceColor','r','MarkerSize', 5,'LineWidth', 2);
hold on; plot(est_positions, est_sig_3, 'k', 'linewidth', 2);
xlabel ('Position [mm]', 'FontSize', 12);
ylabel ('Normalized Amplitude [%]',  'FontSize', 12);
title('Vinegar Hologram fit to Sinusoid function', 'FontSize', 12);
legend('input Vinegar hologram', 'sinusoid fit');
hold off; axis ([-5 6 -100 105]);

phase_1 = est_phi_1 * 180 / pi;
phase_2 = est_phi_2 * 180 / pi;
phase_3 = est_phi_3 * 180 / pi;

phase_shift_12 = phase_1 - phase_2;
phase_shift_13 = phase_1 - phase_3;

fprintf ('\n');
fprintf ('%s',num2str(num_samples),' Samples');
fprintf ('\n');
fprintf ('%s','Sample spacing = ', num2str(Ts), ' mm');
fprintf ('\n\n');

fprintf ('%s','estimated Phase of Water Signal = ', num2str(phase_1), ' degrees');
fprintf ('\n');
fprintf ('%s','estimated Phase of Oil Signal = ', num2str(phase_2), ' degrees');
fprintf ('\n');
fprintf ('%s','estimated Phase of Vinegar Signal = ', num2str(phase_3), ' degrees');
fprintf ('\n\n');
fprintf ('%s','Phase difference between Water & Oil signals = ', num2str(phase_shift_12), '
degrees');
fprintf ('\n');
fprintf ('%s','Phase difference between Water & Vinegar signals = ', num2str(phase_shift_13),
' degrees');
fprintf ('\n\n');
fprintf    ('%s','Fringe    Shift    between    Water    &    Oil    signals    =    ',
num2str((phase_shift_12)*lamda/360), ' fringes');
fprintf ('\n');
fprintf    ('%s','Fringe    Shift    between    Water    &    Vinegar    signals    =    ',
num2str((phase_shift_13)*lamda/360), ' fringes');
fprintf ('\n');
```

filename: fitsine.m

```
function estimates = fit_sine (time, intensity)
% Call fminsearch with a set starting point
start_phi = 0;
start_point = [start_phi];

options = optimset ('fminsearch');
new_options = optimset (options, 'MaxFunEvals', 50000, 'MaxIter', 50000);

estimates = fminsearch(@sinefun, start_point, new_options);
% sinefun accepts curve parameters as inputs and outputs sse,
% sse is the sum of squares error for FittedCurve - intensity
    function sse = sinefun(params)
        lamda = 1.2339;
        A = 0.65 * max(intensity);
        phi = params (1);

        FittedCurve = (A .* sin(2*pi*time/lamda + phi));
        ErrorVector = FittedCurve - intensity;
        sse = sum(ErrorVector .^ 2);
    end
fprintf ('%s', 'sum of squares error = ', num2str(sum(ErrorVector .^ 2)))
fprintf ('\n');
end
```

APPENDIX D: AUTOCORRELATION ALGORITHM

The following Matlab code was used to measure the phase shifts of the holograms using the autocorrelation algorithm.

filename: find_shift_auto_cor.m

```
clear; clc;
load holograms; %load measured hologram data
lamda = 1.2339; %fringe spacing, measured using the FT method

%shift signals down so the average value is zero
sig_1 = water - mean(water); sig_2 = oil - mean(oil);
sig_3 = vinegar - mean(vinegar);

%normalize the signals so that they are roughly the same amplitude
sig_1 = 100 * sig_1/max(sig_1); sig_2 = 100 * sig_2/max(sig_2);
sig_3 = 100 * sig_3/max(sig_3);

num_samples = length (water)
Ts = positions(2) - positions (1)    %sample spacing [mm]

figure (1); hold on; %plot original hologram data
plot (positions, sig_1,'b-s','MarkerFaceColor','b','MarkerSize', 3,'LineWidth', 2);
plot (positions, sig_2,'g-d','MarkerFaceColor','g','MarkerSize', 4.5,'LineWidth', 2);
plot (positions, sig_3,'r-^','MarkerFaceColor','r','MarkerSize', 4.5,'LineWidth', 2);
title ('Measured Spatial Holograms for 3 Specimens (Normalized)', 'FontSize', 12);
xlabel ('Horizontal Position [mm]', 'FontSize', 12);
ylabel ('Normalized Amplitude',  'FontSize', 12);
sig_1_text = sprintf ('Water Specimen'); sig_2_text = sprintf ('Mineral Oil');
sig_3_text = sprintf ('Vinegar');
legend(sig_1_text, sig_2_text, sig_3_text);
hold off; axis ([-Inf Inf -Inf Inf]); grid on; set(gca,'xminortick','on');

intp_factor = 5   %interpolated to give 5 times the number of points
intp_sig_1 = interp (sig_1,intp_factor);
intp_sig_2 = interp (sig_2,intp_factor);
intp_sig_3 = interp (sig_3,intp_factor);

new_num_samples = num_samples * intp_factor
new_Ts = Ts/intp_factor     %the new sample spacing (smaller)
intp_positions = [0:new_Ts:(new_num_samples-1)*new_Ts] + positions (1); %new pos values

figure (2); hold on; %plot interpolated hologram data
plot(intp_positions,intp_sig_1,'b-s','MarkerFaceColor','b','MarkerSize',3,'LineWidth', 2);
plot(intp_positions,intp_sig_2,'g-d','MarkerFaceColor','g','MarkerSize',4.5,'LineWidth', 2);
plot(intp_positions,intp_sig_3,'r-^','MarkerFaceColor','r','MarkerSize',4.5,'LineWidth', 2);
title ('Holograms with interpolated points', 'FontSize', 12);
xlabel ('Horizontal Position [mm]', 'FontSize', 12);
ylabel ('Normalized Amplitude',  'FontSize', 12);
legend(sig_1_text, sig_2_text, sig_3_text);
hold off; axis ([-Inf Inf -Inf Inf]); grid on; set(gca,'xminortick','on');

% find the autocorellation sequence and the pixel (position) shift between the input signals
[r_index, r_total_1, pos_shift_12] = auto_cor (sig_1,sig_2);
[r_index, r_total_2, pos_shift_13] = auto_cor (sig_1,sig_3);
[r_index, r_total_3, pos_shift_23] = auto_cor (sig_2,sig_3);

figure (3); hold on; %plot the autocorrelation sequence
plot (r_index, r_total_1,'g-d','MarkerFaceColor','g','MarkerSize', 4.5,'LineWidth', 2');
plot (r_index, r_total_2,'r-^','MarkerFaceColor','r','MarkerSize', 4.5,'LineWidth', 2);
%plot (r_index, r_total_3,'b-s','MarkerFaceColor','b','MarkerSize', 3,'LineWidth', 2);
hold off; title ('Autocorrelation Sequence vs Shift Value',  'FontSize', 12);
xlabel ('n', 'FontSize', 12); ylabel ('r_n', 'FontSize', 12);
legend ('Mineral Oil vs Water', 'Vinegar vs Water')%, 'Mineral Oil vs Vinegar');
hold off; axis ([-100 100 -Inf Inf]); grid on; set(gca,'xminortick','on','yminortick','on');

% find autocorellation sequence and the pixel (position) shift between interpolated signals
[intp_r_index,intp_r_total_1,intp_pos_shift_12]=auto_cor(intp_sig_2,intp_sig_1);
[intp_r_index, intp_r_total_2,intp_pos_shift_13]=auto_cor(intp_sig_3,intp_sig_1);
[intp_r_index, intp_r_total_3,intp_pos_shift_23]=auto_cor(intp_sig_2,intp_sig_3);

pos_shift_12, pos_shift_13,intp_pos_shift_12, intp_pos_shift_13,
fprintf ('\n');

figure (4); hold on; %plot the interpolated autocorellation sequence (Zoomed in)
plot(intp_r_index,intp_r_total_1,'g-d','MarkerFaceColor','g','MarkerSize',4.5,'LineWidth',2);
plot(intp_r_index,intp_r_total_2,'r-^','MarkerFaceColor','r','MarkerSize',4.5,'LineWidth',2);
```

```
hold off; title ('Interpolated Autocorrelation Sequence vs Shift Value',  'FontSize', 12);
xlabel ('n', 'FontSize', 12); ylabel ('r_n', 'FontSize', 12);
legend ('Mineral Oil vs Water', 'Vinegar vs Water')%, 'Mineral Oil vs Vinegar');
hold off; axis ([-50 50 -1.5e6 2e6]); grid on; set(gca,'xminortick','on', 'yminortick', 'on',
'xtick',[-50:5:50]);

%Output important values
fprintf ('%s','Mineral Oil vs Water Position Shift = ',num2str(pos_shift_12*Ts),' mm', '    =
',num2str(pos_shift_12*Ts*360/lamda),' degrees');
fprintf ('\n');
fprintf ('%s','Vinegar vs Water Position Shift = ',num2str(pos_shift_13*Ts),' mm', '     =
',num2str(pos_shift_13*Ts*360/lamda),' degrees');
fprintf ('\n');
fprintf   ('%s','Mineral   Oil   vs   Vinegar   =   ',num2str(pos_shift_23*Ts),'   mm','   =
',num2str(pos_shift_23*Ts*360/lamda),' degrees');
fprintf ('\n\n');

fprintf ('Interpolated Results'); fprintf ('\n');
fprintf ('%s','Mineral Oil vs Water Position Shift = ',num2str(intp_pos_shift_12*new_Ts),'
mm', '    = ',num2str(intp_pos_shift_12*new_Ts*360/lamda),' degrees');
fprintf ('\n');
fprintf ('%s','Vinegar vs Water Position Shift = ',num2str(intp_pos_shift_13*new_Ts),' mm', '
= ',num2str(intp_pos_shift_13*new_Ts*360/lamda),' degrees');
fprintf ('\n');
fprintf ('%s','Mineral Oil vs Vinegar = ',num2str(intp_pos_shift_23*new_Ts),' mm', '     =
',num2str(intp_pos_shift_23*new_Ts*360/lamda),' degrees');
fprintf ('\n');
```

filename: auto_cor.m

```
%auto/cross correlation function for two signals to determine the phase shift
function  [r_indices,  r_total,  measured_position_shift]  =  find_phase_shift  (signal_1,
signal_2)

N = length(signal_1); %number of data points in whole signal

start_pos = 2*N + 1;   %start signal 1 at this index # plus one
end_pos = start_pos + N-1;

% make a signal with 2N zeros at the front, then N elements, then 2N more zeros
s1 (1 : end_pos+2*N) = 0;       %set all intially to zero
s1 (start_pos : end_pos) = signal_1;

%Signal 2 is shifted wrt Signal 1
s2 (1 : start_pos+2*N) = 0;       %set all intially to zero
s2 (start_pos : end_pos) = signal_2;

%auto correlation fxn
for k = 1:N
    r_sum = 0;
    r_negative_sum = 0;
    for x = 1:N
        r_sum = r_sum + s1(start_pos+x)* s2(start_pos+x-k);
        r_negative_sum = r_negative_sum + s1(start_pos+x)* s2(start_pos+x+k);
    end
    r(k) = r_sum;
    r_negative (N-k+1) = r_negative_sum;
end

r_zero = 0;

for x = 1:N
    r_zero = r_zero + s1(start_pos+x)* s2(start_pos+x);
end

% final autocorrelation function with all values filled
r_total (1:N) = r_negative; r_total (N+1) = r_zero; r_total (N+2:N+N+1) = r;

% indices of autocorellation function
r_indices = -N:N; [max_value, index_value] = max (r_total);

measured_position_shift = r_indices (index_value); %measured position shift in pixels
```